VOL. XX

REVIEW OF THE AIR FORCE ACADEMY

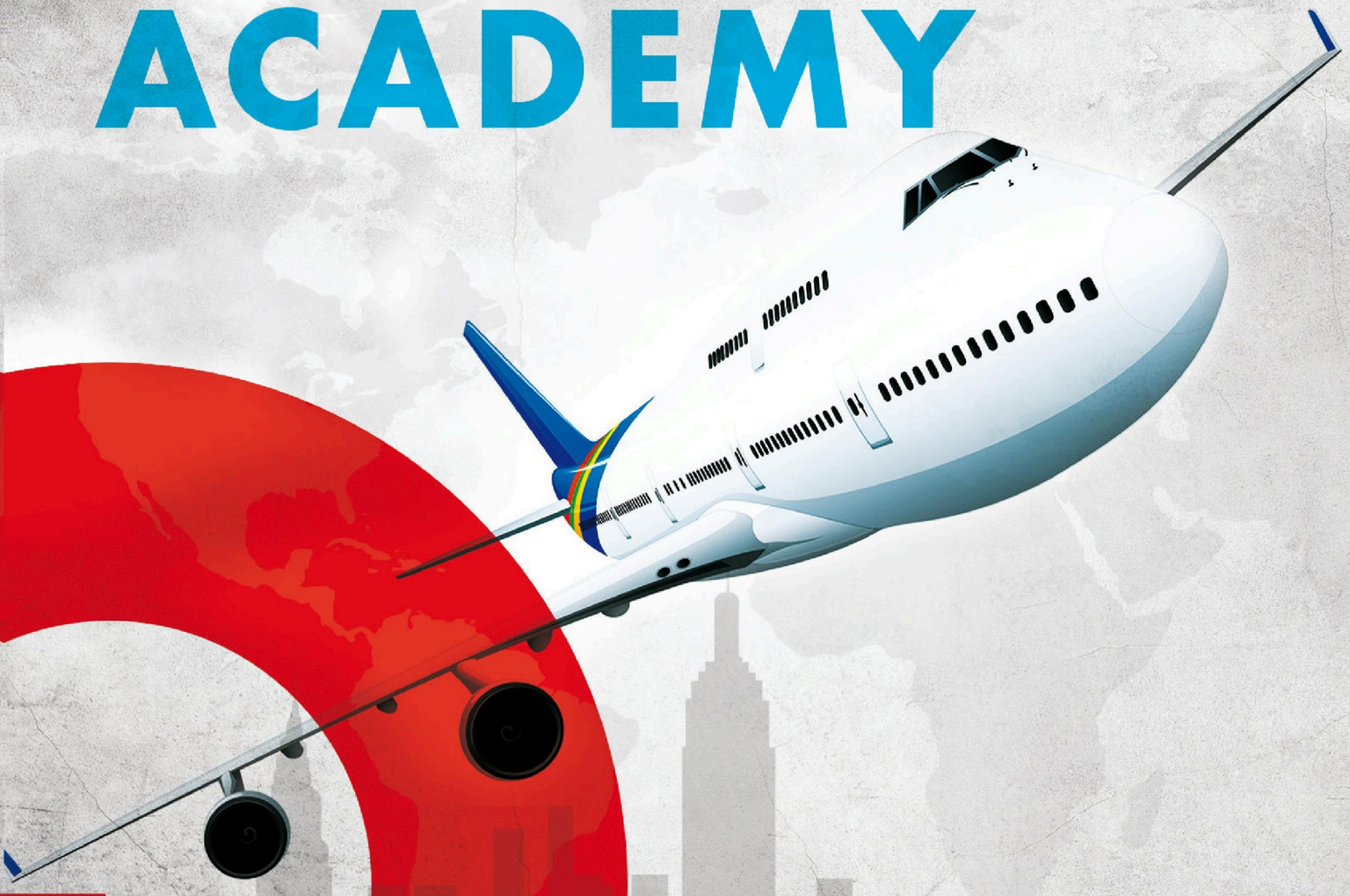

No. 2 (46)/2022

Review
of the Air Force Academy

The Scientific Informative Review, Vol. XX, No.2 (46)/2022
DOI: 10.19062/1842-9238.2022.20.2

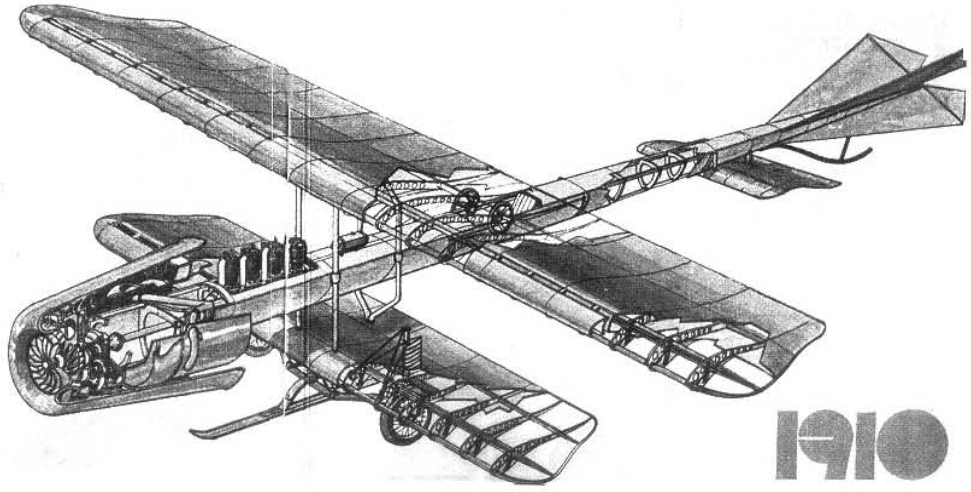

BRAŞOV - ROMANIA

© February, 2023
Visa 0574-12/2022
I.S.S.N. 1842-9238

"Henri Coandă" Air Force Academy Publishing House, 160, Mihai Viteazul St., Braşov, ROMÂNIA
Phone: +40 268 423421, e-mail: editura@afahc.ro

C O N T E N T S

REMOTE SENSING IN BIOMETEOROLOGY

Alexandru TUDOR

"Henri Coandă" Air Force Academy, Braşov, Romania (alexandru.tudor@afahc.ro@afahc.ro)
ORCID: 0009-0001-1471-2549

DOI: 10.19062/1842-9238.2022.20.2.1

Abstract: *Remote sensing is a powerful tool used in biometeorology to study the interactions between the atmosphere and living organisms, particularly plants. Through satellite-based sensors, researchers can observe and analyze a range of biophysical parameters related to vegetation, such as leaf area index, biomass, vegetation cover, and land surface temperature. This data can be used to estimate plant growth, productivity, and water use efficiency, as well as monitor environmental conditions, such as drought, heat stress, and air pollution. Remote sensing is used in the development of crop models for agricultural management and to study the impact of climate change on plant communities and ecosystems. By tracking changes in vegetation cover and productivity, as well as changes in phenology, remote sensing helps researchers identify optimal planting times, irrigation schedules, and predict crop yields.*

Keywords: *remote sensing, biometeorology, atmosphere, satellite-based sensor, climate change, seasonal biology, land surface temperature (LST), climate change.*

1. INTRODUCTION

Remote sensing is a powerful tool in biometeorology that allows researchers to observe and analyze vegetation and other environmental variables at large spatial and temporal scales. Biometeorology is the study of the interactions between the atmosphere and living organisms, particularly plants, and how these interactions affect the climate and weather. [1].

Remote sensing technologies, such as satellite-based sensors, can provide data on a range of biophysical parameters related to vegetation, including leaf area index (LAI), biomass, vegetation cover, and land surface temperature (LST). These data can be used to estimate plant growth, productivity, and water use efficiency, as well as to monitor environmental conditions, such as drought, heat stress, and air pollution.[1][2]

Remote sensing is used in biometeorology in the development of crop models for agricultural management. These models use remote sensing data, along with weather and soil information, to predict crop yields and identify optimal planting times and irrigation schedules.Another example is the use of remote sensing to study the impact of climate change on plant communities and ecosystems. Remote sensing data can help researchers track changes in vegetation cover and productivity, as well as changes in phenology (the timing of seasonal events, such as leaf emergence and flowering). [3][4] [5].

2. REMOTE SENSING

Remote sensing has become an important tool in biometeorology for studying the complex interactions between the atmosphere and living organisms, and for monitoring

and predicting changes in the environment over time. Remote sensing is the process of collecting data about the environment without physically being present. In biometeorology, remote sensing is used to collect data on the Earth's surface and atmosphere to study the impacts of weather and climate on living organisms. [4] [5]

Different remote sensing techniques can be used to monitor changes in vegetation, land use, and weather patterns over time, providing valuable information for biometeorologists. For example, satellite imagery can be used to track changes in vegetation cover and identify areas affected by drought or other weather-related stressors. In addition, it can be used to measure various atmospheric parameters, such as temperature, humidity, and air pressure, which can help researchers to better understand the impacts of weather and climate on living organisms. For example, remote sensing data can be used to track the movement of air masses, which can impact the distribution and migration patterns of birds and other animals. [6]

The use of remote sensing in biometeorology has led to a better understanding of the complex relationship between the natural environment and living organisms, and has enabled researchers to develop more accurate models and predictions of how weather and climate impact the health, behavior, and well-being of different species. [3][4]

3. FURTHER USE OF REMOTE SENSING APPLIED TO BIOMETEOROLOGY FILEDS

Remote sensing provides a way to measure and monitor a variety of environmental variables over large spatial and temporal scales. Some of the key ways in which remote sensing can be applied in biometeorology include:

Vegetation monitoring: The use of remote sensing can enable the measurement of vegetation indices, including but not limited to the normalized difference vegetation index (NDVI) and leaf area index (LAI), which offer valuable insight into the extent and condition of vegetation coverage. These indices can be used to monitor changes in vegetation productivity, health, and distribution, and to identify areas of drought stress or other environmental stressors. [7][8]

Land surface temperature (LST) mapping: Remote sensing can be used to measure LST, which is an important parameter for understanding biophysical processes such as evapotranspiration and energy balance. LST mapping can be used to identify areas of urban heat island effect or to monitor changes in temperature associated with land cover changes or climate change.

Crop monitoring: Remote sensing can be used to monitor crop health and productivity, by measuring parameters such as leaf chlorophyll content and canopy temperature. These measurements can be used to optimize irrigation and fertilizer use, and to predict crop yields.

Phenological monitoring: Remote sensing can be used to track the timing of seasonal events, such as leaf emergence and flowering, which can provide important information on changes in plant growth and climate patterns.

Air quality monitoring: Remote sensing can be used to monitor air quality, by measuring parameters such as atmospheric particulate matter and ozone concentration. These measurements can be used to identify areas of high pollution and to assess the impact of pollution on vegetation and human health.

Remote sensing provides a powerful tool for monitoring and analyzing environmental variables related to biometeorology, and can help researchers better understand the complex interactions between living organisms and the atmosphere. [9][10] [11]

4. USING LST MAPPING IN BIOMETEOROLOGY

Land surface temperature (LST) mapping is an important tool in biometeorology, as it provides information on the temperature of the Earth's surface, which can impact the energy balance between the surface and the atmosphere. Some of the key ways in which LST mapping is used in biometeorology include:

Urban heat island effect: LST mapping can be used to identify areas of urban heat island effect, where cities and other developed areas are significantly warmer than surrounding rural areas due to factors such as increased energy use, reduced vegetation cover, and increased impervious surfaces.

Drought monitoring: LST mapping can be used to monitor drought conditions, as areas experiencing drought tend to have higher LST values due to reduced vegetation cover and soil moisture. [12][13]

Evapotranspiration: LST mapping can be used to estimate evapotranspiration rates, which is the combined loss of water from the Earth's surface through evaporation and plant transpiration. LST mapping can be used to estimate the amount of energy used for these processes, which is an important parameter for understanding the water balance in ecosystems.

Climate change impacts: LST mapping can be used to monitor changes in temperature associated with climate change, such as changes in the timing and duration of the growing season, or changes in the distribution of vegetation types.

Vegetation health: LST mapping can be used to monitor vegetation health, as changes in LST can indicate changes in plant water stress, disease, or other factors affecting vegetation health.

LST mapping is a valuable tool in biometeorology for monitoring and analyzing the impacts of environmental factors on the Earth's surface temperature and the associated biophysical processes. [13][14]

5. HEAT STRESS AND URBAN HEAT. THERMAL PERCEPTION STUDY OF URBAN AREAS

Thermal perception in urban areas is an important area of study in biometeorology, as it relates to the way that people experience and respond to temperature in urban environments. Some of the key ways in which biometeorology researchers study thermal perception in urban areas include:

Heat stress assessments: Biometeorologists use thermal perception data to assess the potential for heat stress in urban areas, which can help city planners and public health officials to develop strategies for mitigating the negative impacts of heat on human health. [30]

Thermal comfort mapping: Biometeorologists use data on thermal perception to create maps of thermal comfort in urban areas, which can help city planners and architects to design buildings and public spaces that are more comfortable for people to use in different weather conditions. [30][31]

Urban heat island effect: Biometeorologists study the effect on urban heat island, which is the phenomenon of warmer areas in urban environment than surrounding rural areas due to factors such as increased energy use and reduced vegetation cover. This can lead to increased thermal discomfort for urban residents, and biometeorologists study ways to mitigate this effect through urban greening and other strategies. [32][33]

Microclimate monitoring: Biometeorologists use sensors and other technology to monitor microclimates in urban areas, which can help to identify areas of high thermal discomfort and inform strategies for reducing heat stress.

Human behavior and adaptation: Biometeorologists study the way that people adapt to and respond to different thermal conditions in urban environments, such as the use of air conditioning or changes in outdoor activities.

The examination of how humans perceive temperature in urban settings is a significant subject in biometeorology investigation. Its significance lies in the impact it has on the health and welfare of people living in urban areas, and on the planning and administration of cities in the context of a changing climate. [33][34][35]

6. SATELLITE IMAGERY

Satellite imagery is a valuable tool in biometeorology as it allows researchers to monitor large-scale weather patterns and changes in vegetation and land use over time. This data can then be used to study the impacts of weather and climate on living organisms, including humans, animals, and plants. For example, satellite imagery can be used to track the distribution and movement of weather systems, such as hurricanes and typhoons, which can have a significant impact on human populations and ecosystems. Satellite data can also be used to monitor changes in vegetation cover and land use, which can provide insights into the impacts of climate change and human activities on ecosystems and wildlife. [27]

It can be used to monitor environmental conditions in real-time, providing early warning systems for natural disasters, such as droughts, floods, and wildfires. This data can help inform decision-making processes and enable communities to prepare and respond to potential threats.

Biometeorology relies heavily on satellite imagery as a critical resource to better understand the intricate interactions between the environment and organisms, aiding in the creation of precise models and forecasts of the effects of weather and climate on various species' health, behavior, and overall welfare. [28][29]

7. URBAN MAPING

Urban mapping is the process of creating detailed maps of urban areas, including buildings, streets, and infrastructure. In biometeorology, urban mapping is used to study how the built environment affects local weather and climate, as well as the health and well-being of urban populations. [24][25]

Urban mapping is used to identify areas of the city that are more susceptible to heat island effects, where temperatures are significantly higher than surrounding areas due to the presence of buildings and other infrastructure. This information can then be used to develop strategies to mitigate the impacts of heat on urban populations, such as the installation of green roofs and other urban green spaces.Urban mapping can also be used to study how air pollution levels vary across different neighborhoods and urban areas, providing insights into how these factors impact the health and well-being of residents. This information can be used to inform policies and interventions to reduce air pollution and improve public health.

By using this tool in biometeorology, it’s providing valuable insights into the complex relationship between the built environment, weather and climate, and the health and well-being of urban populations. By understanding these relationships, researchers and

policymakers can develop strategies to improve the resilience and sustainability of urban areas, while also promoting the health and well-being of urban residents. [24][26]

8. URBAN FOOTPRINT MAPPING

Urban footprint mapping is a process of mapping the extent and characteristics of urban land use, often using remote sensing and geographic information systems (GIS) technologies. In biometeorology, urban footprint mapping is used to understand the impacts of urbanization on the environment and human health.

Urbanization can lead to significant changes in the local climate, including increased temperatures, altered wind patterns, and changes in precipitation. Urban footprint mapping can help identify areas that are particularly vulnerable to these impacts, such as neighborhoods with low levels of green space or areas with a high concentration of impervious surfaces like roads and buildings. By analyzing the extent and characteristics of urban land use, researchers can also identify areas where urban development may be encroaching on sensitive ecosystems or agricultural land, and develop strategies to promote more sustainable land use patterns.

It can also be used to study the distribution of environmental health hazards in urban areas, such as air pollution and heat stress, and to develop targeted interventions to address these hazards and promote public health.

This tool allows for a comprehensive understanding of the effects of urbanization on both the environment and human health. This knowledge can be used by researchers and policymakers to devise effective strategies aimed at promoting sustainable and healthy urban development. [26]

9. LANDSAT SATELLITES

Landsat is a series of Earth observation satellites operated by the United States Geological Survey (USGS). The Landsat program provides a continuous stream of moderate-resolution imagery of the Earth's land surfaces, helping scientists, resource managers, and policymakers make informed decisions about natural resources and the environment. The satellites are in a polar orbit, circling the Earth from north to south and taking images of the same areas at regular intervals. The latest Landsat satellite, Landsat 9, was launched on September 27, 2021, and it is now in operational mode.

The Landsat program has several operational components that work together to provide continuous and reliable satellite imagery. These include:

Satellite Operations Control Center (SOCC): This facility is responsible for controlling the Landsat satellites, monitoring their health, and ensuring they are functioning correctly. SOCC is located at the Goddard Space Flight Center in Maryland, USA.

Ground Data System (GDS): The GDS receives the data transmitted by the Landsat satellites and processes it into usable imagery products. The GDS is responsible for archiving Landsat data, generating products, and distributing data to users.

Landsat Science Team: The Landsat Science Team is a group of scientists who advise the USGS on scientific and technical issues related to Landsat data. The team helps ensure that Landsat data is of the highest quality and meets the needs of the scientific community.

Landsat Ground Stations: There are several Landsat ground stations located around the world that receive data from the Landsat satellites. These ground stations are responsible for receiving, processing, and distributing Landsat data to users.

Landsat operations involve the coordination of these different components to ensure that the satellites are functioning correctly, the data is being received and processed efficiently, and the resulting imagery is of the highest quality. [23][22]

10. LANDSAT ROMANIA

Landsat data has been used extensively in Romania for a variety of applications, including land cover and land use mapping, agriculture, forestry, geology, and hydrology. One example of Landsat's use in Romania is in monitoring land cover change. Landsat data has been used to study changes in land use and land cover in the country, such as the expansion of urban areas, deforestation, and changes in agricultural practices.

This data has also been used to study the effects of climate change on vegetation dynamics and agricultural productivity. Researchers have usedLandsat data to study the response of vegetation to changes in temperature and precipitation patterns, and how these changes may affect crop yields and agricultural productivity. In addition, acquired data has been used to study water resources in Romania, including surface water and groundwater. Researchers have used Landsat data to map and monitor changes in the country's river systems, as well as to study the impacts of climate change and land use on water resources.

Past couple of years this data has played an important role in understanding and managing natural resources in Romania, and has and will be used by local authorities and researchers, to make informed decisions about land use, water management, and environmental protection. [20][21]

11. LANDSAT 8 AN 9 OVER ROMANIA

In the past few decades, Romania's countryside has undergone significant changes in response to evolving land management policies and alterations in the natural environment. Consequently, numerous farms now exhibit a fascinating range of shapes and sizes, particularly when observed from an aerial perspective.

FIG.1 Acquired April 8, 2020[36]

These images of the Oltenia province in southwest Romania were captured by the Operational Land Imager (OLI) on Landsat 8 on April 8, 2020. The false-color representation of the images using bands 6-5-2 enhances the differentiation of various land covers across the province's mountains, foothills, and plains.

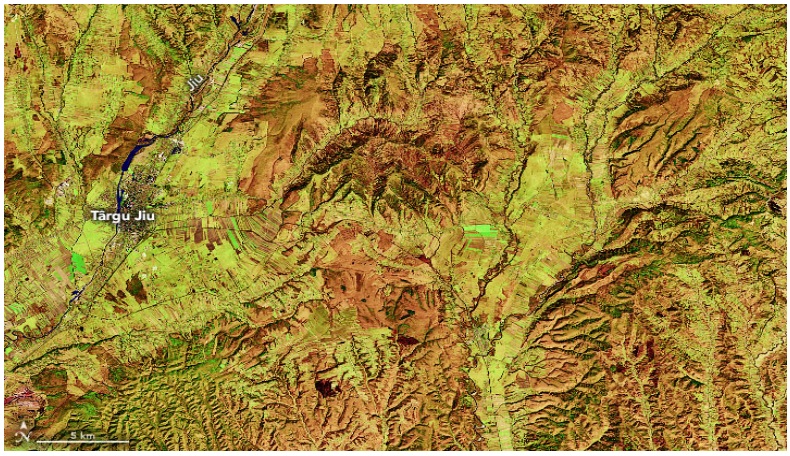

FIG.2 Acquired April 8, 2020 [36]

The top image provides a comprehensive view of the Oltenia province, encompassing the Olt River to the east, the Danube River to the south, and the South Carpathian Mountains to the north. The higher elevations of the Carpathian range, which surpass 2500 meters (8200 feet), are covered in snow and ice, depicted in light blue. The forested regions of the Carpathians, characterized by a mix of coniferous and deciduous trees, appear as a blend of dark green and orange colors.

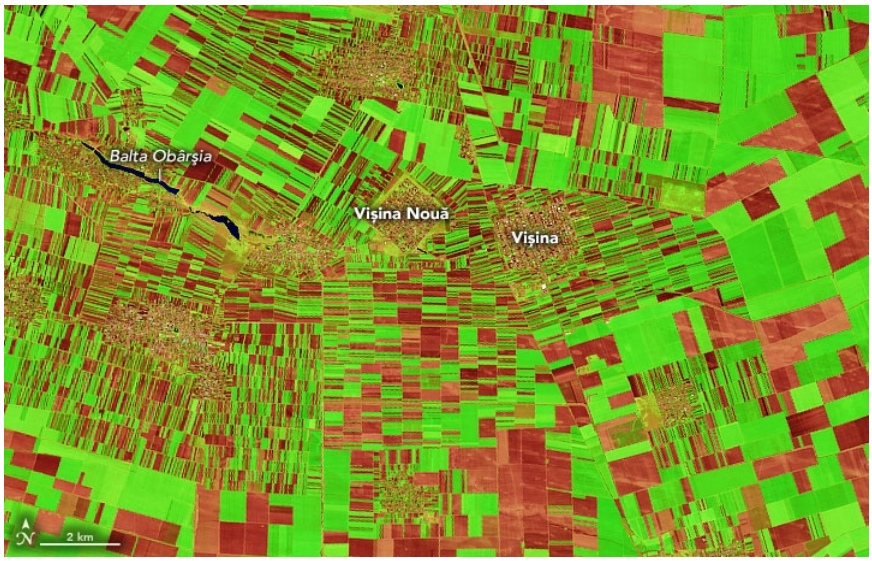

FIG.3 Acquired April 9, 2020 [36]

The lower elevations, ranging between 300 to 800 meters, exhibit forested areas (mostly orange) primarily consisting of oak and beech trees, spreading across the foothills. The valleys within the foothills display a vibrant green color, indicating thriving crops. The flat terrain adjacent to the river channels offers suitable land for farming amidst the otherwise mountainous terrain. [17][18][19]

12. LANDSAT AS A REMOTE SENSING TOOL

Landsat is a remote sensing program that uses satellites to capture images of the Earth's land surfaces. The Landsat satellites have a number of instruments on board, including the Operational Land Imager (OLI) and the Thermal Infrared Sensor (TIRS), which capture images in visible, near-infrared, short-wave infrared, and thermal infrared wavelengths. These images are used to study the Earth's land surfaces and the changes that occur over time.The imagery can be used to detect changes in land use, such as deforestation, urbanization, and agricultural expansion. It can also be used to monitor natural disasters, such as wildfires, floods, and landslides.

To analyze Landsat remote sensing data, a number of image processing techniques are used, such as image enhancement, image classification, and change detection. These techniques allow researchers to extract information from the images, such as the location and extent of different land cover types, and changes in land cover over time. The program provides a valuable resource for monitoring and understanding the Earth's land surfaces, and the remote sensing data it provides is widely used by researchers, policymakers, and natural resource managers around the world.

Limits and drawbacks: It is important to note that image sensing is just one tool in a larger toolbox of biometeorological methods. While image sensing can provide valuable data on vegetation cover, land use, and other biophysical features, it has limitations that must be addressed in order to make accurate and useful predictions and assessments.

One key limitation is the weather dependency of image sensing. Cloudy or rainy weather can reduce image quality or prevent image capture altogether, making it difficult to gather comprehensive data on a particular area. This limitation can be mitigated by using multiple sensors or integrating other data sources such as weather data, to ensure that missing image data is accounted for. Another limitation is the limited spatial coverage of image sensing. This limitation can be addressed by using satellite-based sensors or unmanned aerial vehicles (UAVs) to obtain data from larger or remote areas. However, these technologies can be expensive and require specialized expertise and equipment.

Temporal resolution is also a limitation of image sensing, as images are typically captured at discrete intervals, which may not capture the rapid changes in weather patterns or biophysical features that occur over short periods of time. To address this limitation, more frequent image capture can be used, or data from other sources, such as remote sensing or weather stations, can be used to supplement image data.

The high costs associated with image sensing can also be a barrier to its use in biometeorology, particularly in developing countries or regions with limited resources. To address this, alternative data sources and methods may need to be used, such as participatory methods or community-based monitoring, which can be more cost-effective and provide valuable data on local conditions.

Finally, the limited spectral resolution of image sensing can also be a limitation, particularly when attempting to differentiate between different biophysical features or patterns. This limitation can be addressed by using sensors with higher spectral resolution, or by combining image data with other types of data, such as meteorological or ground-based data, to provide a more comprehensive understanding of environmental conditions.

As a conclusion, while image sensing is a valuable tool in biometeorology, its limitations must be carefully considered when planning and implementing biometeorological studies. Alternative data sources and methods may need to be used to

supplement image sensing data in order to obtain a comprehensive understanding of the impact of weather and climate patterns on living organisms and the environment. [15][16]

REFERENCES

[1] P. S. Thenkabail, (2019). *Remote Sensing in Agriculture: An Introduction*. Taylor & Francis;
[2] J. L. Hatfield & J. H. Prueger, (2015). *Handbook of agricultural meteorology.* Routledge;
[3] S. J. Goetz, A. G. Bunn, G. J. Fiske & R. A. Houghton (2005) *Satellite-observed photosynthetic trends across boreal North America associated with climate and fire distur*, of the American Meteorological Society, 78(4), 621-636;
[4] B. D. Wardlow, S. L. Egbert, J. H. Kastens & G. M. Henebry (2007). *Comparison of the growing season dynamics of NDVI and EVI for a Canadian prairie crop. Remote Sensing of Environment*, 107(2), 204-215;
[5] A. D. Richardson, J. P. Jenkins, B. H. Braswell, D. Y. Hollinger & S. V. Ollinger (2007). *Near-surface remote sensing of spatial and temporal variation in canopy phenology*, Ecological Applications, 17(6), 1919-1934;
[6] X. Xiong, J. Butler, Comprehensive Remote Sensing Volume 1, 2018, Pages 1-6, *Comprehensive Remote Sensing*;
[7] T. M. Lillesand, R. W. Kiefer & J. W. Chipman, (2015), *Remote sensing and image interpretation*, John Wiley & Sons;
[8] D. Bălteanu et al. (2013), *Land Use and Crop Dynamics Related to Climate Change Signals During the Post-Communist period in the South Oltenia, Romania*, Proceedings of the Romanian Academy, 15 (3), 265–278;
[9] D. Dogaru, et al. (2019), *Drivers and Dynamics of Agricultural Land Fragmentation in the Western Part of the Romanian Plain*, Romanian Journal of Geography, 63 (2), 145–165;
[10] JPL Photojournal (2020, February 3) PIA23677: Gorj Province, Romania. Accessed April 29, 2020;
[11] S. Qiu, J. Liu, Y. Liu & Y. Zhang, (2019), *Application of remote sensing technology in land surface temperature research: Progress and prospect. Remote Sensing*, 11(8), 944;
[12] Y. Peng, L. Zhang & Z. Gao, (2021), *Advances in the application of remote sensing technology in biometeorology*, International Journal of Biometeorology, 65(6), 901-914;
[13] P. S. Thenkabail, (2016), *Land surface temperature (LST) estimation from Landsat 8 satellite: Example from the irrigated and rainfed cropping systems in the Arizona Sonoran Desert, USA. In Remote sensing of land use and land cover: Principles and applications* (pp. 75-99). CRC Press;
[14] M. K. Ridd, (1995), *Exploring a V-I-S (vegetation-impervious surface-soil) model for urban ecosystem analysis through remote sensing: comparative anatomy for cities*, International Journal of Remote Sensing, 16(12), 2165-2185;
[15] T. Kuemmerle et al. (2009), *Land use change in Southern Romania after the collapse of socialism*, Regional Environmental Change, 9 (1);
[16] NASA Earth Observatory images by Joshua Stevens, using Landsat data from the U.S. Geological Survey. Story by Kathryn Hansen with image interpretation by Dan Bălteanu/Romanian Academy;
[17] M.V. Birsan, A. Dumitrescu, (2014), *Romanian daily gridded climatic dataset* (1961-2013), National Meteorological Administration, Bucharest, Romania. https://doi.pangaea.de/10.1594/ PANGAEA.833627*;*
[18] E. Mateescu, M. Smarandache, N. Jeler, V. Apostol, (2013), *Drought conditions and management strategies in Romania*. In D. Tsegai &Ardakanian (Eds.), Capacity Development to Support National Drought Management Policies for Eastern European Countries (pp.56-61);
[19] M. Radoane & R. Popescu, (2018), *Assessment of vegetation response to climate change using Landsat data in Romania*, Environmental Monitoring and Assessment, 190(2), 74;
[20] L. C. Dincă & R. S. Savastru, (2020), *The use of Landsat data in monitoring land use/land cover changes in Romania*, In Advances in Environmental Research (Vol. 75, pp. 73-87). Elsevier;
[21] F. M. Chmielewski & T. Rötzer (2001), *Response of tree phenology to climate change across Europe. Agricultural and Forest Meteorology*, 108(2), 101-112;
[22] R. Geiger, R. H. Aron & P. Todhunter, (2003), *The climate near the ground. Rowman& Littlefield*;
[23] S. K. Dash, S. R. Goward, R. O. Dubayah, and A. R. Michaelis, *Advances in Remote Sensing Applications in Biogeography and Biometeorology*, Geogr. Compass, vol. 3, no. 6, pp. 2209–2238, Nov. 2009;
[24] A. C. Comrie and J. W. Thornes, *Biometeorology for urban planning and building design*, in Applied Climatology: Principles and Practice, Routledge, 2007, pp. 305–335;

[25] J. Kleerekoper, E. Van Esch, and P. Salcedo, *How to make a city climate-proof, addressing the urban heat island effect*, Resour. Conserv. Recycl., vol. 64, pp. 30–38, Feb. 2012;
[26] El Kenawy, A. M., & Ouarda, T. B. M. J. (2014), *Remote sensing applications in meteorology and climatology. Remote Sensing*, 6(5), 4177-4180. doi: 10.3390/rs6054177;
[27] G. Jia , X. Liu, X. Li, & D. Zhuang, (2020), *Satellite remote sensing applications in biometeorology: A review. Remote Sensing*, 12(18), 2981. doi: 10.3390/rs12182981;
[28] W. P. Menzel, (2019), *Satellite meteorology and biometeorology: An overdue integration*, International Journal of Biometeorology, 63(5), 603-609. doi: 10.1007/s00484-019-01704-z;
[29] C. S. B. Grimmond,& T. R. Oke, (2002), *Urbanization and global environmental change: local effects of urban warming*, The Geographical Journal, 168(4), 293-297;
[30] S.Hajat & T. Kosatky, (2010), *Heat-related mortality: a review and exploration of heterogeneity*, Journal of Epidemiology and Community Health, 64(9), 753-760;
[31] N. Kántor & A. Kovács, (2019), *Thermal comfort and heat stress risk in urban open public spaces–A review of assessment methods and metrics. Sustainable Cities and Society*, 47, 101469;
[32] T. R. Oke, G. T. Johnson & D. G. Steyn, (2011), *Thermal environment of urban areas*, Wiley Interdisciplinary Reviews: Climate Change, 2(5), 657-663;
[33] M. Santamouris, (2014), *Urban climate, heat island and sustainability: a review of strategies*. Sustainability, 6(2), 826-855;
[34] J. Tan, Y. Zheng, X. Tang, C. Guo, L. Li, & G. Song, (2010), *The urban heat island and its impact on heat waves and human health in Shanghai*, International Journal of Biometeorology, 54(1), 75-84;
[35] https://landsat.visibleearth.nasa.gov/view.php?id=147400.

ISSUES ON QUADCOPTER DESIGN CUSTOMIZED FOR URBAN AERIAL SURVEILLANCE

Irina-Carmen ANDREI[*], Gina Florica STOICA[**], Nicoleta CRIȘAN[**], Delia PRISECARU[**], Cristian STOICA[***], Anca GRECULESCU[**], Javier LINARES[****], Timothee Pol DUCROST[*****], Alexis BILLEREY[******], Bastien FONTANA-CASTETS[*******], Radu MIHALACHE[**]

[*]I.N.C.A.S. – National Institute for Aerospace Research "Elie Carafoli", Romania (andrei.irina@incas.ro)
[**]"Politehnica" University of Bucharest, Romania (gina.stoica@upb.ro, nicoletacrisan@upb.ro, delia.prisecaru@upb.ro, radumihalache500@yahoo.com)
[***]COMOTI – Romanian Research and Development Institute for Gas Turbines, Bucharest, Romania (cristian.stoica@comoti.ro)
[****]Glasgow Caledonian University, Glasgow, Scotland, United Kingdom of Great Britain and Northern Ireland (jlinar200@caledonian.ac.uk)
[*****]Ecole Polytechnique de l'Université Francois Rabelais de Tours, France (timothee.ducrost@etu.univ-tours.fr)
[******]I.M.T. - Institut Mines Telecom, l' École Nationale Superieure des Mines d'Alès, France (alexis.billerey@mines-ales.org)
[*******]E.N.I.T. - l' École Nationale des Ingénieurs de Tarbes, France (bastien.fontanacastets@enit.fr)

DOI: 10.19062/1842-9238.2022.20.2.2

Abstract: *The topic of this paper is in line with the efforts to reduce the spread of the pandemic effects; the objective is to design a quadcopter meant to perform urban aerial surveillance, focused on monitoring the urban traffic of cars and monitoring the traffic of groups of people, who should not gather in groups larger than three persons. The specificity of the work is given by the requirements of the European Project Semester EPS, where international teams of students actively experience a multidisciplinary and multicultural project for one semester in another university. This opportunity has allowed them to develop research and industrial partnerships. To this purpose, the approach provided by the I.N.C.A.S. as Research Partner is oriented towards Problem Based Learning and Project Organized Learning. The University as Organizer provides Project Related Courses and complementary Project Organized Learning. The research was oriented towards the customized design of a drone able to efficiently achieve the objective. The benefits of the research project are related mainly to the potential applications of the drone, with a good effect to cost ratio and to allowing the students to subsequently acquire valuable professional knowledge and experience from this research project.*

Key words: *Quadcopter, design, urban aerial surveillance, mobile/ car and people group traffic monitoring, Problem Based Learning, Project Organized Learning.*

1. INTRODUCTION

The present paper presents the study of the possibility of using drones as part of the COVID-19 lockdown monitoring system. Quadcopters had to be assessed in order to motorize crowds of people and enforcing safety requirement. The present city surveillance system was also studied and assessed. Possibilities of using quadcopter for achieving city surveillance were depicted and legal aspect was highlighted.

Afterward, computer vision and its application on Unmanned Aerial Vehicle's (UAV) for people counting were presented.

Two types of quadcopters can be distinguished: public and professional quadcopters.

Table 1 – Public and professional drones

Type	Public	Professional
Control	Remote/Smartphone Autopilot	Remote Autopilot
Price	Dozens of euros	Thousands of euros

In the last decades, quadcopters were mainly used by the military for reconnaissance and surveillance of dangerous areas or groups of people. But nowadays, they are very useful during lockdown situations [3], [4].

-study of lockdown's influence on global warming and air pollution measurement;

-give assistance or prevent emergencies;

-remind people of the exit instructions;

-monitor stores and vehicles.

Experimentation with people recognition using YOLO algorithm proved the ease of employing it. Studying the portfolio of available quadcopters on the market and making a requirement table lead to choosing the best UAV to monitor people in the street. Subsequently, an application case of city surveillance was made in Drumul Taberei, Bucharest, Romania. Deployment of the monitoring system has been studied. A MATLAB simulation of an UAV evolving in Drumul Taberei area and simulating people counting and detection allowed to experiment on the system.

A Quadcopter is a small flying object that has four arms, belonging to the UAV category. It is commonly also called "multirotor helicopter" because it is composed of four propellers allowing the Quadcopter to be vertically lifted. Quadcopters use the same physical phenomenon as helicopters which is the thrust as shown in Fig. 1.

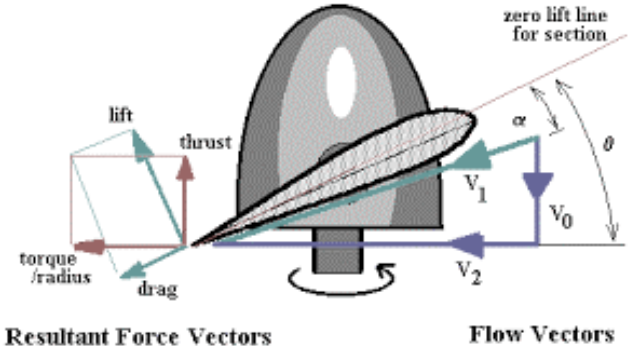

FIG. 1 – The thrust analysis of a propeller

In addition to thrust, Quadcopters use two clockwise and two counterclockwise propellers to achieve the three basic movements: Go forward, back, left, right / Turn left, right / Take off, land as illustrated in Fig. 2.

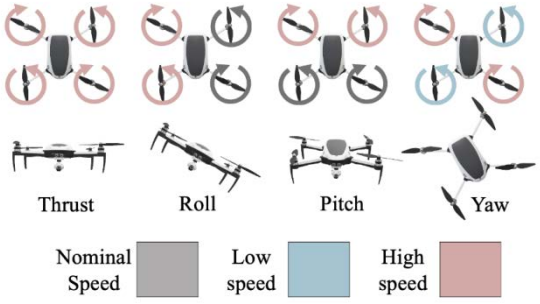

FIG. 2 The possible movements of a quadcopter

2. METHODOLOGY

2.1 Building the model

The first thing in order to create a model of the drone it is needed a block diagram to recreate the whole system. The simplest version of the system would be the one shown in Fig. 3.

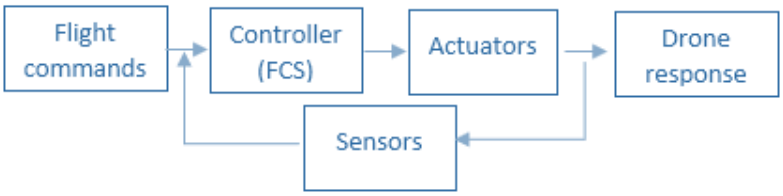

FIG. 3 Block diagram of a drone as a system

Thanks to Simulink this can be modelled into MATLAB using very similar diagrams and then include all the calculation blocks inside of them. This is illustrated in Fig. 4.

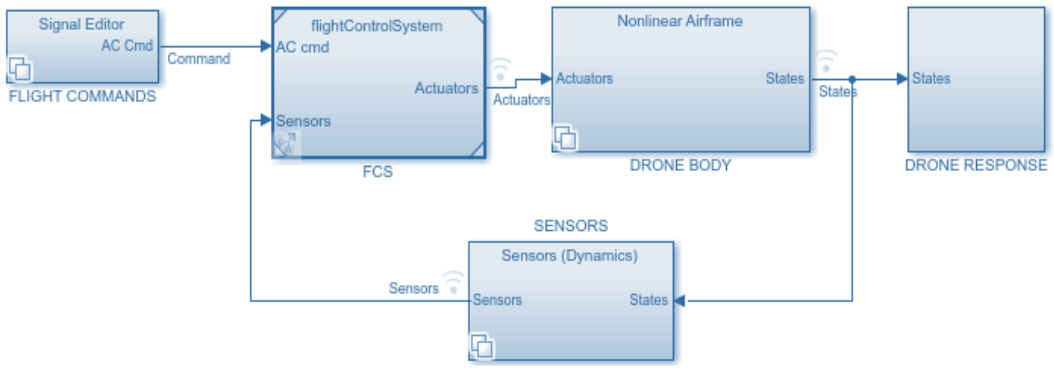

FIG. 4 Simplified Simulink model [8]

The flight commands are grouped in a block and include the pre-set settings, flight navigation paths or could represent just the remote controller of the quadcopter. That is the input for the closed loop.

The flight control system (FCS), also known as controller, it is the heart of the system. At this level, all Proportional-Integral-Derivative controller (PID) adjust the behaviour of the drone if needed and control all the actuators to ensure that the response of the system is as accurate and smooth as possible. This block also receives the feedback of the sensor to compare the actual flight parameters to the reference ones set in the flight commands block.

The drone actuators are the 4 four motors of the propellers, which receive the signal from the controller depending on the action needed (if needed).

The drone response represents the actual output of the system. Basically, it is what the drone is doing. In Simulink this block includes the 3D representation of the quadcopter.

Along with the controller, the sensor is one of the most important elements of the system. It acts as the feedback, providing the actual situation to the FCS in order to obtain the most accurate response.

Summing up, the close loop formed by the FCS, actuators and the sensors, are the ones processing the input in order to get the output as close as possible to the instructions given.

2.2 Simulation Validation and Limits

A simulation is a duplication of a real-world scenario, using a computer. This process of mathematical modeling is used to foretell the behavior or the consequence of the studied scenario. Simulations are extremely helpful for different reasons. For example, drone behaviors can be simulated without the need to operate or to have access to a real drone. Other notable reasons for the prevalent usage of computer aided simulations are as follows:

- simulations involve lower costs and are done way faster than real world experiments;
- simulations are very flexible, any input or variable can be changed easily;
- everything can be done without harming the environment or the persons involved.

The limits of a simulation are basically it's downsides or disadvantages. Most of these refer to the human operator. The main disadvantages of simulations are:

- very high processing power needed for complex models;
- building a model needs experience and special training;
- difficulties in interpretation of the result might appear;
- any error in the model or the inputs can propagate in a wrong result.

A Sense and Avoid algorithm is illustrated by A. Strobel and M. Schwarzbach [9] ,,with upsides and downsides of the approach". The result of the simulation was that once anything enters the "Threat Region", the map turns red and an avoidance maneuver begins. As a conclusion, the two limitations of this approach were that it only works with a single object entering the "Threat Region", with the other one being that even a single intruder has to maintain a constant speed and execute simple maneuvers in order for the algorithm to work properly

The main steps of achieving a good simulation:

1) Gathering accurate data that reflects the real world. (i.e.: equations or forces involved)
2) Creating algorithms (mathematical formulas) that can further generate data from what has been inputted
3) Generating ways to display the outcome (output): graphs, animations, etc.
4) Verify and validate results.

2.3 Obstacle Detection

Midair collision avoidance is a critical task that is mandatory to guaranty a safe airspace. Nowadays, airborne systems and ground systems participate in this collision avoidance for aviation. With the fast development of drones and quadcopters as depicted in [1], more quadcopters are sharing the airspace. To be able to fully use UAVs at their maximum capacities and keep airspace safe [10], the next challenge is to be able to develop a reliable collision avoidance system for UAVs. This question was already studied 20 years ago [11] but still as no answer today for the full portfolio of existing and yet to come UAV's.

The small unmanned aerial vehicles need to be visible [12] for all users of the airspace but also to be able to seek their surrounding in order to perform an avoidance if needed.

All algorithm work on the same principle Figure . They are based on deep learning and there for huge quantities of data are required to train the model. However, they can easily be trained for specific purpose, for instance, detecting people from a quadcopter. The only requirement is having a huge quantity of accurate data. Comparison of Region-based Convolutional Neural Networks (R-CNN), Faster R-CNN, You Only Look Once (YOLO) and Single Shot Detector (SSD) were conducted on different data set [5].

YOLO method was chosen because it's one of the fastest methods (it allows 30 images per seconds on a high-end computer) and pretrained models are available for experimentation.

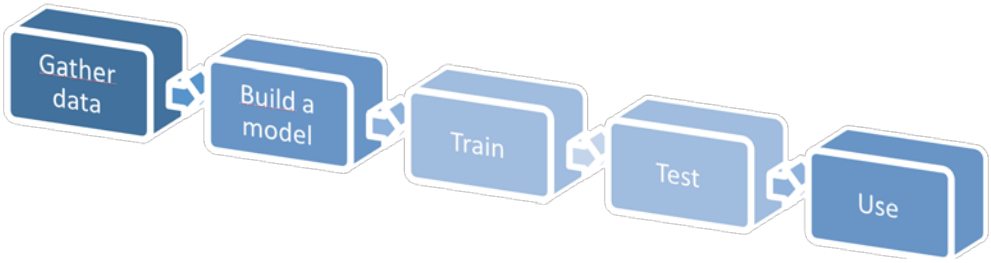

FIG. 5 Principle of deep learning

3. RESULTS

YOLO is composed of one model and a set of weights obtained from training the model on a dataset. Many models and sets of weights trained on different dataset are available. Tiny YOLO was used for experimentation as it is faster and works fine on a Computer Processing Unit (CPU). Set of weights is only 44Mo as for YOLOV3, weights are 252Mo. Tiny YOLO model is much simpler therefor the results are far below YOLOV3 capacities.

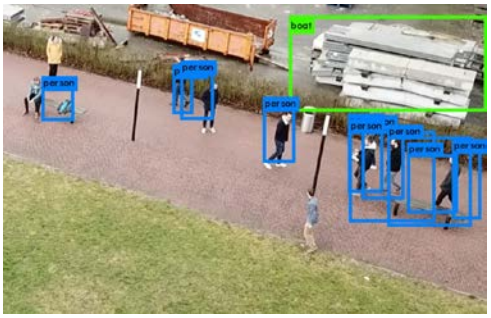

FIG. 6 Prediction on people from behind and from one side, case # 1

Data provide from two different dataset realized for studying computer vision for quadcopters. One dataset [8] is a video taken within an institute and shows people walking next to grass. The other [9] is a set of pictures taken from quadcopters in various areas, showing people and cars, Fig. 6 and 7.

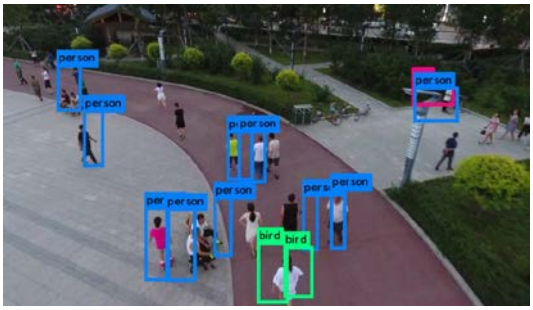

FIG. 7 Prediction on people from behind and from one side, case # 2

Experimentation highlights the limits of computer vision from quadcopter without a proper trained model. The many angles and point of views that provide quadcopter make images harder to analyze with common models. To increase people detection rate, fitting the model with a good dataset is required.

Experimentations are based on picture analysis. A video is just a set of pictures. Taking this into account, for performing real time analysis the same technique can be used. A Graphic Processing Unit (GPU) such as Nvidia GTX1080TI is required as it dedicated to the job with more processing cores. According to [7] YOLOV3 perform 45 images per seconds analysis while running on a Titan X GPU (Titan X is a high end GPU released in 2016).

Video analysis can be performed onboard, but the system is energy-consuming, so it impacts quadcopter performances. Moreover, small GPUs are expensive. The best option is to perform the analysis on the ground. Quadcopter's video feed can be sent to a ground unit and object detection is to be run there. Human operator is notified when a forbidden behavior is detected, and afterwards the operator can take the control of the quadcopter to analyze the situation, as sown in Fig. 8.

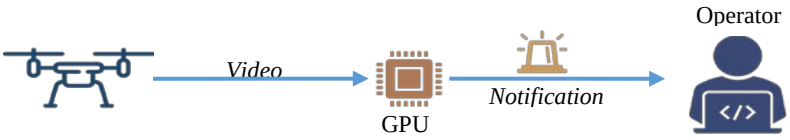

FIG. 8 Live video analysis and operator notification workflow

After detecting people on frame, the next step is to be able to measure if safety distance are respected. As the quadcopter position is not always the same, a ground projection can be done and analysis afterward. The society dragonfly has been chosen by U.S. government to develop pandemic drones with such abilities [10]. The main concern about such usage of technology is about people privacy and public acceptence. A lot of people are showing there objection to such usage. The society also claimed being able to detect people coughing, sneezing and even measure heartbeat.

Another application of computer vision to COVID-19 is mask detection. Computer vision expert Adrian Rosebrock [11] has been able to train a model that recognize if someone is wearing a mask or no. He released a tutorial on the 4th May 2020.

This fast reaction emphasize how quadcopters with computer vision capabilities can be versatile and perform many different tasks.

Different applications can be made of quadcopters with computer vision capabilities. This system can be used to analyze where population is taking risks and reinforcing security after analyzing. But also, it can be used to enforce law and to give fines by using face recognition algorithm or sending police to the place where restrictions are not respected.

In computer vision, HD cameras are usually used to captures the iamges. But different kind and sensors can be applied. The model used and the training methods differ, however, the principle stays the same. Good acquisition device and high-quality products are the keys to enable reproducible analysis.

3.1. Components

Sensors: - Ultrasonic

As the name indicates, ultrasonic sensors measure distance by using ultrasonic waves. The senor head emits an ultrasonic wave and receive the waves reflected from the

obstacle. It measures the distance between the emitter and the obstacle by calculating with the time spends between emission and reception, and the sonic speed.

- Infrared

Infrared sensor is a simple electronic device, which emits and detects IR radiation in order to find out certain objects/obstacles in its range. Some of its features are heat and motion sensing. It is used in a wavelength between 0.75 to 1000μm, which falls between visible and microwave regions of electromagnetic spectrum. There are three categories: near infrared - 0.75μm to 3 μm, mid infrared - 3 μm to 6 μm, up far infrared – > 6 μm.

Mm wave is an extremely valuable sensing technology for detection of objects and providing the range, velocity and angle of these objects. It is a contactless technology, which operates in the spectrum between 30GHz and 300GHz. Due to the technology's use of small wavelengths it can provide sub-mm range accuracy and is able to penetrate certain materials such as plastic, drywall, clothing, and is impervious to environmental conditions such as rain, fog, dust and snow. TI has two families of mm Wave sensors, AWR mm Wave sensors for automotive and IWR mm Wave sensors for industrial, drones and medical applications.

Light Detection and Ranging (LiDAR) sensors use light energy, emitted from a laser, to scan the ground and measure variable distances. The result is a rich set of elevation data that can be used to produce high-resolution maps and 3D models of natural and manufactured objects.

The key features of HD for video surveillance are: Maximum HD resolution is 2.1MP, maximum megapixel resolution is 20MP or more with 5MP cameras are common from numerous vendors, HD video format is 1280 x 720 or 1920 x 1080 (megapixel cameras can offer many more formats), HD aspect ratio is 16:9 (compared to 5:4 or 4:3 in other surveillance cameras), HD frame rate is 30/25 (where megapixel cameras are often 3 - 15 frames), HDTV has quality compliance standards (where megapixel simply specifies the number of pixels)

In addition to the terrestrial forces, as a support for surveillance, aerial methods are normally used by security forces. The most common method used until now, is the helicopter, which has a relatively high operational cost [12]. This type of aircraft also has the limitations of flight altitude, large area to take off and landing or high cost among other disadvantages. Due to its large size and levels of noise, helicopter cannot fly at low altitudes above the people while an UAV can fly closer, respecting always the legal distances. Besides the altitude restrictions, for the task of taking off or landing, a helicopter needs around two hundred square meters [13] while a quadcopter can easily take off in less than one. Moreover, transporting an unmanned quadcopter from one area to another is considerably cheap. Since the drone can be carried in any kind of transport easily, while a helicopter normally flies from A to B, having a greater cost. These reasons along with the lower operator risk of an unmanned vehicle, have made it an ideal resource in the field of aerial surveillance. It is the brain of the Quadcopter. It pilots the Quadcopter. We can see two components: a flight controller (FC, in red on Fig. 31) and a Global Positioning System (GPS, in blue on Fig. 9). Equipped with sensors, the FC is the link between the pilot and the Quadcopter. It analyses the commands send by the pilot to control the speed of the rotors via the ESC. In addition, the GPS localizes the position of the Quadcopter to help it to follow a defined path.

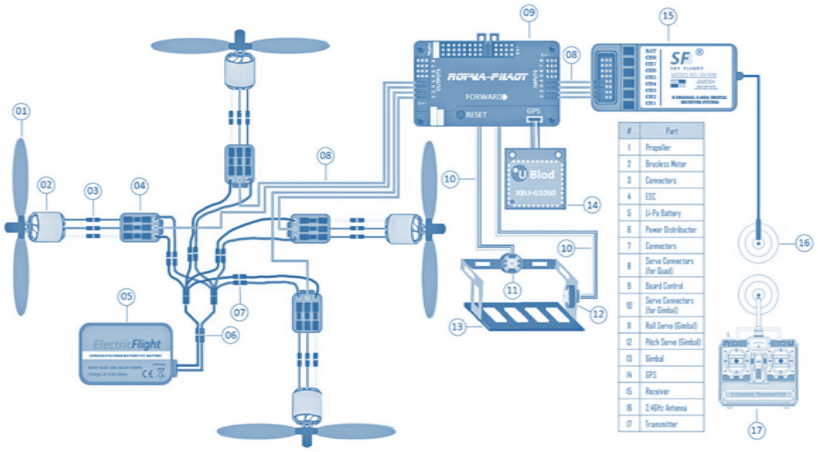

FIG. 9 Flight Controller and Global Positioning System implementation

Detect and avoid obstacles is the role of this block. The Collision Avoidance System (CAS) is equipped with some sensors or cameras catching in real time some information like shapes and their position in the space (Table 8). The analysis of the environment of the Quadcopter allows the collision avoidance system to determine if there is a risk of collision or not. Based on algorithms, the CAS can compute a new trajectory for the Quadcopter avoiding in security the obstacle.

This block can change according to the use of the Quadcopter. The principle is to use dismountable devices. Therefore, this block performs different functions related to the employed devices as illuminate, communicate or filming.

With the aim of simulating the way the UAVs work around the city, Matlab environment, and more specifically, the driving scenario tool were used.

Fig. 10 shows the trajectory followed by the drone through the streets of the chosen area of the city.

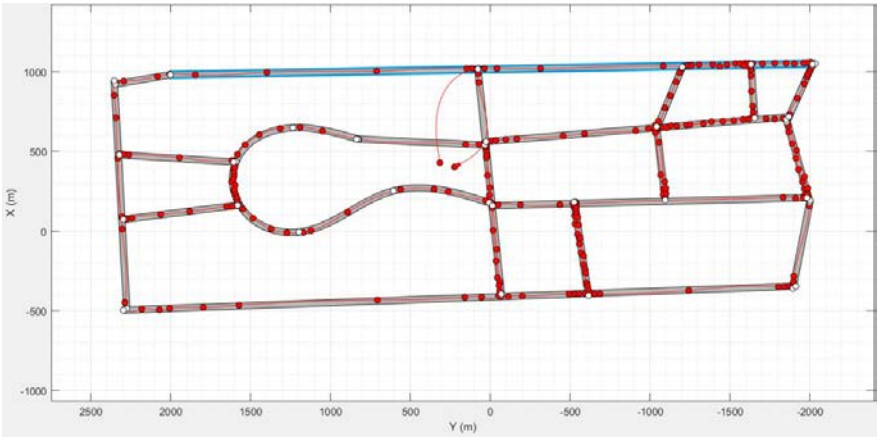

FIG. 10 Build trajectory simulation in MATLAB, based on Google Earth 2020 extraction of the streets layer of the district *Drumul Taberei* of Bucharest.

As explained in the previous paragraphs, one of the purposes of the system is to detect if there is a group of people larger than 3 or not. Figure 11 shows an example of a non-alert situation in comparison with an alert one. It detects the persons but since the condition was a group of at least person, the patrol would continue as normal.

FIG. 11 Non-alert detection vs. alert detection

4. CONCLUSIONS

The main goal of the EPS project was to study the possibility of using drones as part of the COVID-19 lockdown monitoring system. Quadcopters were studied for monitoring crowd and enforcing safety requirement.

Actual city surveillance systems were studied. Possibilities of using quadcopter for achieving city surveillance were depicted and legal aspect were highlighted. Afterward, computer vision and its application on UAV's for people counting were presented. Experimentation with people recognition using YOLO algorithm proved the ease of employing it. Studying the portfolio of available quadcopters on the market and making a requirement table lead to choosing the best UAV to monitor people in the street. Subsequently, an application case of city surveillance was made in Drumul Tabarei, Bucharest, Romania. Deployment of the monitoring system has been studied. A MATLAB simulation of an UAV evolving in Drumul Tabarei area and simulating people counting and detection allowed to experiment on the system.

Autonomous fleet of quadcopter equipped with HD cameras are a good mean for monitoring citizens in the street and showed promising results in terms of accuracy, reliability and safety. However, this system has to deal with strict legal aspects that evolve fast due to the recent development of quadcopters. Moreover, UAVs usage for population monitoring confronts people's privacy and citizen could show objection to the system and cause its destruction. Laws have to evolve at European model to ensure the development of city monitoring systems using quadcopters.

ACKNOWLEDGEMENTS

This paper represents an improved and extended version of the paper presented at the International Conference of Aerospace Sciences "AEROSPATIAL 2020", Bucharest, 15 - 16 October 2020, (Virtual Conference), Section 2 – Flight Mechanics, Paper S2.3.

This research was developed within the research partnership between [4]"POLITEHNICA" University of Bucharest, Faculty of Mechanical Engineering and Mechatronics and INCAS - National Institute for Aerospace Research "Elie Carafoli", through the EPS – European Project Semester programme.

The team of Science Advisors and Coordinators: Irina-Carmen ANDREI, Gina Florica STOICA, Nicoleta CRIŞAN, Delia PRISECARU, Cristian STOICA, Anca GRECULESCU.

The team of Tutors: Irina-Carmen ANDREI (INCAS Tutor), Nicoleta CRIŞAN (UPB Tutor).

We would also like to show our gratitude to Dr. Dragos-Daniel Ion-Guță, Head of Systems Division, and to all the research team members from INCAS, for supporting the EPS students groups and for providing expertise that greatly assisted the project research.

REFERENCES

[1] Web of Science, *Drones records analysis*, 2020. [Online]. Available: https://wcs.webofknowledge.com/RA/analyze.do?product=WOS&SID=F4CcNzvft8OyxbvZzDS&field=TASCA_JCRCategories_JCRCategories_en&yearSort=false;
[2] Institute Project Management, PMBOK® Guide – Sixth Edition. 2010;
[3] I. Mihajlovic, *Everything You Ever Wanted To Know About Computer Vision*,"2019. [Online]. Available: https://towardsdatascience.com/everything-you-ever-wanted-to-know-about-computer-vision-heres-a-look-why-it-s-so-awesome-e8a58dfb641e. [Accessed: 12-May-2020];
[4] S. Remanan, *Beginner's Guide to Object Detection Algorithms*, 2019. [Online]. Available: https://medium.com/analytics-vidhya/beginners-guide-to-object-detection-algorithms-6620fb31c375. [Accessed: 18-May-2020];
[5] MC.AI, "Object detection: speed and accuracy comparison (Faster R-CNN, R-FCN, SSD and YOLO)," 2018. [Online]. Available: https://mc.ai/object-detection-speed-and-accuracy-comparison-faster-r-cnn-r-fcn-ssd-and-yolo/. [Accessed: 18-May-2020];
[6] J. Redmon, S. Divvala, R. Girshick, and A. Farhadi, *You only look once: Unified, real-time object detection*, Proc. IEEE Comput. Soc. Conf. Comput. Vis. Pattern Recognit., vol. 2016-Decem, pp. 779–788, 2016;
[7] J. Redmon and A. Farhadi, *YOLOv3: An Incremental Improvement*, 2018;
[8] VisDrone, *Object detection - VisDrone2020-DET dataset*, 2020. [Online]. Available: http://aiskyeye.com/download/object-detection/. [Accessed: 25-May-2020];
[9] UAVision, *3rd International Workshop on Computer Vision for UAVs* [Online]. Available: https://sites.google.com/site/uavision2019/challenge. [Accessed: 25-May-2020];
[10] *Dragonfly Selected to Develop 'Pandemic Drone*, 2020. [Online]. Available: https://insideunmannedsystems.com/draganfly-selected-to-develop-pandemic-drone/. [Accessed: 22-May-2020];
[11] Adrian Rosebrock, *COVID-19: Face Mask Detector with OpenCV, Keras/TensorFlow, and Deep Learningitle*, 2020. [Online]. Available: https://www.pyimagesearch.com/2020/05/04/covid-19-face-mask-detector-with-opencv-keras-tensorflow-and-deep-learning/. [Accessed: 25-May-2020];
[12] Breaking News, *Are UAS More Cost Effective Than Manned Flights?*, 2013. [Online]. Available: https://www.auvsi.org/are-uas-more-cost-effective-manned-flights;
[13] EASA, *EASA*, 2020. [Online]. Available: https://www.easa.europa.eu;
[14] Dimension.Guide, *Dimensions.Guide*. [Online]. Available: www.dimensions.guide. [Accessed: 26-May-2020];
[15] T. Guardian, *How dangerous are drones to aircraft*?, 2018. [Online]. Available: https://www.theguardian.com/technology/2018/dec/20/how-dangerous-are-drones-to-aircraft.
[16] CYIENT, "CYIENT," 2020. [Online]. Available: https://www.cyient.com;
[17] F. D'Souza, "Goa cops use drones for aerial surveillance during COVID-19 lockdown," 2020. [Online]. Available: https://timesofindia.indiatimes.com/life-style/spotlight/goa-cops-use-drones-for-aerial-surveillance-during-covid-19-lockdown/articleshow/75252128.cms;
[18] Z. Doffman, *Coronavirus Spy Drones Hit Europe: This Is How They're Now Used*, 2020. [Online]. Available: https://www.forbes.com/sites/zakdoffman/2020/03/16/coronavirus-spy-drones-hit-europe-police-surveillance-enforces-new-covid-19-lockdowns/#76ae2ac7471c;
[19] T. Mogg, *French police the latest to use speaker drones to enforce coronavirus lockdown*, 54, 2020;
[20] News, *China uses talking drones to scold citizens amid coronavirus lockdown*, 2020. [Online]. Available: https://www.abc.net.au/news/2020-02-03/china-uses-talking-drones-to-scold-citizens-amid-coronavirus-lo/11926116;
[21] Direcția Generală de Jandarmi a Municipiului București, *Informaţii Privind Utilizarea Şi Folosirea Dronelor În Condiţii De Legalitate*, 2020. [Online]. Available: http://www.jandarmeriabucuresti.eu/2018/11/29/informatii-privind-utilizarea-si-folosirea-dronelor-in-conditii-de-legalitate/.

LIGHT PAYLOAD QUADCOPTER DESIGN FOR THE TRANSPORTATION OF ESSENTIAL GOODS TO PEOPLE IN SELF-ISOLATION

Irina-Carmen ANDREI[*], Gina Florica STOICA[**], Nicoleta CRIŞAN[**], Delia PRISECARU[**], Cristian STOICA[***], Anca GRECULESCU[**], Dries BIERENS [****], Adrien THIBAULT [*****], Vincent BURRE-ESPAGNOU [******], Martin DILLINGER [*******], George ZDRU [**]

[*]I.N.C.A.S. – National Institute for Aerospace Research "Elie Carafoli", Romania (andrei.irina@incas.ro)
[**]"Politehnica" University of Bucharest, Romania (gina.stoica@upb.ro, nicoletacrisan@upb.ro, delia.prisecaru@upb.ro, radumihalache500@yahoo.com)
[***]COMOTI – Romanian Research and Development Institute for Gas Turbines, Bucharest, Romania (cristian.stoica@comoti.ro)
[****] Universiteit Antwerpen, Antwerp, Belgium (dries.bierens@student.uantwerpen.be)
[*****]Institut Universitaire de Technologie de Dijon, France (adrien.thibault11@gmail.com)
[******] E.N.I.T. - École Nationale d'Ingénieurs de Tarbes, France (vincent.burreespagnou@enit.fr)
[*******]Czech Technical University, Prague (Czech Republic, martin.dill@seznam.cz)

DOI: 10.19062/1842-9238.2022.20.2.3

Abstract: *A quadcopter, also called a quadrotor helicopter or quadrotor is a multirotor helicopter that is lifted and propelled by four rotors. In case of lockdown or self-isolation, companies as well as governments can make use of unmanned aerial vehicles equipped with obstacle detection and collision avoidance technology. It is paramount to understand the importance of flight safety with unmanned aerial vehicles. If rules and restrictions are not followed because the user with the controller made an error or was unconscious, a sophisticated system will detect possible conflict and save the drone before collision. In this paper, a digital model was created using MatLab software, in order to analyze and understand how a quadcopter works in its environment. Using the trajectory tools, a well-defined trajectory is defined for a quadcopter in order to better represent its behavior during a light parcel transport assignment. The results obtained can be used to design a drone for the delivery of small packages containing essential goods for people in self-isolation.*

Keywords: *quadcopter design, safety issues, numerical simulation*

1. INTRODUCTION

A quadcopter (Fig. 1), also called a quadrotor helicopter or quadrotor is a multirotor helicopter that is lifted and propelled by four rotors. Quadcopters are classified as rotorcraft, as opposed to fixed-wing aircraft, because their lift is generated by a set of rotors (vertically oriented propellers).

Quadcopters generally use two pairs of identical fixed pitch propellers; two clockwise (CW) and two counter clockwise (CCW). These use independent variation of the speed of each rotor to achieve control. By changing the speed of each rotor, it is possible to specifically generate a desired total thrust; to locate for the centre of thrust both laterally and longitudinally; and to create a desired total torque, or turning force. [1]

FIG. 1 Quadcopter design

In case of lockdown or self-isolation, companies as well as governments can make use of unmanned aerial vehicles equipped with obstacle detection and collision avoidance technology. By having the quadcopter equipped with various types of sensors (vision, ultrasonic, infrared, etc.) (Fig. 2a) and by creating a database with all stores and pharmacies within a certain area, it is possible to have essential items delivered to one's residence. Drones available, at the moment, can deliver payloads up to five kilograms and over a distance up to twenty-five kilometers (Fig. 2b).

One of the most important elements of this concept is the obstacle detection and collision avoidance technology. For any autonomous driving vehicle, be it a car, robot, or drone, to be able to detect obstacles and avoid collisions, it requires a number of complex technologies working together to create an integrated system. This entails many various sensors and software programming which include mathematical modelling, algorithms, machine learning and aspects of SLAM technology.

Most of the time, drones are equipped with sensors fusion. This is a process by which data from several different sensors are "fused" to compute something more than could be determined by any one sensor alone. Sensor fusion is a subcategory of data fusion and is also called multisensory data fusion or sensor-data fusion.

FIG. 2 (a) Position of sensor on a drone, (b) Flight pattern of a drone.

A quadcopter could have the best sensors available, but without software and algorithms, they are of no use. An algorithm is a detailed step-by-step instruction set that aims to solve a particular problem, in this case the problem of avoiding both moving and stationary object, detected by the sensors. Depending on the algorithm, the quadcopter will be able to compare real time data from stored referenced images of objects. There is a multitude of techniques which can be used for obstacle avoidance, but usually the best technique depends on the specific environment and it differs depending on type of device (cars/drones/robots). [2]

FIG. 3 "Air Prime" project by Amazon

2. QUADCOPTER DESIGN

While designing a quadcopter four aspects must be taken in consideration: the axis, the mass and inertia and the number of rotors. One of the most important features of an unmanned aerial vehicle is its mobility on all directions. This means that the quadcopter is able to move along the X-axis, which points in the direction along the nose of the quadcopter, along the Y-axis, which points to the right of the quadcopter, and along the Z-axis, which point downwards following the right-hand rule. All of the quadcopter's axis are centred in its centre of gravity (Fig. 4).

FIG. 4 Position of the three axis for the quadcopter's movement

In terms of mass and inertia, it is assumed that the whole body of the vehicle works as a particle. A quadcopter's rotors are located parallel to the XY plane and on the axis going through the centre of gravity at 45 degrees and -45 degrees. Each of the rotor rotate in a different direction in order for the quadcopter to keep its balance during flight; the first and the third rotors rotate positively with respect to the Z-axis, while the second and the fourth rotors rotate negatively with respect to the body's Z-axis. (Fig.5) [4]

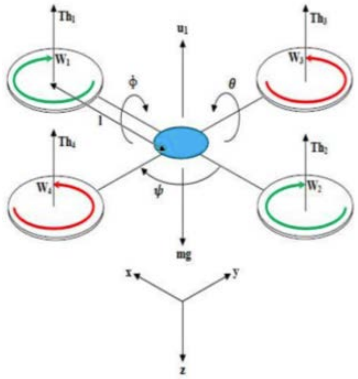

FIG. 5 Visual representation of the rotors movement of rotation in respect to the three axis

The parameters of the rotors (the degree in respect to X and Y axis, as well as the direction of the rotation) may depend on the number of rotors the unmanned aerial vehicle has [5]. The last, but not least aspect which must be taken into consideration when designing a quadcopter is its purpose, depending on that the vehicle might need special night-vision cameras and/or sensors, temperature sensors, etc. as well as a control unit, made of individual controllers for pitch/roll, yaw, and the quadcopter's position on the X, Y, and Z axis.

In conclusion, the quadcopter is an efficient and elegant design, and is a very popular layout for an unmanned aerial vehicle due to the fact it is relatively a simple design, it is symmetrical, and inexpensive to manufacture compared to other multi-rotor designs.

3. SAFETY CONCERNS IN DRONE OPERATION

This topic serves as a guidance material for software engineers. This section describes safety hazards of flying with drones, especially when a drone is controlled by an inexperienced person without knowledge of safety instructions. Then, information about possible collisions is provided. Consequently, there is a proposal for future systems improvements in order to achieve safe flight without collisions with ground, obstacles or aircraft. A summary of which detection and collision systems shall be developed and which ones are currently too complicated to create is presented in this section. Mentioned content can help students to understand importance of safe flight of unmanned aerial vehicles. If rules and restrictions are not followed because the user with the controller made an error or was unconscious, sophisticated system will detect possible conflict and save the drone before collision.

Safety is always the most important thing to consider in aviation. Unmanned aerial vehicles have rapidly spread over the world. Drones (quadcopters) are still considered to be children's toys. In fact, mid-air collision of a drone with aircraft is really dangerous accident (Fig. 6). It causes harm to the aerodynamic shape of the aircraft and it can even lead to engine destruction. That is the reason why drones have to be totally separated from other air traffic [13].

FIG. 6 Mid-air collision with a drone damaged aircraft's nose

The root problem of using drones is that drones are controlled by inexperienced and unlicensed people in contrast to highly regulated civil aviation. The task for regulatory organs is to determine how and where are drones are permitted to fly. They must compromise between undisturbed flying of drones and safety of civil aviation. Legislation is a bit late due to the fast development of drones. Restrictions are being established in order to regulate airspace protection. There are some rules that should be followed:

- Drones shouldn't fly over people.
- Drones shouldn't fly over private property without permission of its owner.

- Controller should always see his/her drone and keep direct eye contact from ground.
- Drones shouldn't fly in bad weather conditions, such as low visibility, wind, thunderstorm etc.
- Drones shouldn't fly close to obstacles, such as houses, trees, roads etc.
- Drones shouldn't fly in proximity to airports and restricted areas.
- Drones shouldn't fly in significant heights close to airspace (usually no more than 120 meters above ground). [13]

To prove that the lack of restrictions and regulations regarding drone usage, Fig. 7, is a representation of a drone that failed to hover and crashed over ski slope. The respective drone almost hit an athlete that was skiing at that moment, an event which could have had very bad consequences. That is why there must be strict rules and regulations, as well as fines or punishment for those who fail to comply with the rules, this is also why in some countries, and owners of drones weighting more than 250 grams must be registered by aviation authority.

In December 2018, Gatwick Airport stopped its operation for 24 hours because some drones were flying close to the airport. This deliberate incident affected more than 760 flights and it encouraged airports to build drone detectors and manufactures to work on advanced systems as well.

FIG. 7 Drone crashing over ski slope

The best way to avoid collisions is to separate different means of transport and create simple restrictions that can be easily followed. For future development and wide application of drones, however, it is important to integrate all traffic means together and share one airspace. This is a challenging idea and it will be very difficult to establish such a complex system. It will take a long time to solve this problem, but it might be possible with new technologies and more precise locators and sensors.

The reason why to achieve it is that for future drone delivery and other services, the restrictions are too strict and there is not enough space specified for drones exclusively. Drones can't fly too high currently and always must be seen visually. Drones are high technology devices and their function can be enhanced by sophisticated systems. The limit for installation these extensions is the need of light weight and low battery consumption. New systems include flight stabilization, precision flight, obstacle detection and manoeuvre resolution.

Which collisions can occur when drone is in the air? There are dangerous barriers (Fig. 8), some of them are even invisible, and the user must be aware of them. Drones should not fly close to these obstacles because it is unsafe for the drone itself or for other aircrafts. Various early warning systems for detecting hazards are in development.

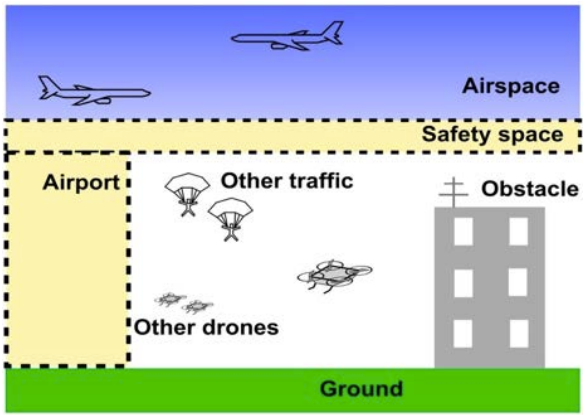

FIG. 8 Drone fly zones and obstacles

Protection against controlled flight into terrain or hard landing is mainly the controller's task. Drones usually have several sensors detecting nearby objects. If there is a downward sensor, a control unit is able to calculate a too fast decent close to the ground in cooperation with accelerometers. The majority of drones equipped with GPS locators can simply execute automatic smooth landings using the downward sensor.

Many unmanned aerial vehicles have already been equipped with obstacle detection systems. When a drone approaches an obstacle too fast, the system makes a resolution and lets the drone hover in sufficient distance from obstacle. The current limitation is in sensors. Sensors have limited ability to detect obstacles. They can detect an object that is as far as approximately fifty meters. It reliably detects obstacles as far as twenty-five meters. [15] Since maximum velocity reaches significant speed (about 20 meters per second), there is just a bit more than a second until impact. During this time, the control unit must process the inputs and stop the drone from moving toward obstacle. That is almost impossible at high speeds, to brake and avoid obstacle collision. Another problem is that the sensors can't reliably detect shiny and reflective surfaces, don't work properly in darkness and do not detect very small, or thin objects (electric wires).

The key task for protection against collision with an obstacle is to improve sensors. The problem is short range and unreliability of object detection. Better sensor characteristics enable drones to detect obstacle earlier and stop them before collision. Other improvement could be looking into precise 3D database that anticipates obstacle location or scanning objects by camera remembering their exact shape and position in space (so called Simultaneous localization and mapping technology). [16]

Collisions with aircrafts can lead to very severe consequences. That is the reason why these two machines must not come together. Aircraft fly in segregated airspace. For drones it is prohibited to fly into airspace that is determined for aircrafts. Aircrafts are served by air traffic controllers (ATC) and all movements are based on air traffic controller's permission (clearance). There is no chance for ATC to handle drones because they aren't seen on a radar and human controllers aren't on board. Aircrafts can fly up to 250 knots (460 km/h) in lower altitudes and so sensors on a drone can't detect aircrafts. Pilots also can't see drones in time in order to perform a maneuver. Drones have to stay away from controlled airspace. Airspace usually starts 300 meters above ground level, drones shouldn't fly above 120 meters.

Airspace is controlled by human ATC and it will certainly remain like this more than 10 years ahead. Airspace should be more automated in future using free flight concept, but it won't enable drones to fly within airspace. Aircrafts use Traffic Collision Avoidance System (TCAS) to get rid of collision in case of ATC failure. Drones aren't concerned in this system. A possible idea is to install mode S receiver into drone. Mode S is a signal (information about position and height) transmitted by all big aircraft. The drone could find out that some aircraft is heading in its direction and the drone would immediately decent. However, in the following years drones must stay segregated from airspace. Another idea is to limit airspace a bit and create restricted areas for drones only or conditional routes, as military aircraft sometimes use. Drones equipped with precise altimeter could have limits to not fly above a stated level.

As aircraft take off and land on runways, not to fly too high by drones is not a sufficient condition. They can't fly close to an airport or close to other restricted areas, such as military areas or nuclear power stations. This negative trend is growing year to year and there is no satisfactory restriction to eliminate drones in airport proximity.

If a database with restricted areas exists, drones with GPS will know where is a boundary where not to fly. Such maps with restricted areas are created, it is not difficult to provide it to a drone control unit. The task is to enable access to this database and a lot of unintentional entries to airport areas will be simply prevented.

Small aircraft and parachute belong into this category. Presence of them close to ground is conditioned mainly by visual caution. Small aircraft should fly higher than drones shall. In busy traffic areas controllers of drones are usually warned by signs to not fly there.

It is not easy to solve these possible collisions that are based just on visual awareness. Other traffic is quite slow in low heights and so better sensors could be able to detect them and avoid collision. New sensors technologies will perhaps cope with distant flying object detection. These progressive technologies are for example ultrasonic sensors, time-of-flight sensors or Lidar (Light detection and ranging).

These collisions are not prevented unless obstacle detection system reveals resolution. Drones should be flown at low density traffic areas. Controllers shall guard theirs drone and shouldn't come closer to others.

Some automatic broadcast transponder could be developed and installed to all unmanned aerial vehicles. Other devices would calculate relative position to the particular drone and be aware of danger in case of air proximity. Then maneuver can be executed. Otherwise drones could send information about their position via datalink and share movements with drones in surroundings. There was a drone show during the Winter Olympic Games in Pyeongchang county in South Korea. 1218 drones cooperated to each other and made a perfect light show.

Vertical downward acceleration close to terrain shall be reduced. Modern drones can be equipped with a precise altimeter. The altimeter might be either radio altimeter that measures precise height over terrain even in high heights or barometric that provides altitude based on local pressure. A more reliable altimeter offers more automatic functions (for example flying at determined height above ground) and protects the drone against collision with the ground. On the other hand, such altimeters are significantly heavier and for cautious controllers a downward sensor is enough.

4. NUMERICAL SIMULATION AND CONCLUSION

In order to analyse and understand how a quadcopter works in its environment, a digital model was created using MatLab software. The model (Figure 9) is mainly composed of six independent blocks that communicate with each other:

- command block: command and control the quadcopter;
- sensors block: record the different data and variables that act on the quadcopter;
- environment block: subjecting the quadcopter to the different forces / constraints of our terrestrial environment;
- flight control system block: record and analyse the previous blocks in order to issue commands to the quadcopter;
- airframe block: analyse the quadcopter's behaviour in its environment;
- visualization block: communicating with the user using 3d models and sensors;

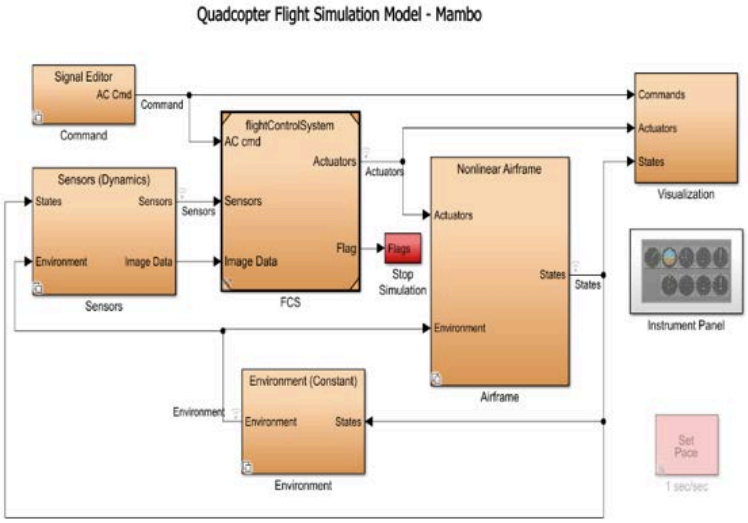

FIG. 9 Visualization of the six independent blocks

The main focus of this paper is on the command and visualization blocks; using the trajectory tools, a well-defined trajectory is defined for a quadcopter in order to better represent its behavior for a light parcel transport use. No fly zones are defined in order to restrict the quadcopter's flight path in some places (Fig. 10).

FIG. 10 MatLab visualization tool

In order to load this trajectory, it is necessary to switch the control mode to data so that the quadcopter can follow the different crossing points chosen beforehand. (Fig. 11)

For visualization, a 3D simulator as well as a control panel are used in order to analyze in real time the different variables of the quadcopter. (Fig. 12)

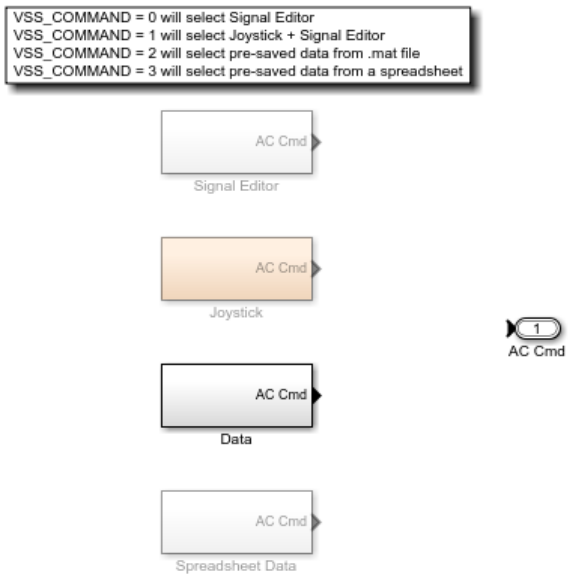

FIG. 11 MatLab software control model

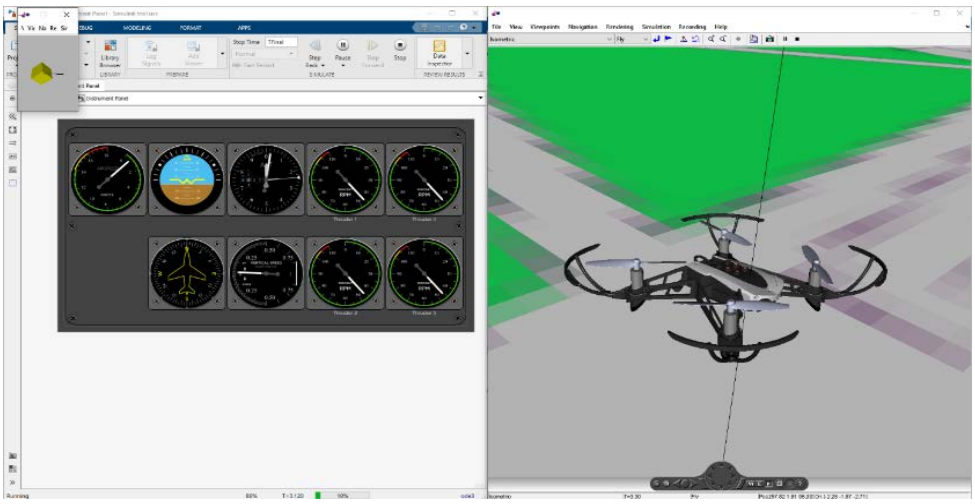

FIG. 12 MatLab software 3D simulator

In order to create the trajectory, a new tool from MatLab (Fig. 13), creating a more intuitive trajectory generator than the old one used for the first test. The new trajectory includes a take-off, a longitudinal forward movement, a transverse movement, a longitudinal backward movement and, finally, landing. The aim is to observe the behaviour of the quadcopter as well as the data differences with the first simulation.

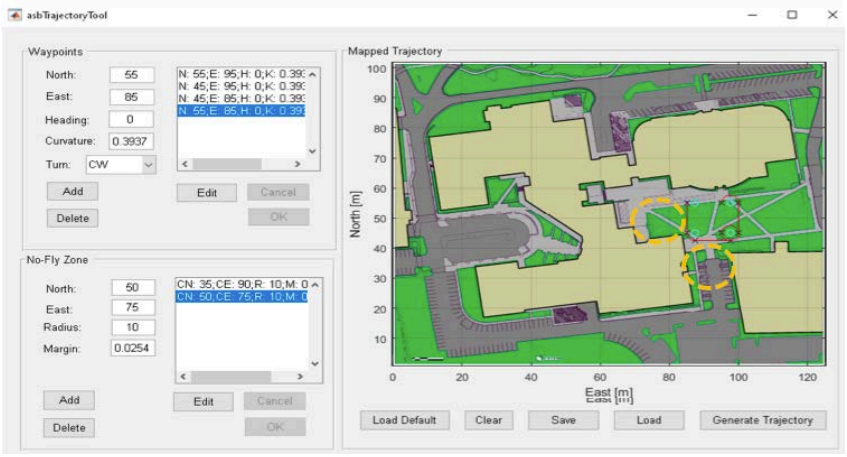

FIG. 13 MatLab tool for no-fly zone creation

The new tool, allows for the creation of no-fly zones, just as in reality. In this way, the drone will have to avoid those zones and use different trajectories that could be less efficient. The aim is to observe how the drone deals with the constraints of the no-fly zones, and as with the previous simulation, to analyse the data made available by the 3D simulation (Fig.14) in order to better understand how the drone functions and its reactions.

FIG. 14 3D simulation (Video link of the 3D simulation: https://youtu.be/NUJvz_HUxgg)

CONCLUSION

Quadcopter are unmanned aerial vehicles that some delivery companies started using for delivering small packages. Even though there is precedent, it has only been done occasionally. The use of quadcopters can prove essential in special situations, helping bring food, drinks or medicine to people in isolation, but it is an overall new concept which must still requires research and testing before implementing it.

The PESTEL analysis, which is an assessment of the external environment's influence was done to evaluate the potential using drones as means of transportation on a large scale. This analysis consisted evaluation from a political, economic, socio-cultural, legal, technological and environmental point of view. Another aspect like, battery life, cost, safety of the package and weather conditions, were taken into account.

In order to analyse and understand how a quadcopter works in its environment, a digital model was created using MatLab software. Different collision avoidance solutions for avoiding an obstacle, collisions with aircrafts, flying close to the airports, prevention

of collisions with other traffic and collisions with other drones were identified. Using the trajectory tools, a well-defined trajectory is defined for a quadcopter in order to better represent its behaviour for a light parcel transport use. No fly zones are defined in order to restrict the quadcopter's flight path in some places.

The quadcopter is one of the simplest and most elegant designs for an unmanned aerial vehicle, one of the easiest to control, as shown in the simulation, and one of the less expensive to manufacture, given its simplicity. There are still regulations to be implemented and investments and technological progress to be made until the mass implementation of a delivery by drone system can be possible.

ACKNOWLEDGEMENTS

This paper represents an improved and extended version of the paper presented at the International Conference of Aerospace Sciences "AEROSPATIAL 2020", Bucharest, 15 - 16 October 2020, (Virtual Conference), Section 2 – Flight Mechanics, Paper S2.4.

This research was developed within the research partnership between [4]"POLITEHNICA" University of Bucharest, Faculty of Mechanical Engineering and Mechatronics and INCAS - National Institute for Aerospace Research "Elie Carafoli", through the EPS – European Project Semester programme.

The team of Science Advisors and Coordinators: Irina-Carmen ANDREI, Gina Florica STOICA, Nicoleta CRIȘAN, Delia PRISECARU, Cristian STOICA, Anca GRECULESCU.

The team of Tutors: Irina-Carmen ANDREI (INCAS Tutor), Nicoleta CRIŞAN (UPB Tutor).

We would also like to show our gratitude to Dr. Dragos-Daniel Ion-Guță, Head of Systems Division, and to all the research team members from INCAS, for supporting the EPS students groups and for providing expertise that greatly assisted the project research.

REFERENCES

[1] Wikipedia/ quadcopters;
[2] Dronezon.com;
[3] presse-citron.net;
[4] https://www.mathworks.com/help/aeroblks/quadcopter-project.html;
[5] https://ardupilot.org/copter/docs/advanced-multicopter-design.html;
[6] https://www.sdentertainer.com/news/what-happened-to-amazon-drone-delivery/;
[7] https://www.suasnews.com/2017/08/gaia-160-hybrid-5-hours-flight-time-2kg-payload/;
[8] https://www.wetalkuav.com/dji-phantom-4-wetsuit-rainproof-drone/;
[9] https://www.flirtey.com/;
[10] https://www.ups.com/us/en/services/knowledge-center/article.page?kid=art16deef03243;
[11] https://www.youtube.com/watch?v=0yMv16p8FO8;
[12] https://www.bpost.be/site/nl/pakjesautomaat/;
[13]T. Guardian, *How dangerous are drones to aircraft?*, 2018. [Online]. Available: https://www.theguardian.com/technology/2018/dec/20/how-dangerous-are-drones-to-aircraft;
[14]Wikipedia, *Regulation of unmanned aerial vehicles*, 2020. [Online]. Available: https://en.wikipedia.org/wiki/Regulation_of_unmanned_aerial_vehicles;
[15]F. Corrigan, *DJI Mavic Air 2 Review Of Features, Specs And FAQs Answered*, 2020. [Online]. Available: https://www.dronezon.com/drone-reviews/dji-mavic-air-2-review-includes-featuresspecs-faqs/;
[16]F. Corrigan, *12 Top Collision Avoidance Drones And Obstacle Detection Explained*, 2020. [Online]. Available: https://www.dronezon.com/learn-about-drones-quadcopters/top-droneswith-obstacle-detection-collision-avoidance-sensors-explained/.

PERFORMANCE ANALYSIS OF MILITARY FLYING WING UAV WITH PULSE JET ENGINE

Vasile PRISACARIU

"Henri Coandă" Air Force Academy, Brașov, Romania (prisacariu.vasile@afahc.ro)
ORCID: 0000-0003-4370-4756

DOI: 10.19062/1842-9238.2022.20.2.4

Abstract: *The current technological level of data acquisition systems, used on military and civilian unmanned aircraft, allow for diverse kinetic sampling conditions covering large ranges of altitudes and temperature. Thus, there is a need to collect the necessary atmospheric data, in terms of constructive simplicity and reduction of total costs (manufacturing and operation), with the help of unmanned aircraft equipped with PJE (pulse jet engine) and PDE (pulse detonation engine) propulsion systems. The article presents pre-design aspects of a flying wing UAV concept equipped with a PJE engine, which can be mounted on supersonic aircraft.*

Keywords: *flying wing, pulse jet engine, pulse detonation engine, XFLR5*

Symbols and acronyms

AR	*Aspect ratio*	*AoA*	*Angle of attack*
CAD	*Computer Aided Design*	*CAM*	*Computer Aided Manufacturing*
CFD	*Computational fluid dynamics*	*ISR*	*Intelligence, surveillance, and reconnaissance*
LLT	*Lifting line theory*	*MAC*	*Main aerodynamic chord*
PDE	*Pulse detonation engine*	*PJE*	*Pulse jet engine*
VLM	*Vortex Lattice Method*		
c_0	*Root chord*	c_e	*Tip chord*
c_l,	*Lift coefficient*	c_m	*Pitch coefficient*
c_d,	*Drag coefficient*		

1. INTRODUCTION

PDEs are propulsion systems, in experimental phases, that use supersonic detonation waves as a combustion mechanism, having a reduced mechanical complexity and high efficiency compared to traditional aerofoil engines, PDE being considered an extension of PJE [5].

Due to the thermodynamic conditions of combustion, it can be an eligible candidate for equipping UAVs for subsonic and supersonic kinetic conditions, under the conditions of a UAV concept optimized for atmospheric data acquisition missions at high altitudes.

PDE can be an eligible technical solution for the propulsion of UAVs with fixed wing in classic concept or tailless (flying wing) in airborne launch conditions. Starting from the Fi 103 (V1) missile, historical and evolutionary milestones have confirmed the usefulness of (military) UAVs, such as: AQM-34 Firebee (Fig. 1.1), Lockheed D-21 (Fig. 1.2), BQM-74), equipped with no rotor engine-PJE engines.

The PDE concept offers a number of advantages, the most relevant being: technological and design simplicity, record theoretical power per volume unit, they are ecological, low impact on the engine and aircraft structure.

However, the concept of PDEs does not offer commercial applications with technological limitations still to be solved, such as: ignition of the detonation wave in a controllable and reliable way, geometric optimization of the detonation tube, cycle repetition frequency, optimization of manufacturing materials, [5]. Along with technological progress, the PDE concept is analysed multidisciplinary by the scientific community, a concept subject to concerns in the field of experimental thermodynamics and CFD analyses, [4].

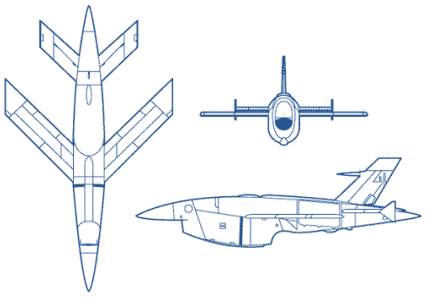

FIG. 1.1 AQM-34 Firebee, [1]

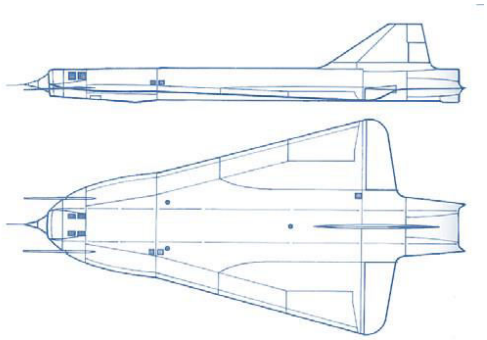

FIG. 1.2 Lockheed D 21, [2]

According to specialist information [8, 9] a PDE engine was used on modified Scaled Composites-EZ (Fig. 1.3) thus demonstrating the efficiency of using such a propulsion system in terms of fuel consumption versus traction characteristics and of the level of atmospheric pollution. PJE engines are used in UAS and general and sport aviation, [10, 11].

FIG 1.3 Rutan Long-EZ Borealis cu PDE, [8, 9]

FIG 1.4 Glider PJE, [10]

2.AERODYNAMIC PERFORMANCE EVALUATION TOOLS AND METHODS

2.1. XFLR5 software

XFLR5 provides a series of useful modules for geometric parameterization and aerodynamic performance evaluation (2D and 3D) for aircraft without the influence and interference generated by propulsion systems (propellers). For XFLR5 6.55, the modules are as follows: direct foil design (geometric parameterization of aerofoils), Xfoil inverse design (generation of profiles from selected/edited aerofoils), Xdirect analysis (analysis of aerofoil performances), wing and plane design (geometric parameterization) and 3D aerodynamic analysis single geometries/complex geometries).

For 3D aerodynamic analysis the software tool can use a number of methods such as: LLT (lifting line theory), VLM (vortex lattice method) and 3D panels. The results

of the analyses are graphic, numerical with possibilities of poor processing and use with other software tools (e.g. CAD/CAM software, Excel), [7, 13].

2.2. Aerodynamic analysis methods

a. The VLM method

VLM (Vortex Latice Method) is an extension of the LLT (lifting line theory) method, based on the theory of ideal flow (potential flow), used both in the pre-design stages of aircraft (for a quick estimation of global aerodynamic characteristics) and in the field aerospace university and provides a reasonable level of accuracy. Through the initial estimates of the pressure distribution on the wing, the structural design phases of the fixed (wing, wings) and mobile (flaps, ailerons, thruster) bearing surfaces can be initiated, see Fig. 2.1.

VLM models fixed aerofoil surfaces (wing, tailplanes) as a thin web of discrete vortices for the calculation of lift and induced drag without the influence of wing thickness, turbulence, boundary layer and air viscosity. However, the method offers a global approach to the distribution of the pressure coefficient that determines the quantification of the relevant aerodynamic coefficients (and derived quantities) for possible evaluations of the stability/manoeuvrability qualities for the conceptual phase of the aircraft, [17, 18].

The method is described clearly and in detail in a series of specialized references in the field of aerodynamics, the most relevant being: Katz-Plotkin [19], Anderson [20], Bertin-Simth [21] or Drela [22].

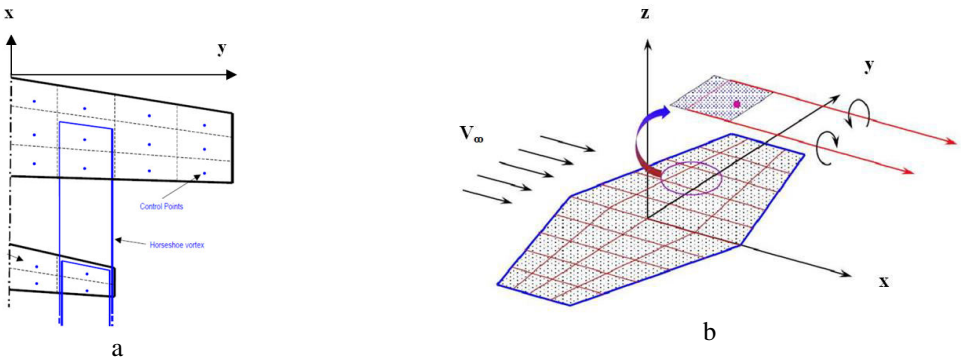

FIG 2.1 VLM method a.[18], b.[23]

b. The 3D panel method

This method analyses the distribution of the pressure coefficient (intrados/extrados) of a bearing surface also considering the thickness of the wing (3D geometry) compared to the VLM which was based only on the curvature line of the wing (2D geometry), see Fig. 2.2.

3D panel models the perturbation existing on the wing surface, initially being an analysis method with singularities (source distributions and vortices) later being a variant of boundary element methods. Currently this method can be used for a solution of the flow potential equation on complex geometries for subsonic or supersonic speeds, the method eliminating the need for a volumetric grid as in the case of finite element methods, [18].

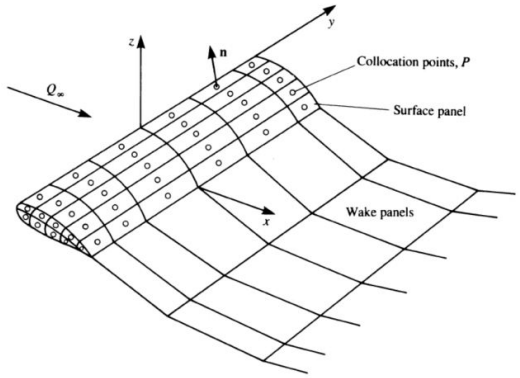

FIG 2.2 3D panel method, geometry approximation by panel elements [19]

3.CONCEPT FLYING WING UAV-PJE

The UAV-PJE concept is realized with the software tool XFLR5 [6, 7] based on a flying wing geometry (see Fig. 2.1) that can be used in ISR missions, powered by a miniPJE engine, having the characteristics estimated in Table 2.1.

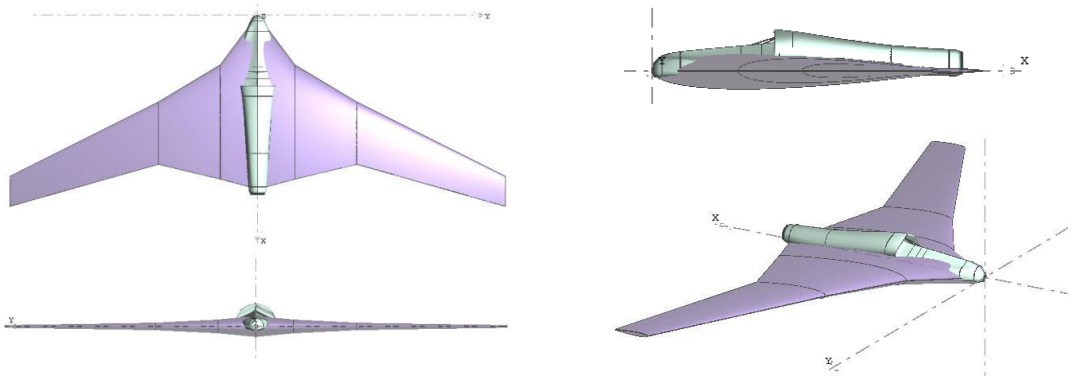

FIG. 2.1 UAV-PJE/PDE initial proposal concept

Table 2.1 Initial estimated characteristics for FW UAV-PJE

Characteristics	Value	Characteristics	Value
Span / Length	2 / 1,5 m	MAC	0,35 m
Dihedral / Swept	5^o / $26,79^o$	Wing load	8,1 kg/m^2
Surface	0,574 m^2	Total weight/ Payload	4,65 kg / 1,25 kg
Aspect ratio / taper ratio	6,97 / 0,171	Propulsion	PJE / pulse-jet

The estimation of the mass and balance variant is highlighted graphically in Fig. 2.2 and numerically in Table 2.2 and annex 3.

Table 2.2 FW UAV-PJE weight and balance

Element	Value	Element	Value
Frame weight	2,2 kg	Fuel	0,5 kg
Engine weight	1,2 kg	Battery	0,25 kg
Electronic equipment weight	0,5	Total weight	4,65 kg

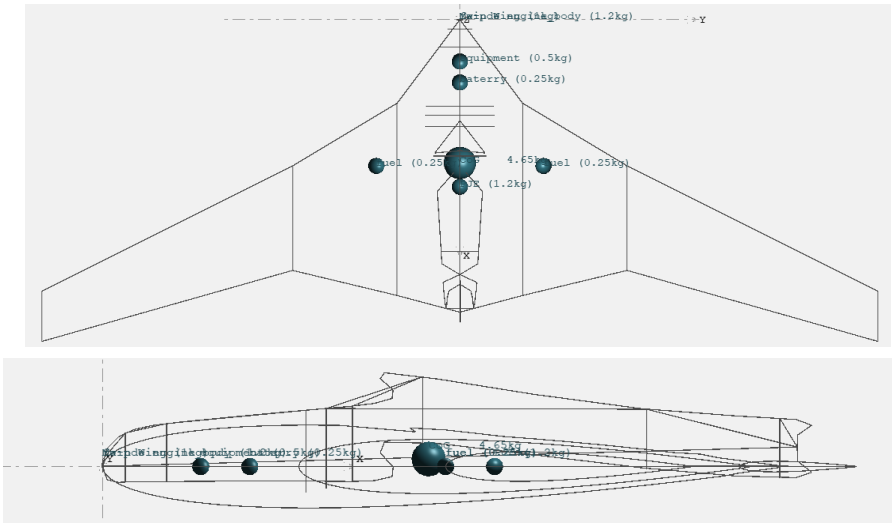

FIG. 2.2 UAV-PJE weight and balance for initial proposal concept

To make a 3D model, XFLR5 can export *.stl files used for 3D printing with the Cura 15 tool, see Fig. 2.3, [15]. The 3D model can be used to measure aerodynamic parameters in subsonic wind tunnels, [16].

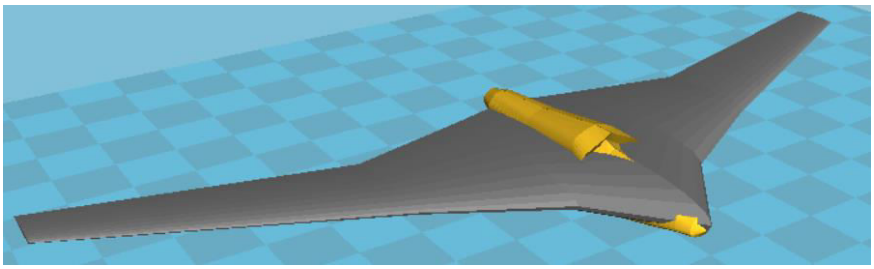

FIG. 2.3 Model *.stl for 3D print, [15]

4.UAV-PJE PERFORMANCES ANALYSIS

4.1. Simulation conditions and analysis cases

For optimal parametrisation from the point of view of the useful space of the wing, a high-thickness profile specific to the MH 92 flying wings was chosen for the fitting, and for the extreme section the MH 64 was selected, thus generating a mixed geometric torsion, both designed by Martin Hepperle, see Fig. 3.1, having the characteristics in Table 3.1, [12].

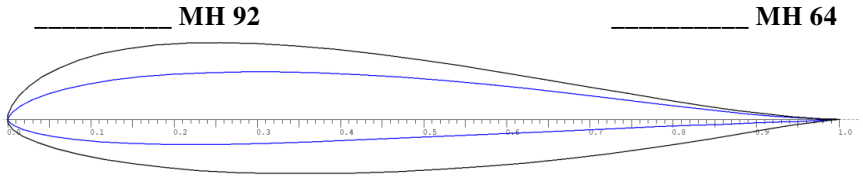

FIG. 3.1 Aerofoils [13]

Table 3.1 Aerofoil features

MH 92		MH 64	
Max. thickness	15,50% la 27,5%	Max. thickness	8,6% la 26,9%
Max. curvature	1,4% la 15%	Max. curvature	1,4% la 41,8%

4.2. Performance analysis for 2D geometry (XFLR5)

The simulation steps aim at an estimation of the aerodynamic performance of the proposed geometric configuration (see Table 2.1). according to the analysis conditions recorded in Table 3.2.

Table 3.2 2D analysis conditions

Analysis condition	Value	Analysis condition	Value
Chord	1m	Speed	15 m/s
Nr. Reynolds	1100000	Air density	1,225 kg/m^3
Iterations	100	Aer viscosity	1,5 x 10^{-5} m^2/s

The analysed aerofoils provide the variation of comparative values over the range of AoA analysed to observe the aerodynamic behaviour at a minimum theoretical speed (15 m/s).

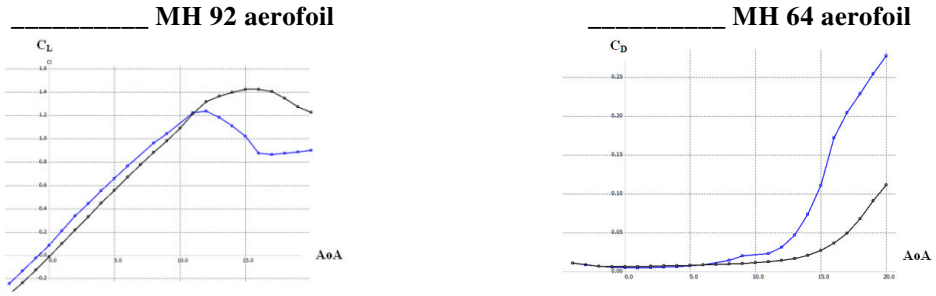

a b

FIG. 3.2 Airfoil polars, a.c_l vs AoA, b.c_d vs AoA, [13]

Fig. 3.2 and 3.3 show both the polars of the relevant aerodynamic coefficients c_l, c_d and c_m as a function of AoA, as well as the gliding rate c_l/c_d vs AoA at the analysed speed (Fig. 3.2c) or the mutual variations of c_l vs c_d (Fig. 3.2.d).

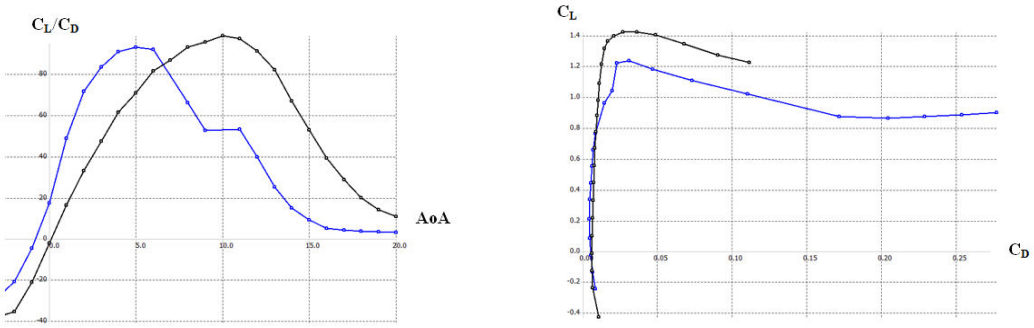

a b

FIG. 3.3 Aerofoil polars, c. c_l/c_d vs AoA, d.c_l vs c_d [13]

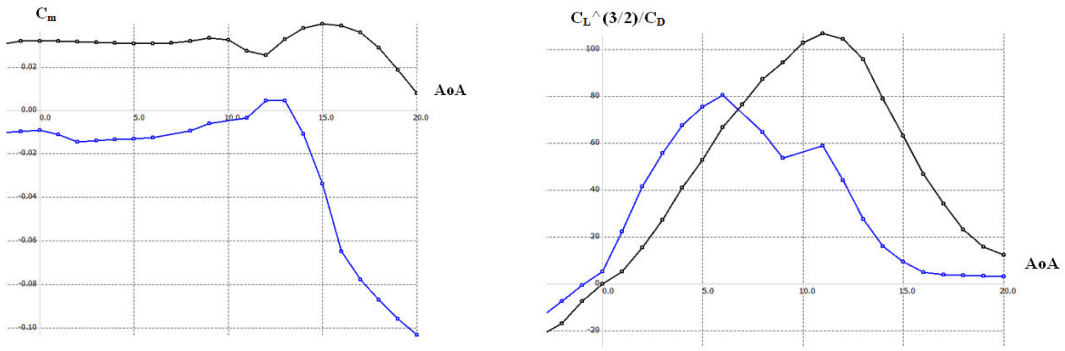

a b

FIG. 3.4 Aerofoil polars, a.c_m vs AoA, b. $(c_l/c_d)^{3/2}$ vs AoA [13]

The differences in the values of the aerodynamic coefficients for the two analysed aerofoils recommend their use in the span: MH 92 at the embedment and MH 64 at the tip of the wing. The pitching moment differences (Fig. 3.4.a) recommend an optimization of the overall performance through aerodynamic torsion (see also annex 1).

4.3. 3D geometry performance analysis

It is focused on a series of aerodynamic analyses for the single flying wing without the presence and influence of the fuselage in the form of aerodynamic interferences, having the atmospheric and kinetic analysis conditions from Table 3.3.

Table 3.3 3D analysis conditions

Analysis condition	Value	Analysis condition	Value
Span	2 m	Speed	15 m/s
Surface	0,57 m^2	Boundary conditions	Dirichlet
AoA	$-15^o \div 15^o$	AoA precision	0,01
Method of analysis	VLM/3D panel	Panels VLM / 3D	494 / 1014

The analysed 3D geometry (see also Table 2.1) provides a series of aerodynamic parameter values, highlighted in Fig. 3.5 and 3.6 and Annex 2.

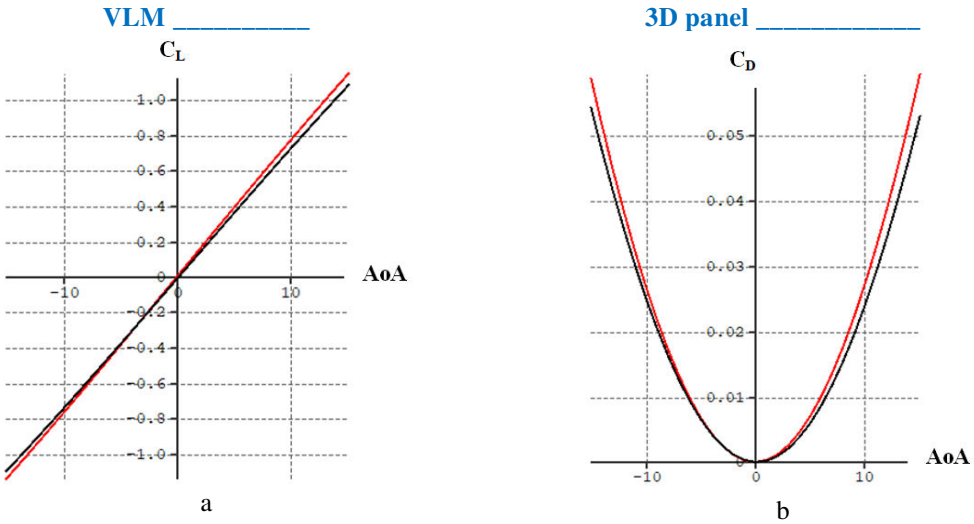

a b

FIG. 3.5 UAV-PJE flying wing polars, a.Cl-AoA, b.Cd-AoA [13]

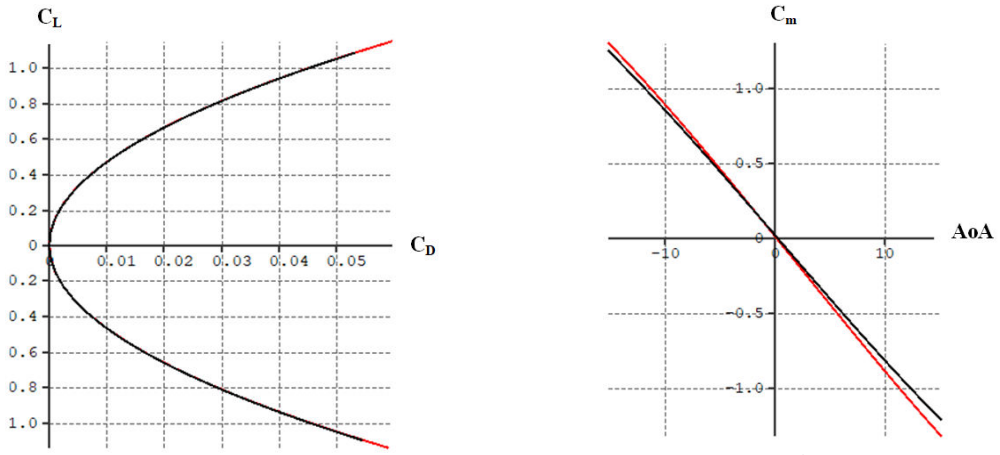

c d

FIG. 3.6 UAV-PJE flying wing polars, c.C_l-C_d, d.C_m-AoA [13]

According to Fig. 3.5 and 3.6 differences in the values of the aerodynamic coefficients are observed with the increase of AoA due to the consideration of the friction effect in the case of the 3D panel method.

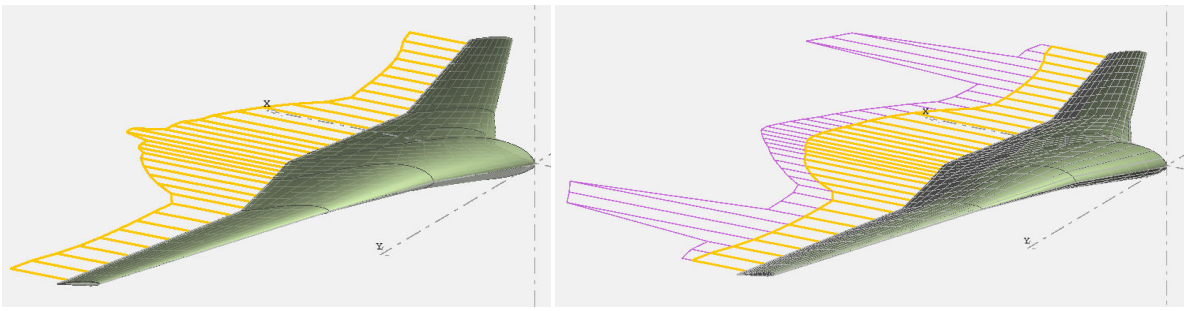

a b

FIG. 3.7 Drag force (AoA=9°), a.VLM method, b. 3D panel method

In Fig. 3.7, we have the comparative values of the drag for a critical value AoA=9°, and can be observed the trace of the drag generated by the air viscosity. In Fig. 3.8 the values of the pressure coefficient Cp extracted with the two analysis methods: VLM and 2D panel are observed, generated value differences generated by the consideration of air viscosity.

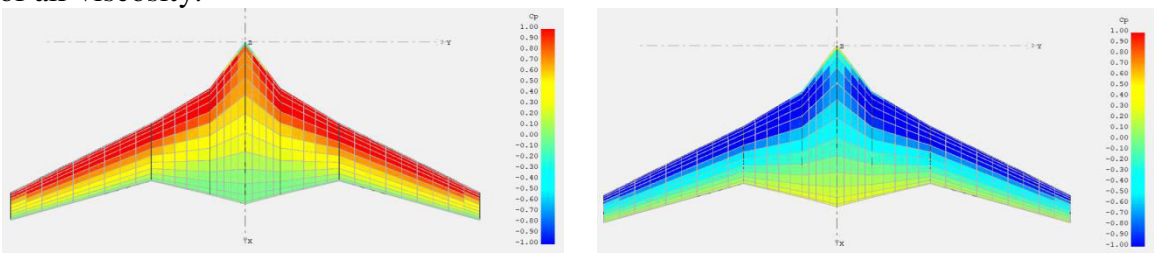

a b

FIG. 3.8 Pressure coefficient distribution C_p (AoA=9°), a.VLM method, b. 3D panel method

5. PROPULSION SYSTEM (PJE) PERFORMANCE ESTIMATE

A mass-optimized PJE for the analysed UAV (maximum weight of 4.65 kg) has the dimensions estimated from Table 5.1, values obtained with Pulse Jet Engine Calculator 1.4 [24]. Figure 5.1. shows a simple PJE geometry with the main dimensions calculated.

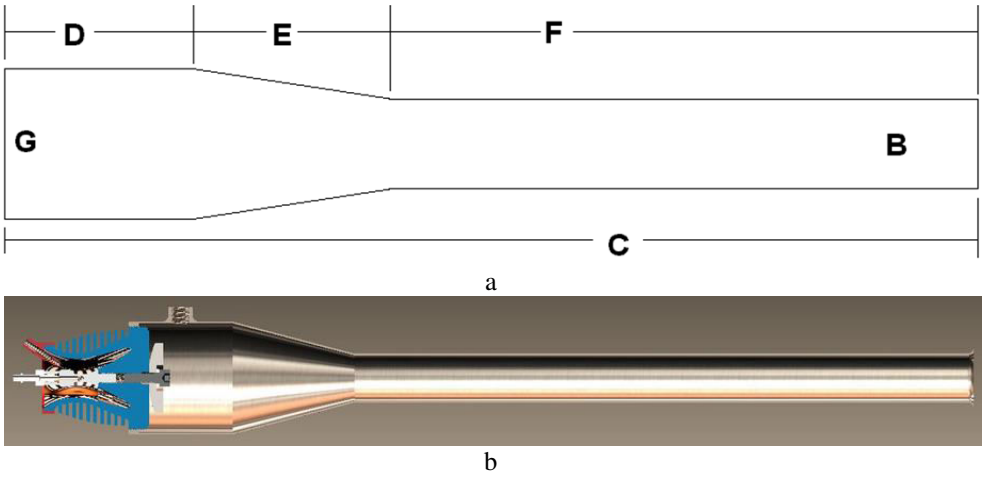

a

b

FIG. 5.1 Pulse jet engine a.geometry a.[24], b. CAD aspects,[25]

Table 5.1 PJE structural features and performances estimated

Features	Value	Features	Value
Lenght C	68 cm	Valve head lenght	10.21 cm
Lenght combustor D	13,62 cm	Exhaust cone E	13,62
Exhaust pipe F	40,86	Detonation freguency	189-203 Hz
Exhaust B	4,75 cm	Thrust	5kg/cm

CONCLUSIONS

Currently, PJE-powered unmanned aircraft are a mature technology that can offer advantages to users in areas of interest, technology that is also refined with the help of analysis software tools.

The article summarized a pre-design stage of a PJE powered flying wing UAV using freeware tools (XFLR5, PJE calculator).

The current study can be substantiated with the help of CFD tools that can provide high degrees of confidence both in problematic kinetic cases (transonic speeds) and in manoeuvrings flight situations (high angles of attack, high bank angles). In the future, it is considered that the CFD instrumentation will be applied to virtual and real geometric models for a comparative approach to the results and the choice of optimized technical solutions.

REFERENCES

[1] Freebee UAV, https://www.globalsecurity.org/intell/systems/firebee.htm, accesed in 21.09.2022;

[2] Colville, Jesse & Lewis, Mark & Starkey, Ryan. (2006). *Axisymmetric Inlet Design for Combined-Cycle Engines. Journal of Propulsion and Power* - J PROPUL POWER. 22. 1049-1058. 10.2514/1.18063;

[3] V. Prisacariu, *The history and the evolution of UAVs from the beginning till the 70s*, Journal of Defense Resources Management, vol.8 issue 1(14)/2017, ISSN:2068-9403, eISSN:2247-6466, ISSN-L: 2247-6466, p181-189;

[4] S. Cassady, *Pulse detonation engine*, 2006, available at http://large.stanford.edu/courses/2016/ph240/cassady1/ , accessed on 12.11.2022;
[5] S.L. Deshmukh, *Pulse detonation engine – future of aerospace propulsion*, 2021, available https://dras.in/pulse-detonation-engines-future-of-aerospace-propulsion, accessed on 18.12.2022;
[6] M. Drela, H. Yungren, *Guidelines for XFLR5 v6.03 (Analysis of foils and wings operating at low Reynolds numbers),* 2011, available at http://sourceforge.net/projects/xflr5/files;
[7] V. Prisacariu, *Analysis of UAVs flight characteristics*, vol. 38, nr. 3/2018, p.29-36, Review of the Air Force Academy, ISSN 1842-9238; e-ISSN 2069-4733, DOI: 10.19062/1842-9238.2018.16.3.4;
[8] S.J. Ajitesh, T. Mahant, *Pulse detonation engine - a review*, International Research Journal of Modernization in Engineering Technology and Science, Vol.4, issue 05, 2022, e-ISSN: 2582-5208;
[9] L. Barr, *Puse detonation engine flies into history*, 2008, available at https://www.af.mil/News/Article-Display/Article/123534/pulsed-detonation-engine-flies-into-history, accesed in 18.01.2023;
[10] https://wave-engine.com/technology, accesed in 21.02.2023;
[11] https://www.airtoi.com/pulse.htm, accesed in 14.02.2023;
[12] M. Hepperle, https://www.mh-aerotools.de/airfoils/mh64koo.htm, accesed in 16.02.2022;
[13] XFLR%, https://www.xflr5.tech/xflr5.htm, accesed in 16.02.2022;
[14] M. Hepperle, https://www.mh-aerotools.de/airfoils/mh92koo.htm, 16.02.2022;
[15] Ultimaker, *Cura 13 user manual*, v.10, 41p., available at https://docs.rs-online.com/a10b/0900766b81376d80.pdf;
[16] *Tunel de vânt Sangari SES 115*, disponibil la https://sangari.ro/index.php/ses115, accesat la data de 15.05.2022;
[17] NASA, *Vortex-lattice utilization*. NASA SP-405, NASA-Langley, Washington, 1976;
[18] *XFLR5 Analysis of foils and wings operating at low Reynolds numbers*, Guidelines for QFLR5 v0.03, 2009, available at https://engineering.purdue.edu/~aerodyn/AAE333/FALL10/HOMEWORKS/HW13/XFLR5_v6.01_Beta_Win32%282%29/Release/Guidelines.pdf;
[19] J. Katz and A. Plotkin, *Low-Speed Aerodynamics From Wing Theory to Panel Methods*, McGraw-Hill, Inc., New York, 1991;
[20] J.D. Anderson Jr, *Fundamentals of aerodynamics*, 2nd ed., McGraw-Hill Inc, 1991;
[21] J.J. Bertin, M.L. Smith, *Aerodynamics for Engineers*, 3rd ed., Prentice Hall, New Jersey, 1998;
[22] M. Drela, *Flight Vehicle Aerodynamics, MIT Press*, Cambridge, MA, 2014;
[23] Huang, Wei & Li, Binbin & Liang, Hui & Chen, Xiaobo. (2016). *Dynamic course stability of towing systems using fiber ropes*, Marine Operations Specialty Symposium (MOSS 2016) , ISBN: 978-981-11-0743-6, doi:10.3850/978-981-11-0743-6 MOSS1015;
[24] E. Beck, Eric Beck's Pulsejet Calculator Version 1.4, available at https://www.jetzilla.com/jetZilla.html;
[25] Kovesdi L., *Pulse jet PL-25*, 2014, available at https://grabcad.com/library/pulse-jet-engine-pl-35-

Anexx 1. 2D data export

xflr5 v6.55

Calculated polar for: MH64 © Martin Hepperle

1 1 Reynolds number fixed Mach number fixed

xtrf = 1.000 (top) 1.000 (bottom)
Mach = 0.044 Re = 1.100 e 6 Ncrit = 9.000

alpha	CL	CD	CDp	Cm	Top Xtr	Bot Xtr	Cpmin	Chinge	XCp		
-7.000	-0.6218	0.03382	0.03139	-0.0212	0.9526	0.0090	-4.1838	0.0000	0.0000	0.0000	0.2118
-6.000	-0.5487	0.02674	0.02354	-0.0187	0.8810	0.0118	-3.3770	0.0000	0.0000	0.0000	0.2123
-5.000	-0.4446	0.02540	0.02174	-0.0170	0.8384	0.0182	-2.4238	0.0000	0.0000	0.0000	0.2087
-3.000	-0.2430	0.00847	0.00268	-0.0113	0.7659	0.0118	-1.9976	0.0000	0.0000	0.0000	0.2008
-2.000	-0.1341	0.00647	0.00113	-0.0102	0.7311	0.2117	-1.3695	0.0000	0.0000	0.0000	0.1710
-1.000	-0.0250	0.00539	0.00088	-0.0098	0.6967	0.4759	-0.4855	0.0000	0.0000	0.0000	-0.1481
0.000	0.0844	0.00481	0.00072	-0.0091	0.6512	0.6780	-0.4154	0.0000	0.0000	0.0000	0.3564
1.000	0.2092	0.00429	0.00077	-0.0112	0.5831	0.9778	-0.5479	0.0000	0.0000	0.0000	0.3017
2.000	0.3369	0.00472	0.00084	-0.0147	0.4934	1.0000	-0.7241	0.0000	0.0000	0.0000	0.2914
3.000	0.4450	0.00534	0.00111	-0.0140	0.3959	1.0000	-0.9345	0.0000	0.0000	0.0000	0.2787
4.000	0.5529	0.00609	0.00152	-0.0135	0.3038	1.0000	-1.2262	0.0000	0.0000	0.0000	0.2710
5.000	0.6600	0.00711	0.00213	-0.0130	0.2057	1.0000	-2.0487	0.0000	0.0000	0.0000	0.2657
6.000	0.7660	0.00835	0.00301	-0.0126	0.1190	1.0000	-3.1175	0.0000	0.0000	0.0000	0.2615
8.000	0.9601	0.01457	0.00941	-0.0092	0.0083	1.0000	-5.0423	0.0000	0.0000	0.0000	0.2525
9.000	1.0400	0.02001	0.01543	-0.0058	0.0069	1.0000	-6.2572	0.0000	0.0000	0.0000	0.2473
10.000	1.1297	0.02195	0.01763	-0.0046	0.0050	1.0000	-8.2534	0.0000	0.0000	0.0000	0.2445
11.000	1.2202	0.02312	0.01887	-0.0034	0.0032	1.0000	-10.4633	0.0000	0.0000	0.0000	0.2417
12.000	1.2263	0.03184	0.02838	0.0048	0.0022	1.0000	-10.9410	0.0000	0.0000	0.0000	0.2336
13.000	1.1720	0.04812	0.04547	0.0039	0.0022	1.0000	-10.7108	0.0000	0.0000	0.0000	0.2326
14.000	1.0972	0.07533	0.07332	-0.0122	0.0022	1.0000	-10.0683	0.0000	0.0000	0.0000	0.2454
15.000	1.0107	0.11272	0.11115	-0.0350	0.0024	1.0000	-8.8762	0.0000	0.0000	0.0000	0.2680

xflr5 v6.55

Calculated polar for: MH92 © Martin Hepperle

1 1 Reynolds number fixed Mach number fixed

xtrf = 1.000 (top) 1.000 (bottom)
Mach = 0.044 Re = 1.100 e 6 Ncrit = 9.000

alpha	CL	CD	CDp	Cm	Top Xtr	Bot Xtr	Cpmin	Chinge	XCp		
-14.000	-0.5713	0.15597	0.15438	0.0374	1.0000	0.0181	-1.8024	0.0000	0.0000	0.0000	0.2984
-13.000	-0.5590	0.13769	0.13613	0.0282	1.0000	0.0181	-1.9795	0.0000	0.0000	0.0000	0.2840
-12.000	-0.5709	0.11241	0.11088	0.0156	1.0000	0.0180	-2.3847	0.0000	0.0000	0.0000	0.2617
-11.000	-0.9953	0.03217	0.02846	-0.0083	1.0000	0.0098	-6.2514	0.0000	0.0000	0.0000	0.2289
-9.000	-0.9134	0.01788	0.01236	0.0111	0.8228	0.0068	-5.4607	0.0000	0.0000	0.0000	0.2516
-8.000	-0.8524	0.01328	0.00706	0.0198	0.7689	0.0120	-4.9014	0.0000	0.0000	0.0000	0.2636
-7.000	-0.7477	0.01264	0.00641	0.0213	0.7209	0.0158	-3.8884	0.0000	0.0000	0.0000	0.2697
-4.000	-0.4261	0.01055	0.00391	0.0247	0.5863	0.0197	-1.8045	0.0000	0.0000	0.0000	0.3011
-2.000	-0.2339	0.00663	0.00161	0.0304	0.4939	0.5185	-1.0432	0.0000	0.0000	0.0000	0.3741
-1.000	-0.1267	0.00604	0.00145	0.0317	0.4580	0.6797	-0.6171	0.0000	0.0000	0.0000	0.4955
0.000	-0.0129	0.00603	0.00146	0.0319	0.4190	0.7463	-0.7453	0.0000	0.0000	0.0000	2.7257
1.000	0.1018	0.00620	0.00160	0.0318	0.3821	0.7959	-0.8780	0.0000	0.0000	0.0000	-0.0723
2.000	0.2170	0.00653	0.00178	0.0315	0.3422	0.8242	-1.0323	0.0000	0.0000	0.0000	0.0964
3.000	0.3314	0.00698	0.00207	0.0312	0.3071	0.8461	-1.1945	0.0000	0.0000	0.0000	0.1473
4.000	0.4454	0.00726	0.00242	0.0310	0.2901	0.8713	-1.3616	0.0000	0.0000	0.0000	0.1714
5.000	0.5575	0.00789	0.00287	0.0307	0.2562	0.8851	-1.5517	0.0000	0.0000	0.0000	0.1852
6.000	0.6696	0.00822	0.00326	0.0306	0.2444	0.9051	-1.7558	0.0000	0.0000	0.0000	0.1938
7.000	0.7765	0.00896	0.00397	0.0311	0.2153	0.9234	-2.0012	0.0000	0.0000	0.0000	0.1985
8.000	0.8819	0.00949	0.00453	0.0319	0.2017	0.9415	-2.2928	0.0000	0.0000	0.0000	0.2012
9.000	0.9820	0.01031	0.00531	0.0333	0.1772	0.9609	-2.5862	0.0000	0.0000	0.0000	0.2023
10.000	1.0914	0.01110	0.00621	0.0324	0.1650	0.9789	-2.9549	0.0000	0.0000	0.0000	0.2051
11.000	1.2154	0.01256	0.00753	0.0274	0.1323	0.9910	-3.3795	0.0000	0.0000	0.0000	0.2109
12.000	1.3158	0.01452	0.00931	0.0257	0.1010	1.0000	-3.8266	0.0000	0.0000	0.0000	0.2122
13.000	1.3636	0.01672	0.01147	0.0330	0.0810	1.0000	-4.2314	0.0000	0.0000	0.0000	0.2058
14.000	1.3933	0.02100	0.01579	0.0380	0.0616	1.0000	-4.7089	0.0000	0.0000	0.0000	0.2007
15.000	1.4186	0.02707	0.02198	0.0397	0.0526	1.0000	-5.2094	0.0000	0.0000	0.0000	0.1977

Anexx 2. 3D data export

xflr5 v6.55

Plane name : fw-pde engine
Polar name : T1-15.0 m/s-VLM1
Freestream speed : 15.000 m/s

alpha	Beta	CL	CDi	CDv	CD	CY	Cl	Cm	Cn	Cni	QInf	XCP
-15.000	0.000	-1.063660	0.051984	0.000000	0.051984	-0.000000	-0.000000	1.205421	-0.000000	-0.000000	15.0000	0.4302
-14.000	0.000	-0.994501	0.045562	0.000000	0.045562	-0.000000	0.000000	1.130646	0.000000	0.000000	15.0000	0.4296
-13.000	0.000	-0.924699	0.039496	0.000000	0.039496	-0.000000	0.000000	1.054463	-0.000000	-0.000000	15.0000	0.4290
-12.000	0.000	-0.854296	0.033807	0.000000	0.033807	-0.000000	0.000000	0.976965	-0.000000	-0.000000	15.0000	0.4285
-11.000	0.000	-0.783334	0.028511	0.000000	0.028511	-0.000000	-0.000000	0.898246	0.000000	0.000000	15.0000	0.4281
-10.000	0.000	-0.711856	0.023627	0.000000	0.023627	-0.000000	-0.000000	0.818402	-0.000000	-0.000000	15.0000	0.4278
-9.000	0.000	-0.639907	0.019169	0.000000	0.019169	-0.000000	0.000000	0.737531	-0.000000	-0.000000	15.0000	0.4276
-8.000	0.000	-0.567531	0.015152	0.000000	0.015152	-0.000000	0.000000	0.655730	0.000000	0.000000	15.0000	0.4275
-7.000	0.000	-0.494773	0.011587	0.000000	0.011587	-0.000000	0.000000	0.573100	-0.000000	-0.000000	15.0000	0.4275
-6.000	0.000	-0.421681	0.008487	0.000000	0.008487	-0.000000	0.000000	0.489742	0.000000	0.000000	15.0000	0.4277
-5.000	0.000	-0.348301	0.005862	0.000000	0.005862	-0.000000	0.000000	0.405756	-0.000000	-0.000000	15.0000	0.4283
-4.000	0.000	-0.274682	0.003719	0.000000	0.003719	-0.000000	0.000000	0.321245	-0.000000	-0.000000	15.0000	0.4293
-3.000	0.000	-0.200870	0.002066	0.000000	0.002066	-0.000000	0.000000	0.236312	-0.000000	-0.000000	15.0000	0.4314
-2.000	0.000	-0.126914	0.000909	0.000000	0.000909	-0.000000	0.000000	0.151061	-0.000000	-0.000000	15.0000	0.4360
-1.000	0.000	-0.052863	0.000251	0.000000	0.000251	0.000000	0.000000	0.065596	-0.000000	-0.000000	15.0000	0.4543
0.000	0.000	0.021234	0.000095	0.000000	0.000095	0.000000	0.000000	-0.019980	0.000000	0.000000	15.0000	0.3445
1.000	0.000	0.095329	0.000442	0.000000	0.000442	0.000000	0.000000	-0.105563	0.000000	0.000000	15.0000	0.4054
2.000	0.000	0.169373	0.001291	0.000000	0.001291	-0.000000	0.000000	-0.191047	0.000000	0.000000	15.0000	0.4131
3.000	0.000	0.243316	0.002640	0.000000	0.002640	0.000000	0.000000	-0.276329	0.000000	0.000000	15.0000	0.4162
4.000	0.000	0.317111	0.004486	0.000000	0.004486	-0.000000	0.000000	-0.361304	0.000000	0.000000	15.0000	0.4179
5.000	0.000	0.390708	0.006823	0.000000	0.006823	-0.000000	0.000000	-0.445870	0.000000	0.000000	15.0000	0.4191
6.000	0.000	0.464060	0.009644	0.000000	0.009644	-0.000000	0.000000	-0.529924	0.000000	0.000000	15.0000	0.4200
7.000	0.000	0.537119	0.012943	0.000000	0.012943	-0.000000	0.000000	-0.613362	0.000000	0.000000	15.0000	0.4208
8.000	0.000	0.609838	0.016708	0.000000	0.016708	-0.000000	0.000000	-0.696083	0.000000	0.000000	15.0000	0.4216
9.000	0.000	0.682170	0.020929	0.000000	0.020929	-0.000000	0.000000	-0.777987	0.000000	0.000000	15.0000	0.4223
10.000	0.000	0.754070	0.025593	0.000000	0.025593	-0.000000	0.000000	-0.858974	0.000000	0.000000	15.0000	0.4229
11.000	0.000	0.825492	0.030688	0.000000	0.030688	-0.000000	0.000000	-0.938944	0.000000	0.000000	15.0000	0.4236
12.000	0.000	0.896392	0.036197	0.000000	0.036197	-0.000000	0.000000	-1.017801	0.000000	0.000000	15.0000	0.4244
13.000	0.000	0.966727	0.042104	0.000000	0.042104	-0.000000	0.000000	-1.095449	0.000000	0.000000	15.0000	0.4251
14.000	0.000	1.036454	0.048391	0.000000	0.048391	-0.000000	0.000000	-1.171792	0.000000	0.000000	15.0000	0.4259
15.000	0.000	1.105531	0.055040	0.000000	0.055040	-0.000000	0.000000	-1.246739	0.000000	0.000000	15.0000	0.4267

xflr5 v6.55

Plane name : fw-pde engine
Polar name : T1-15.0 m/s-Panel
Freestream speed : 15.000 m/s

alpha	Beta	CL	CDi	CDv	CD	CY	Cl	Cm	Cn	Cni	QInf	XCP
-15.000	0.000	-1.086837	0.054767	0.095650	0.150418	0.000000	0.000000	1.271639	-0.000000	-0.000000	15.0000	0.4273
-14.000	0.000	-1.015381	0.047916	0.095650	0.143567	0.000000	0.000000	1.193181	-0.000000	-0.000000	15.0000	0.4282
-13.000	0.000	-0.943261	0.041455	0.084788	0.126243	0.000000	0.000000	1.111920	-0.000000	-0.000000	15.0000	0.4291
-12.000	0.000	-0.870520	0.035403	0.074675	0.110078	0.000000	0.000000	1.029252	-0.000000	-0.000000	15.0000	0.4300
-11.000	0.000	-0.797202	0.029779	0.065312	0.095092	0.000000	0.000000	0.945320	-0.000000	-0.000000	15.0000	0.4311
-10.000	0.000	-0.723354	0.024601	0.056547	0.081148	0.000000	0.000000	0.860237	-0.000000	-0.000000	15.0000	0.4322
-9.000	0.000	-0.649022	0.019885	0.047991	0.067876	0.000000	0.000000	0.774069	-0.000000	-0.000000	15.0000	0.4334
-8.000	0.000	-0.574254	0.015645	0.030269	0.045914	0.000000	0.000000	0.685807	-0.000000	-0.000000	15.0000	0.4348
-7.000	0.000	-0.499098	0.011894	0.021361	0.033255	0.000000	0.000000	0.597887	0.000000	-0.000000	15.0000	0.4364
-6.000	0.000	-0.423602	0.008645	0.017839	0.026484	0.000000	0.000000	0.509918	0.000000	-0.000000	15.0000	0.4385
-5.000	0.000	-0.347818	0.005906	0.014921	0.020827	0.000000	0.000000	0.421373	0.000000	-0.000000	15.0000	0.4412
-4.000	0.000	-0.271794	0.003687	0.010524	0.014211	0.000000	0.000000	0.332126	0.000000	-0.000000	15.0000	0.4452
-3.000	0.000	-0.195582	0.001995	0.007342	0.009337	-0.000000	-0.000000	0.242582	0.000000	-0.000000	15.0000	0.4520
-2.000	0.000	-0.119232	0.000834	0.006408	0.007242	-0.000000	-0.000000	0.152820	0.000000	-0.000000	15.0000	0.4668
-1.000	0.000	-0.042797	0.000209	0.005932	0.006141	-0.000000	-0.000000	0.062753	-0.000000	-0.000000	15.0000	0.5330
0.000	0.000	0.033674	0.000121	0.005667	0.005789	-0.000000	-0.000000	-0.027537	-0.000000	0.000000	15.0000	0.3003
1.000	0.000	0.110128	0.000572	0.005493	0.006065	0.000000	-0.000000	-0.117954	-0.000000	0.000000	15.0000	0.3913
2.000	0.000	0.186514	0.001560	0.005486	0.007046	0.000000	-0.000000	-0.208396	-0.000000	-0.000000	15.0000	0.4080
3.000	0.000	0.262781	0.003081	0.005715	0.008796	0.000000	-0.000000	-0.298768	-0.000000	-0.000000	15.0000	0.4152
4.000	0.000	0.338877	0.005132	0.006061	0.011193	0.000000	-0.000000	-0.388967	-0.000000	-0.000000	15.0000	0.4192
5.000	0.000	0.414752	0.007706	0.006467	0.014174	0.000000	-0.000000	-0.478883	-0.000000	-0.000000	15.0000	0.4219
6.000	0.000	0.490356	0.010797	0.006964	0.017761	0.000000	-0.000000	-0.568416	-0.000000	-0.000000	15.0000	0.4239
7.000	0.000	0.565637	0.014393	0.007542	0.021936	0.000000	-0.000000	-0.657462	-0.000000	-0.000000	15.0000	0.4254
8.000	0.000	0.640548	0.018486	0.008539	0.027025	0.000000	-0.000000	-0.745984	-0.000000	-0.000000	15.0000	0.4265
9.000	0.000	0.715038	0.023062	0.009905	0.032966	0.000000	-0.000000	-0.833892	-0.000000	-0.000000	15.0000	0.4275
10.000	0.000	0.789061	0.028107	0.024201	0.052308	0.000000	-0.000000	-0.924345	-0.000000	-0.000000	15.0000	0.4283
11.000	0.000	0.862569	0.033606	0.047003	0.080609	0.000000	-0.000000	-1.016548	-0.000000	-0.000000	15.0000	0.4290
12.000	0.000	0.935516	0.039544	0.051560	0.091104	0.000000	-0.000000	-1.103289	0.000000	-0.000000	15.0000	0.4296
13.000	0.000	1.007857	0.045900	0.055672	0.101572	0.000000	-0.000000	-1.188889	0.000000	-0.000000	15.0000	0.4301
14.000	0.000	1.079547	0.052657	0.061927	0.114584	0.000000	-0.000000	-1.274412	0.000000	-0.000000	15.0000	0.4305
15.000	0.000	1.150543	0.059794	0.064219	0.124013	0.000000	-0.000000	-1.357188	0.000000	-0.000000	15.0000	0.4309

Anexx 3. Mass and balance data export

*fw-pde engine1.mass - Notepad

File Edit Format View Help

```
#--------------------------------------------------
#
#   fw-pde engine
#
#  Dimensional unit and parameter data.
#  Mass & Inertia breakdown.
#--------------------------------------------------
#
Lunit =     0.0010 m
Munit =     1.0000 kg
Tunit = 1.0 s
#-------------------------
#  Gravity and density to be used as default values in trim setup (saves runtime typing).
#  Must be in the unit names given above (i.e. m,kg,s).
g   = 9.81
rho = 1.225
#-------------------------
#  Ixx... are item's inertias about item's own CG.
#
#  x,y,z system here must be exactly the same one used in the .avl input file
#     (same orientation, same origin location, same length units)
#
#     mass          x          y          z        Ixx        Iyy        Izz        Ixy        Ixz        Iyz
         1        403  -7.15e-15          0      0.103     0.0201      0.124          0          0          0 ! Main Wing
       1.2        335          0       29.4   0.000232     0.0405     0.0402          0    0.00102          0 ! Body's inertia
      0.25        350       -200          0      0.000      0.000      0.000 ! fuel
      0.25        350        200          0      0.000      0.000      0.000 ! fuel
       1.2        400          0          0      0.000      0.000      0.000 ! PJE
       0.5        100          0          0      0.000      0.000      0.000 ! equipment
      0.25        150          0          0      0.000      0.000      0.000 ! baterry
#-------------------------
```

ELECTROMAGNETIC FIELD DISTRIBUTION IN THE FAR-FIELD OF A PYRAMIDAL HORN ANTENNA

Robert POPA
Military Technical Academy „Ferdinand I", Bucharest, Romania (rbrtpopa@yahoo.com)
ORCID: 0009-0001-6675-0360

Gheorghe IUBU
Military Technical Academy „Ferdinand I", Bucharest, Romania (gh.iubu@gmail.com)

DOI: 10.19062/1842-9238.2022.20.2.5

Abstract: *The analysis of electromagnetic compatibility problems in radio electronic systems also involves the study of the distribution of the electromagnetic field generated by the antenna system of the device in the far-field area. Having a solid critical overview of the current research on the topic as a starting point, this article presents, in a synthetic, coherent and accessible manner, the procedure for the mathematical modelling of the electromagnetic field radiated in the far-field zone by a pyramidal horn antenna. The second part of the article presents the numerical and graphical results obtained by modelling the procedure described above by means of computer-assisted modelling.*

Keywords: *horn antenna, directivity function, directivity characteristic, opening angle of the directivity characteristic, maximum value of the directivity coefficient, electromagnetic compatibility.*

1. INTRODUCTION

The antenna system of any radio electronic equipment provides the interface of this equipment with the external medium of propagation of the electromagnetic field. The main function of this system is to transform, spatially directive and frequency-selective, when transmitting - the energy of high-frequency currents into the energy of electromagnetic waves, and vice versa, when receiving - the energy of electromagnetic waves into high-frequency currents.

The geometric fundamentals and notations used in the field of antenna theory for Cartesian and spherical coordinate systems are shown in Fig.1 [Balanis], where:

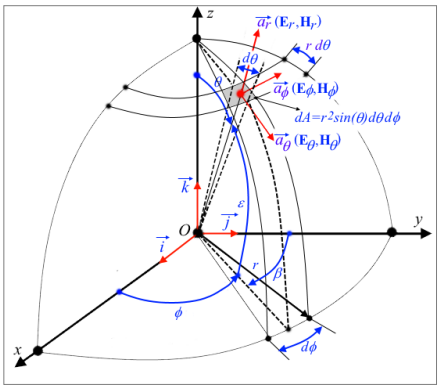

FIG. 1 Geometric foundations for the coordinate system and the notations used

- ϕ is the *azimuthal angle* and $\beta = \pi/2 - \phi$ the complementary angle;
- θ is the *polar angle* and $\varepsilon = \pi/2 - \theta$ the complementary angle called *the elevation angle*;
- $\left(\vec{i}, \vec{j}, \vec{k}\right)$, $\left|\vec{i}\right|^2 + \left|\vec{j}\right|^2 + \left|\vec{k}\right|^2 = 1$, the versors of the Cartesian coordinate system Oxyz;
- $\left(\overrightarrow{a_r}, \overrightarrow{a_\phi}, \overrightarrow{a_\theta}\right)$, $\left|\overrightarrow{a_r}\right|^2 + \left|\overrightarrow{a_\phi}\right|^2 + \left|\overrightarrow{a_\theta}\right|^2 = 1$, the versors of the spherical coordinate system;
- $\left(E_r, E_\phi, E_\theta\right)$, the electric field components in spherical coordinates. For the far field area ($2 \cdot \pi \cdot r/\lambda \gg 1$) $E_r \cong 0$;
- ,$\left(H_r, H_\phi, H_\theta\right)$ the magnetic field components in spherical coordinates. For the far field area $H_r \cong 0$;
- $dA = r^2 \cdot \sin(\theta) \cdot d\phi \cdot d\theta$, the area element in spherical coordinates;
- $d\Omega = dA/r^2 = \sin(\theta) \cdot d\phi \cdot d\theta$, the solid angle element in spherical coordinates;
- $k = \frac{2 \cdot \pi}{\lambda}$, the wave number.

2. FUNDAMENTAL ISSUES REGARDING THE DIRECTIVITY OF ANTENNAS

Any antenna radiates spherical waves that propagate in the radial direction in a coordinate system originating at the point of antenna placement. At large distances, spherical waves can be approximated as plane waves, this approximation being very useful because it simplifies many of the problems related to the mathematical modelling of an antenna.

If $\vec{\mathbf{E}}$ and $\overrightarrow{\mathbf{H}}$ are the orthogonal vectors that describe the values of the electric field intensity and the magnetic field intensity radiated by an antenna, related by the wave impedance in free space $\eta \cong 377\,\Omega$, *the power density* of the radiated electromagnetic wave *or the radiated power per unit area* is described by the modulus of the Poynting vector [16]:

$$S = \left|\vec{\mathbf{S}}\right| = \left|\vec{\mathbf{E}} \times \overrightarrow{\mathbf{H}^*}\right| = \frac{|E|^2}{2 \cdot \eta} = \frac{\eta}{2} \cdot |H|^2 \left[W/m^2\right]. \tag{1}$$

The *electric field strength* radiated by an antenna in the far-field region can be written as $E(r, \phi, \theta) = E^o(\phi, \theta) \cdot \frac{e^{-j \cdot k \cdot r}}{r}$, $E^o(\phi, \theta)$ being the distance independent component. Consequently, the expression of the radiated power density for the far-field region can be written as:

$$S(r, \phi, \theta) = \frac{\left|E(r, \phi, \theta)\right|^2}{2 \cdot \eta} = \frac{1}{r^2} \cdot \frac{\left|E^o(\phi, \theta)\right|^2}{2 \cdot \eta} =$$

$$= \frac{1}{r^2} \cdot \frac{1}{2 \cdot \eta} \cdot \left[\left|E_\theta^o(\phi, \theta)\right|^2 + \left|E_\phi^o(\phi, \theta)\right|^2 + \underbrace{\left|E_r^o(\phi, \theta)\right|^2}_{\gg 0 \text{ far field}} \right] \tag{2}$$

where, with $\left(E_\theta^o, E_\phi^o, E_r^o\right)$ denoted the radiated electric field components, independent of distance, represented in spherical coordinates. If $S \cdot dA$ is the power radiated by the surface element $dA = r^2 \cdot d\Omega$ where $d\Omega$ is the solid angle element in spherical coordinates, it can be written that $S \cdot dA = S \cdot r^2 \cdot d\Omega$.

The value $S(r,\phi,\theta) \cdot r^2 \square U(\phi,\theta)$ is called *the radiation intensity*, being dependent only on the direction of the radiated electromagnetic wave. The radiation intensity can be said to be the radiated power per unit solid angle (the unit of measurement is $W/steradian$). Based on relation (2) we obtain:

$$U(\phi,\theta) = r^2 \cdot S(r,\phi,\theta) = \frac{\left|E^o(\phi,\theta)\right|^2}{2 \cdot \eta} \cong \frac{1}{2 \cdot \eta}\left[\left|E_\theta^o(\phi,\theta)\right|^2 + \left|E_\phi^o(\phi,\theta)\right|^2\right].$$
$$U(\phi,\theta) \cong \frac{\eta}{2}\left[\left|H_\theta^o(\phi,\theta)\right|^2 + \left|H_\phi^o(\phi,\theta)\right|^2\right]. \quad (3)$$

If we denote by U_o the maximum value of the radiation intensity, it can be written:

$$U(\phi,\theta) = U_o \cdot F^2(\phi,\theta). \quad (4)$$

The function $F^2(\phi,\theta)$ describes the angular or spatial distribution of the radiation intensity and is called *the directivity function*, being also called *the power directivity function*. The directivity function itself is $F(\phi,\theta)$ and describes the angular or spatial distribution of the field strength, electric or magnetic. If $(\phi_{\max},\theta_{\max})$ are the angles at which this function reaches its maximum value, $F_{\max} = F(\phi_{\max},\theta_{\max})$, the function $F_n(\phi,\theta) = F(\phi,\theta)/F(\phi_{\max},\theta_{\max})$ is called *the normed directivity function*.

The directivity characteristic or *radiation characteristic* is the graphical representation of the directivity function. This can be represented on a linear scale or on a logarithmic scale (in dB), the latter allowing the secondary lobes to be highlighted. Also, the directivity characteristic can be represented by:

- 2D graphics, in sections $\phi = ct.$ or $\theta = ct.$, in Cartesian coordinates or in polar coordinates, on a linear, linear-logarithmic or logarithmic scale (in dB). The most important sections are $\phi = \phi_{\max} = ct.$ and $\theta = \theta_{\max} = ct.$;
- 3D graphics, in Cartesian coordinates ($\phi \to x$, $\theta \to y$, $F(\phi,\theta) \to z$), in spherical coordinates ($F(\phi,\theta) \cdot \sin(\theta) \cdot \cos(\phi) \to x$, $F(\phi,\theta) \cdot \sin(\theta) \cdot \sin(\phi) \to y$, $F(\phi,\theta) \cdot \cos(\theta) \to z$), on a linear or log scale (in dB).

In the specialized literature consulted [1] we found three-dimensional graphic representations of the directivity characteristic represented in sections, without giving explanations on the procedure used. In Fig. 2 graphically presents the calculation procedure found and used by the author of the article as well as its result, obtained according to the following calculation algorithm and graphic representation: $\theta \cdot \cos(\phi) \to x$, $\theta \cdot \sin(\phi) \to y$, $F_n(\phi,\theta) \to z$, if angles are expressed in radians or $\theta \cdot \cos(\phi \cdot \pi/180) \to x$, $\theta \cdot \sin(\phi \cdot \pi/180) \to y$, $F_n(\phi \cdot \pi/180, \theta \cdot \pi/180) \to z$, if the angles are expressed in degrees.

The most important parameters of the directivity of an antenna or antenna network are related to the shape of the directivity characteristic, respectively:

- ✓ *the opening angles at half power* refer to the opening angles, in the azimuthal plane - $\Delta\phi_{3dB}$ and in the elevation plane - $\Delta\theta_{3dB}$, of the main lobe of the directivity characteristic normalized at the level of half of the maximum radiated power;

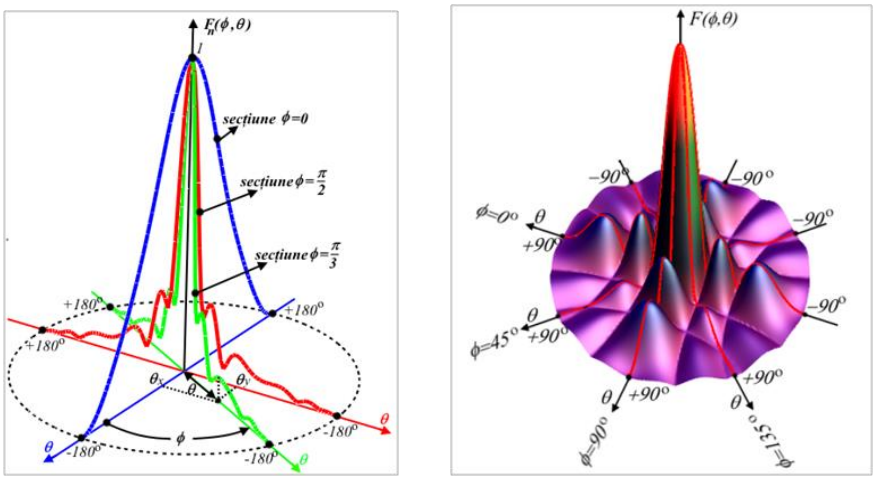

FIG. 2 Section $\phi = ct., 0 \le \phi < 180^\circ$ through the directivity characteristic, in 3D representation

- ✓ *the directivity coefficient* of the antenna is defined as the ratio between the radiation intensity $U(\phi,\theta)$ for a given direction and radiation intensity if the antenna would radiate the same power as an isotropic radiator (a solid angle equal to $4\cdot\pi$) [1]:

$$D(\phi,\theta) = \frac{U(\phi,\theta)}{U_{iso}} = 4\cdot\pi\cdot\frac{F_n^2(\phi,\theta)}{\int_0^{2\cdot\pi}\int_0^{\pi} F_n^2(\phi,\theta)\cdot\sin(\theta)\cdot d\theta\cdot d\phi}. \quad (5)$$

If the direction is not specified, the term *maximum value of the directivity coefficient* is used [1]:

$$D_o = D(\phi_{\max},\theta_{\max}) = \frac{4\cdot\pi}{\int_0^{2\cdot\pi}\int_0^{\pi} F_n^2(\phi,\theta)\cdot\sin(\theta)\cdot d\theta\cdot d\phi}; \quad (6)$$

- ✓ *the distribution and level of the secondary lobes* of the directivity characteristic.

3. MATHEMATICAL MODELLING OF THE ELECTROMAGNETIC FIELD RADIATED BY A PYRAMIDAL HORN ANTENNA

The horn antenna is one of the most widely used antennas, especially in the microwave field, either as an independent antenna or as a primary source in reflector antennas, equipping radio communication systems, radar systems or systems intended for radio astronomy. Also, some modern radio electronic systems using phased antenna arrays use the horn antenna as their elemental antenna. Its widespread applicability is determined by its constructional simplicity, ease of powering, versatility, and relatively high gain [1].

Depending on the opening of the radiating surface, horn antennas can have a rectangular opening or a conical opening. Horn antennas whose aperture is obtained by

widening (flaring) in a plane a rectangular waveguide are also called sector horn E, if the widening occurs in the E plane, or sector horn H, if the broadening occurs in the H plane. If the widening occurs in both planes, a pyramidal horn antenna is obtained (Fig. 3).

The meaning of the notations in the figure and the connection relationships between the geometric parameters of the pyramid horn antenna are:

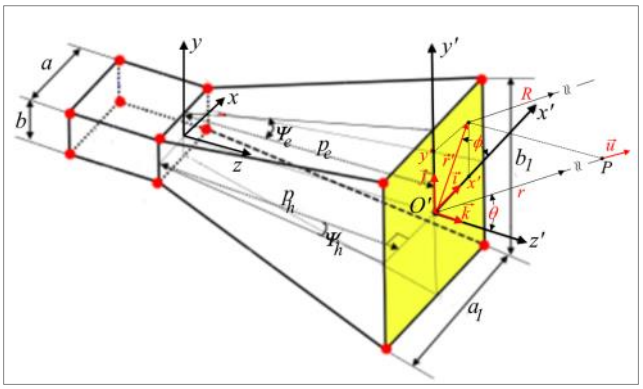

a) three-dimensional view

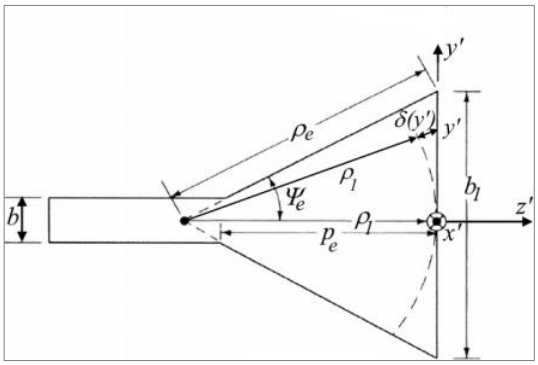

b) E plane view

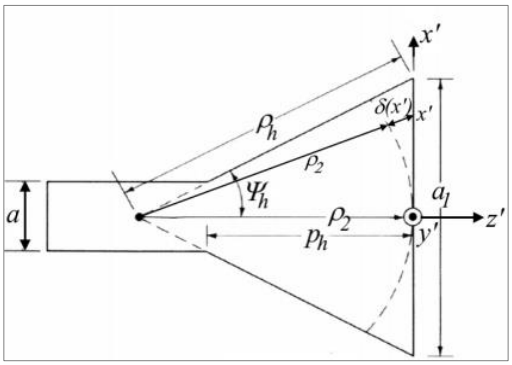

c) H plane view

FIG. 3 Pyramidal horn configuration *[1]*

- the opening semi-angles in the plans E and H, respectively Ψ_e and Ψ_h:

$$\psi_e = \text{arctg}\left[b_1/(2\cdot\rho_1)\right],\ \psi_h = \text{arctg}\left[a_1/(2\cdot\rho_2)\right]. \quad (7)$$

The values b_1, a_1 characterize the opening of the horn antenna and ρ_1, ρ_2 the radii of the circular arcs of equal phase, in the H and E planes. Normalized to the wavelength, these quantities are denoted by: $b_{1n} = b_1/\lambda, a_{1n} = a_1/\lambda, \rho_{1n} = \rho_1/\lambda, \rho_{2n} = \rho_2/\lambda$;

- the heights p_e, p_h of the trapezoidal sections in planes E and H:

$$p_e = \rho_1 - b/\left[2\cdot\tan(\psi_e)\right],\ p_h = \rho_2 - a/2\cdot\tan(\psi_h). \quad (8)$$

The condition of physical realization of the horn imposes the equality of the heights of the chimney in the two planes: $p_e = p_h$;

- $\vec{\mathbf{u}} = u_x\cdot\vec{i} + u_y\cdot\vec{j} + u_z\cdot\vec{k} = \sin(\theta)\cdot\cos(\phi)\cdot\vec{i} + \sin(\theta)\cdot\sin(\phi)\cdot\vec{j} + \cos(\theta)\cdot\vec{k}$ is the versor of the normal to the wavefront in the far-field region;
- $\vec{\mathbf{r}}' = x'\cdot\vec{i} + y'\cdot\vec{j}$ is the position vector of a point in the horn antenna aperture.

3.1 The procedure for evaluating the directivity function expression

In order to determine the expression of the directivity function of the pyramid horn antenna, it is necessary to go through several stages of calculation. Without going into the details of the proofs, the procedure for evaluating the expression of the directivity function of the pyramid horn antenna, assumes [1]:

1) *determining the distribution of components* $\overrightarrow{\mathbf{E}'}, \overrightarrow{\mathbf{H}'}$ *of the electromagnetic field* in the horn antenna opening (plane $x'O'y'$). There are many laborious mathematical models for determining the field distribution in the horn antenna opening. A fairly accurate model, described in the paper [Balanis], starts from the assumption of the field distribution in the opening of the funnel feeding waveguide described by the mode TE_{10}. At a point in the opening of the horn antenna, characterized by the position vector $\overrightarrow{\mathbf{r}'} = x' \cdot \vec{i} + y' \cdot \vec{j}$, this field is out of phase with respect to the centre of the horn opening $(x' = y' = 0)$ due to road differences $\delta(x'), \delta(y')$ (Fig. 3 b), 3c):

$$E_y^{'}(x',y') = E_o \cdot \cos\left(\frac{\pi}{a_1} \cdot x'\right) e^{-j \cdot k \cdot \left[\delta(x') + \delta(y')\right]},\ H_x^{'}(x',y') = -E_y^{'}(x',y')/\eta\,. \tag{9}$$

The path differences can be roughly deduced from the equalities:

$$\begin{aligned} &\rho_1^2 + y'^2 = \left[\rho_1 + \delta(y')\right]^2 = \rho_1^2 + 2 \cdot \rho_1 \cdot \delta(y') + \underbrace{\delta^2(y')}_{\approx 0} \Rightarrow \boxed{\delta(y') \approx \frac{1}{2}\frac{y'^2}{\rho_1}}, \\ &\rho_2^2 + x'^2 = \left[\rho_2 + \delta(x')\right]^2 = \rho_2^2 + 2 \cdot \rho_2 \cdot \delta(x') + \underbrace{\delta^2(x')}_{\approx 0} \Rightarrow \boxed{\delta(x') \approx \frac{1}{2}\frac{x'^2}{\rho_2}}. \end{aligned} \tag{10}$$

As a result, the approximate field components described by (9) become:

$$E_y^{'}(x',y') \approx E_o \cdot \cos\left(\frac{\pi}{a_1} \cdot x'\right) e^{-j \cdot \frac{k}{2} \cdot \left[\frac{x'^2}{\rho_2} + \frac{y'^2}{\rho_1}\right]},\ H_x^{'}(x',y') \approx -E_y^{'}(x',y')/\eta\,. \tag{11}$$

2) *determination of equivalent electric current density expressions* $\mathbf{J}'_s$ and *equivalent magnetic current density* $\mathbf{M}'_s$, from the opening of the radiant surface:

$$\begin{aligned} &\mathbf{J}'_s = \mathbf{n} \times \mathbf{H} = \vec{k} \times \vec{i} \cdot H_x^{'}(x',y') \approx -\vec{j} \cdot \frac{E_o}{\eta} \cos\left(\frac{\pi}{a_1} \cdot x'\right) e^{-j \cdot \frac{k}{2} \cdot \left[\frac{x'^2}{\rho_2} + \frac{y'^2}{\rho_1}\right]} = \vec{j} \cdot J_y(x',y'), \\ &\mathbf{M}'_s = -\mathbf{n} \times \mathbf{E} = -\vec{k} \times \vec{j} \cdot E_y^{'}(x',y') \approx \vec{i} \cdot E_o \cdot \cos\left(\frac{\pi}{a_1} \cdot x'\right) e^{-j \cdot \frac{k}{2} \cdot \left[\frac{x'^2}{\rho_2} + \frac{y'^2}{\rho_1}\right]} = \vec{i} \cdot M_x(x',y'). \end{aligned} \tag{12}$$

3) *conversion of vector components* $\mathbf{J}'_s = \vec{i} \cdot J_x + \vec{j} \cdot J_y + \vec{k} \cdot J_z = \vec{j} \cdot J_y$ and $\mathbf{M}'_s = \vec{i} \cdot M_x + \vec{j} \cdot M_y + \vec{k} \cdot M_z = \vec{i} \cdot M_x$, from Cartesian coordinates to spherical coordinates using the matrix relation:

$$\begin{pmatrix} A_r \\ A_\theta \\ A_\phi \end{pmatrix} = \begin{pmatrix} \sin(\theta)\cdot\cos(\phi) & \sin(\theta)\cdot\sin(\phi) & \cos(\theta) \\ \cos(\theta)\cdot\cos(\phi) & \cos(\theta)\cdot\sin(\phi) & -\sin(\theta) \\ -\sin(\phi) & c\cos(\phi) & 0 \end{pmatrix} \cdot \begin{pmatrix} A_x \\ A_y \\ A_z \end{pmatrix}. \tag{13}$$

Finally, it is obtained that:

$$\begin{aligned}\mathbf{J}'_s(x',y',\phi,\theta)&=\left[\overrightarrow{a_r}\cdot\sin(\theta)\cdot\sin(\phi)+\overrightarrow{a_\theta}\cdot\cos(\theta)\cdot\sin(\phi)+\overrightarrow{a_\phi}\cdot\cos(\phi)\right]\cdot J_y(x',y')\\ \mathbf{M}'_s(x',y',\phi,\theta)&=\left[\overrightarrow{a_r}\cdot\sin(\theta)\cdot\cos(\phi)+\overrightarrow{a_\theta}\cdot\cos(\theta)\cdot\cos(\phi)-\overrightarrow{a_\phi}\cdot\sin(\phi)\right]\cdot M_x(x',y').\end{aligned} \tag{14}$$

4) determination of *the magnetic potential vector* **A** produced by the electric current density $\mathbf{J}'_s$ and of *the electric potential vector* **F** produced by the magnetic current density $\mathbf{M}'_s$ in the far field zone:

$$\mathbf{A}(r,\phi,\theta)=\frac{\mu}{4\cdot\pi}\cdot\iint_{S'}\mathbf{J}(x',y',\phi,\theta)\cdot\frac{e^{-j\cdot k\cdot R}}{R}\cdot ds', \tag{15}$$

$$\mathbf{F}(r,\phi,\theta)=\frac{\varepsilon}{4\cdot\pi}\cdot\iint_{S'}\mathbf{M}'_s(x',y',\phi,\theta)\cdot\frac{e^{-j\cdot k\cdot R}}{R}\cdot ds'. \tag{16}$$

From Fig. 3. a) it follows that

$$R=r-\Delta r=r-\underset{\Delta r}{\overrightarrow{r'}\cdot\vec{u}}=r-\underbrace{\left[x'\cdot\sin(\theta)\cdot\cos(\phi)+y'\cdot\sin(\theta)\cdot\sin(\phi)\right]}_{\Delta r}.$$

Influence of path difference Δr on the amplitude being negligible and having an effect only on the phase, with the area element $ds'=dx'\cdot dy'$, the relations (15) and (16) becomes:

$$\mathbf{A}(r,\phi,\theta)=\frac{\mu}{4\cdot\pi}\cdot\frac{e^{-j\cdot k\cdot r}}{r}\cdot\mathbf{N}(\phi,\theta), \tag{17}$$

with

$$\mathbf{N}(\phi,\theta)=\int_{-a_1/2}^{+a_1/2}\int_{-b_1/2}^{+b_1/2}\mathbf{J}'_s(x',y',\phi,\theta)\cdot e^{-j\cdot k\cdot\left[x'\cdot\sin(\theta)\cdot\cos(\phi)+y'\cdot\sin(\theta)\cdot\sin(\phi)\right]}dx'\cdot dy' \tag{17-a}$$

and

$$\mathbf{F}(r,\phi,\theta)=\frac{\varepsilon}{4\cdot\pi}\cdot\frac{e^{-j\cdot k\cdot r}}{r}\cdot\mathbf{L}(\phi,\theta), \tag{18}$$

with

$$\mathbf{L}(\phi,\theta)=\int_{-a_1/2}^{+a_1/2}\int_{-b_1/2}^{+b_1/2}\mathbf{M}'_s(x',y',\phi,\theta)\cdot e^{-j\cdot k\cdot\left[x'\cdot\sin(\theta)\cdot\cos(\phi)+y'\cdot\sin(\theta)\cdot\sin(\phi)\right]}dx'\cdot dy' \tag{18-a}$$

Based on relations (14), separating from relations (17-a) and (18-a) the components of versors $\overrightarrow{a_\phi}$, $\overrightarrow{a_\theta}$

$$\begin{aligned}N_\phi(\phi,\theta)&=-(E_o/\eta)\cdot\cos(\phi)\cdot I_1(\phi,\theta)\cdot I_2(\phi,\theta)\\ N_\theta(\phi,\theta)&=-(E_o/\eta)\cdot\cos(\theta)\cdot\sin(\phi)\cdot I_1(\phi,\theta)\cdot I_2(\phi,\theta),\\ L_\phi(\phi,\theta)&=-E_o\cdot\sin(\phi)\cdot I_1(\phi,\theta)\cdot I_2(\phi,\theta)\\ L_\theta(\phi,\theta)&=E_o\cdot\cos(\theta)\cdot\cos(\phi)\cdot I_1(\phi,\theta)\cdot I_2(\phi,\theta),\end{aligned} \tag{19}$$

in which:

$$I_1(\phi,\theta)=\int_{-a_1/2}^{+a_1/2}\cos\left(\frac{\pi}{a_1}x'\right)\cdot e^{-j\cdot k\cdot\left[x'^2/2\rho_2-x'\cdot\sin(\theta)\cdot\cos(\phi)\right]}\cdot dx', \tag{20}$$

(2)

$$I_2(\phi,\theta)=\int_{-b_1/2}^{+b_1/2} e^{-j\cdot k\cdot\left[y'^2/(2\rho_1)-y'\cdot\sin(\theta)\cdot\sin(\phi)\right]}\cdot dy'.$$

With the notations:

$$\begin{aligned}
t_1(\phi,\theta)&=\sqrt{2\cdot\rho_{1n}}\cdot\left[-\mathrm{tg}(\Psi_e)-\sin(\theta)\cdot\sin(\phi)\right],\\
t_2(\phi,\theta)&=\sqrt{2\cdot\rho_{1n}}\cdot\left[\mathrm{tg}(\Psi_e)-\sin(\theta)\cdot\sin(\phi)\right],
\end{aligned}\tag{3}$$

$$\begin{aligned}
t_1'(\phi,\theta)&=\sqrt{2\cdot\rho_{2n}}\cdot\left[-\mathrm{tg}(\Psi_h)-\sin(\theta)\cdot\cos(\phi)-1/(2\cdot a_{1n})\right],\\
t_2'(\phi,\theta)&=\sqrt{2\cdot\rho_{2n}}\cdot\left[\mathrm{tg}(\Psi_h)-\sin(\theta)\cdot\cos(\phi)-1/(2\cdot a_{1n})\right],
\end{aligned}\tag{22-a}$$

$$\begin{aligned}
t_1''(\phi,\theta)&=\sqrt{2\cdot\rho_{2n}}\cdot\left[-\mathrm{tg}(\Psi_h)-\sin(\theta)\cdot\cos(\phi)+1/(2\cdot a_{1n})\right],\\
t_2''(\phi,\theta)&=\sqrt{2\cdot\rho_{2n}}\cdot\left[\mathrm{tg}(\Psi_h)-\sin(\theta)\cdot\cos(\phi)+1/(2\cdot a_{1n})\right],
\end{aligned}\tag{22-b}$$

$$\begin{aligned}
f_1(\phi,\theta)&=\pi\cdot\rho_{2n}\cdot\left[\sin(\theta)\cdot\cos(\phi)+1/(2\cdot a_{1n})\right]^2,\\
f_2(\phi,\theta)&=\pi\cdot\rho_{2n}\cdot\left[\sin(\theta)\cdot\cos(\phi)-1/(2\cdot a_{1n})\right]^2,\\
f_3(\phi,\theta)&=\pi\cdot\rho_{1n}\cdot\left[\sin(\theta)\cdot\sin(\phi)\right]^2,
\end{aligned}\tag{22-c}$$

is obtained:

$$\begin{aligned}
I_1(\phi,\theta)=\frac{\lambda}{2}\sqrt{\frac{\rho_{2n}}{2}}\cdot\Big\{&e^{j\cdot f_1(\phi,\theta)}\cdot C\left[t_1'(\phi,\theta),t_2'(\phi,\theta)\right]+\\
&+e^{j\cdot f_2(\phi,\theta)}\cdot C\left[t_1''(\phi,\theta),t_2''(\phi,\theta)\right]\Big\}=\lambda\cdot I_{1n}(\phi,\theta)
\end{aligned}\tag{4}$$

$$I_2(\phi,\theta)=\lambda\cdot\sqrt{\frac{\rho_{1n}}{2}}\cdot e^{j\cdot f_3(\phi,\theta)}\cdot C\left[t_1(\phi,\theta),t_2(\phi,\theta)\right]=\lambda\cdot I_{2n}(\phi,\theta).\tag{5}$$

The function $C(x,y)$ is defined as $C(x,y)\equiv C_F(y)-C_F(x)-j\cdot\left[S_F(y)-S_F(x)\right]$ where C_F, S_F represent the Fresnel integrals.

5) determination of *field intensity expressions* in the far-field region:

$E_r(r,\phi,\theta)\equiv 0$, $H_r(r,\phi,\theta)\equiv 0$,

$$\begin{aligned}
E_\theta(r,\phi,\theta)&=-j\cdot\frac{k\cdot e^{-j\cdot k\cdot r}}{4\cdot\pi\cdot r}\cdot\left[L_\phi(\phi,\theta)+\eta\cdot N_\theta(\phi,\theta)\right],\\
E_\phi(r,\phi,\theta)&=+j\cdot\frac{k\cdot e^{-j\cdot k\cdot r}}{4\cdot\pi\cdot r}\cdot\left[L_\phi(\phi,\theta)-\eta\cdot N_\theta(\phi,\theta)\right],\\
H_\theta(r,\phi,\theta)&=-j\cdot\frac{k\cdot e^{-j\cdot k\cdot r}}{4\cdot\pi\cdot r}\cdot\frac{1}{\eta}\cdot\left[L_\phi(\phi,\theta)-\eta\cdot N_\theta(\phi,\theta)\right],\\
H_\phi(r.\phi,\theta)&=-j\cdot\frac{k\cdot e^{-j\cdot k\cdot r}}{4\cdot\pi\cdot r}\cdot\frac{1}{\eta}\cdot\left[L_\phi(\phi,\theta)+\eta\cdot N_\theta(\phi,\theta)\right].
\end{aligned}\tag{6}$$

The electric field intensity in the far-field region of the pyramidal horn radiator is obtained by vector summation of the components $\overrightarrow{E_\phi(r,\theta,\phi)}$ and $\overrightarrow{E_\theta(r,\theta,\phi)}$, respectively $\overrightarrow{E(r,\theta,\phi)}=E_\phi(r,\theta,\phi)\cdot\overrightarrow{a_\phi}+E_\theta(r,\theta,\phi)\cdot\overrightarrow{a_\theta}$.

Based on relations (25), for the components of the electric field $\overrightarrow{E_\phi(r,\theta,\phi)}$ and $\overrightarrow{E_\theta(r,\theta,\phi)}$ in the far field area, is obtained:

$$E_\phi(r,\theta,\phi)=\frac{\lambda}{r}\cdot e^{-j\cdot k\cdot r}\cdot\underbrace{\left(j\cdot\frac{E_o}{2}\right)\cdot\left\{\cos(\phi)\cdot\left[\cos(\theta)+1\right]\cdot I_{1n}(\theta,\phi)\cdot I_{2n}(\theta,\phi)\right\}}_{E_\phi^o(\phi,\theta)}= \tag{26}$$

$$=\frac{\lambda}{r}\cdot e^{-j\cdot k\cdot r}\cdot E_\phi^o(\phi,\theta)$$

$$E_\theta(r,\theta,\phi)=\frac{\lambda}{r}\cdot e^{-j\cdot k\cdot r}\cdot\underbrace{\left(j\cdot\frac{E_o}{2}\right)\cdot\left\{\sin(\phi)\cdot\left[\cos(\theta)+1\right]\cdot I_{1n}(\theta,\phi)\cdot I_{2n}(\theta,\phi)\right\}}_{E_\theta^o(\phi,\theta)}= \tag{27}$$

$$=\frac{\lambda}{r}\cdot e^{-j\cdot k\cdot r}\cdot E_\theta^o(\phi,\theta).$$

Therefore

$$\overrightarrow{E(r,\phi,\theta)}=\underbrace{\left[E_\phi^o(\phi,\theta)\cdot\overrightarrow{a_\phi}+E_\phi^o(\phi,\theta)\cdot\overrightarrow{a_\theta}\right]}_{\overrightarrow{E_o(\phi,\theta)}}\cdot\frac{\lambda}{r}\cdot\mathrm{e}^{-j\cdot k\cdot r}=\frac{\lambda}{r}\cdot\mathrm{e}^{-j\cdot k\cdot r}\cdot\overrightarrow{E_o(\phi,\theta)} \tag{7}$$

where $\overrightarrow{E_0(\phi,\theta)}$ is the distance-independent component of the electric field:

$$\overrightarrow{E_o(\phi,\theta)}=E_\phi^o(\phi,\theta)\cdot\overrightarrow{a_\phi}+E_\phi^o(\phi,\theta)\cdot\overrightarrow{a_\theta}=$$

$$=\left(j\cdot\frac{E_o}{2}\right)\cdot\left\{\left[\cos(\theta)+1\right]\cdot I_{1n}(\theta,\phi)\cdot I_{2n}(\theta,\phi)\right\}\cdot\left[\cos(\phi)\cdot\overrightarrow{a_\phi}+\sin(\phi)\cdot\overrightarrow{a_\theta}\right]. \tag{29}$$

The module of this component is:

$$E_o(\phi,\theta)=\left|E_\phi^o(\phi,\theta)\cdot\overrightarrow{a_\phi}+E_\phi^o(\phi,\theta)\cdot\overrightarrow{a_\theta}\right|=$$

$$=E_o\cdot\underbrace{\frac{1}{2}\left\{\left[\cos(\theta)+1\right]\cdot I_{1n}(\theta,\phi)\cdot I_{2n}(\theta,\phi)\right\}}_{F_h(\phi,\theta)}\cdot\overbrace{\left[\cos^2(\phi)+\sin^2(\phi)\right]}^{1}=E_o\cdot F_h(\phi,\theta), \tag{30}$$

where $F_h(\phi,\theta)$ is ***the directivity function of the pyramid horn antenna***:

$$\boxed{F_h(\phi,\theta)=\frac{1}{2}\cdot\left[1+\cos(\theta)\right]\cdot I_{1n}(\phi,\theta)\cdot I_{2n}(\phi,\theta)} \tag{8}$$

The maximum value of this function is obtained for zero values of the angular coordinates (ϕ,θ):

$$\boxed{\left|F_h(0,0)\right|=F_{\max}=\left|I_{1n}(0,0)\cdot I_{2n}(0,0)\right|.} \tag{9}$$

3.2 The analysis of the maximum value of the directivity coefficient

The maximum value of the directivity coefficient of the pyramid horn antenna can be calculated with the relation [1]:

$$D_{o\_hp}=8\cdot\pi\cdot\frac{\rho_{1n}\cdot\rho_{2n}}{a_{1n}\cdot b_{1n}}\cdot\left|C(u,v)\right|^2\cdot\left[C_F^2(w)+S_F^2(w)\right], \tag{33}$$

$$\mathrm{u}=\frac{1}{\sqrt{2}}\left(\frac{\sqrt{\rho_{2n}}}{a_{1n}}+\frac{a_{1n}}{\sqrt{\rho_{2n}}}\right),\ \mathrm{v}=\frac{1}{\sqrt{2}}\left(\frac{\sqrt{\rho_{2n}}}{a_{1n}}-\frac{a_{1n}}{\sqrt{\rho_{2n}}}\right),\ w=\frac{b_{1n}}{\sqrt{2\cdot\rho_{1n}}} \tag{10}$$

.

Having seen that [1]

$$D_{o\_hE} = \frac{64}{\pi} \cdot \frac{a_n \cdot \rho_{1n}}{b_{1n}} \cdot \left| C_F^2(w) + S_F^2(w) \right|, \tag{11}$$

$$D_{o\_hH} = \frac{\pi}{32} \cdot \frac{b_n \cdot \rho_{2n}}{a_{1n}} \cdot \left| C(u,v) \right|^2 \tag{12}$$

represent the expressions of *the maximum values of the directivity coefficients of the sectoral horn antennas*, in planes E and H, relation (33) can be written:

$$D_{o\_hp} = \frac{\pi}{32} \cdot \frac{1}{a_n \cdot b_n} \cdot D_{o\_hE} \cdot D_{o\_hH} \cdot \tag{13}$$

Maximizing value D_{o_hp} is equivalent to maximizing values D_{o_hE} and D_{o_hH}. The values of the coefficients D_{o_hE} and D_{o_hH} each depends only on the parameters that characterize the opening of the horn in planes E or H. In Fig. 4 shows the dependence of the maximum value of the directivity coefficient on the antenna parameters, for the sectoral horn antennas, in the E and H planes. It is found that, in the case of the sectoral horn E, for a value ρ_{1n} given the height at the apex, normed at λ, there is an optimal value b_{1n} of the antenna opening in the plane E that maximizes the value of the directivity coefficient:

$$b_{1n\_opt} = \sqrt{2 \cdot \rho_{1n}} \tag{14}$$

Similarly, for a sector horn antenna in the H plane,

$$a_{1n\_opt} = \sqrt{3 \cdot \rho_{2n}} \tag{15}$$

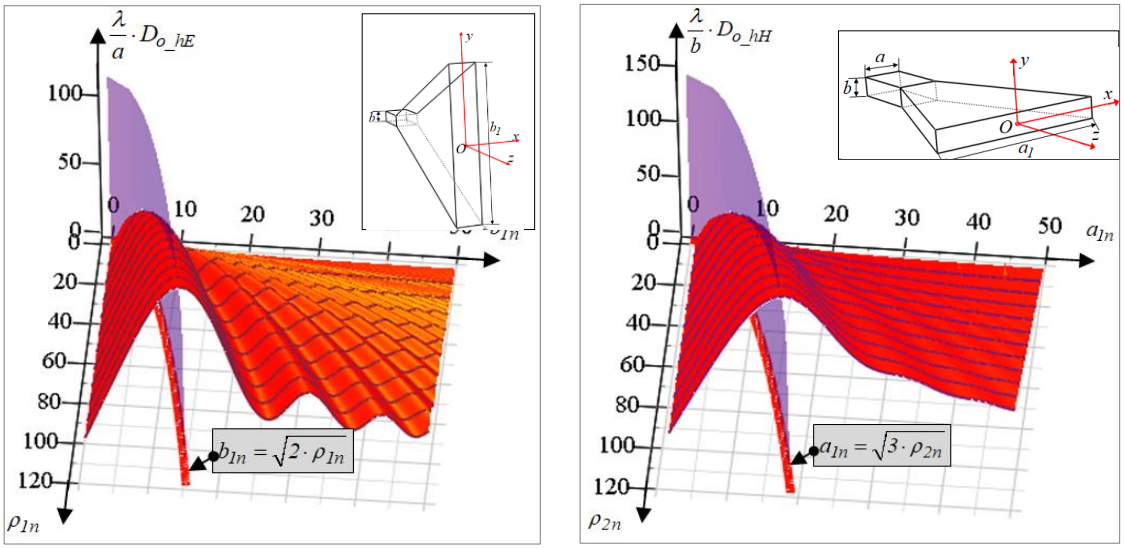

a) sectoral horn, E plane b) sectoral horn, H plane

FIG. 4 Dependence on the antenna parameters of the maximum value of the directivity coefficient, for sector horn antennas

For these values, $u = \frac{1}{\sqrt{2}}\left(\frac{1}{\sqrt{3}} + \sqrt{3}\right)$, $v = \frac{1}{\sqrt{2}}\left(\frac{1}{\sqrt{3}} - \sqrt{3}\right)$, $w = 1$ and the optimal expression of the maximum value of the directivity coefficient of the pyramid horn antenna is:

$$D_{o\_hp\_opt} = 15.83 \cdot \sqrt{\rho_{1n} \cdot \rho_{2n}} \ . \tag{40}$$

Fulfillment of the physical feasibility condition $p_e = p_h \Leftrightarrow \rho_1 \left(1 - \frac{b}{b_1}\right) = \rho_2 \left(1 - \frac{a}{a_1}\right)$ but also of conditions (38) and (39), impose the following relationship between the optimal apertures of the pyramidal horn antenna, normalized to λ:

$$a_{1n\_opt} = \frac{a_n + \sqrt{a_n^2 + 6 \cdot b_{1n\_opt} \cdot \left(b_{1n\_opt} - b_n\right)}}{2} \tag{41}$$

The maximum value of the directivity coefficient can also be determined based on the directivity function, using relations (6), (31) and (32) and the numerical evaluation of the integrals. The differences are not greater than 0.25 dbs.

4. RESULTS OBTAINED THROUGH COMPUTER MODELLING

Based on the mathematical formalism presented above, a program was created in MATHCAD to evaluate, numerically and graphically, the performance of the directivity of a pyramid horn antenna.

With the help of library functions of the programming environment and functions built by the programmer, the program allows:

- ✓ calculation and graphic representation of the most important parameters of the directivity of the pyramidal horn antenna:
  - calculation of the directivity function;
  - graphic plotting of the directivity characteristic, in sections, in Cartesian coordinates, polar/spherical coordinates, on a linear scale or a logarithmic scale in dB;
  - graphic plotting of the directivity characteristic in spherical coordinates (3D format), on a linear or logarithmic scale in dB;
  - visualization of the directivity characteristic represented in spherical coordinates, together with the geometric sketch of the pyramid horn antenna that has this characteristic;
  - calculation of the opening angles at -3 dB of the main lobe of the directivity characteristic, in two planes – the azimuthal plane (H) and the elevation plane (E);
  - calculation of the maximum value of the directivity coefficient;
- ✓ the generation of models of numerical calculation functions and graphics generators not included in the programming environment but which, through the generality of the arguments, help the development of the calculation program but also the understanding of the obtained graphic representations:
  - the decibel conversion function for graphical representation on a logarithmic scale in spherical coordinates;
  - functions for calculating the opening angles at -3 dB of the main lobe of the directivity characteristic, in two planes – the azimuthal plane (H) and the elevation plane (E);
  - the function of generating and 3D graphic representation of scaled geometric sketches of modelled chimney antennas;
  - functions for generating the axes of the Cartesian coordinate system, the axes and circle arcs for 3D delimitation of the opening level at -3dB of the directivity characteristics;

- calculation functions and graphic plotting of spherical caps intended to delimit the different levels of the characteristics represented in spherical coordinates, on a logarithmic scale in dbs.

The results obtained for a working frequency $f_o = 2{,}5\,GHz \Leftrightarrow \lambda = 12\,cm$ are presented below.

To begin with, based on the geometric model presented in Fig. 5.a, the coordinates of the peaks, the parametric equations of its sides and axes were defined ($N_v = 12$ peaks, $N_l = 20$ sides and $N_a = 3$ axes). These elements were introduced into the program and generated the representation in Fig. 5b.

The calculation performed by the program for the maximum value of the directivity function of the pyramid horn antenna returns the result: $F_{max} = F_h(0,0) = 7.71$.

Opening angles at - 3dB of the main lobe of the directivity characteristic of the pyramidal horn antenna for the sections $\phi = 0$, respectively $\phi = \pi/2$, were evaluated with the "root" function available in Mathcad:

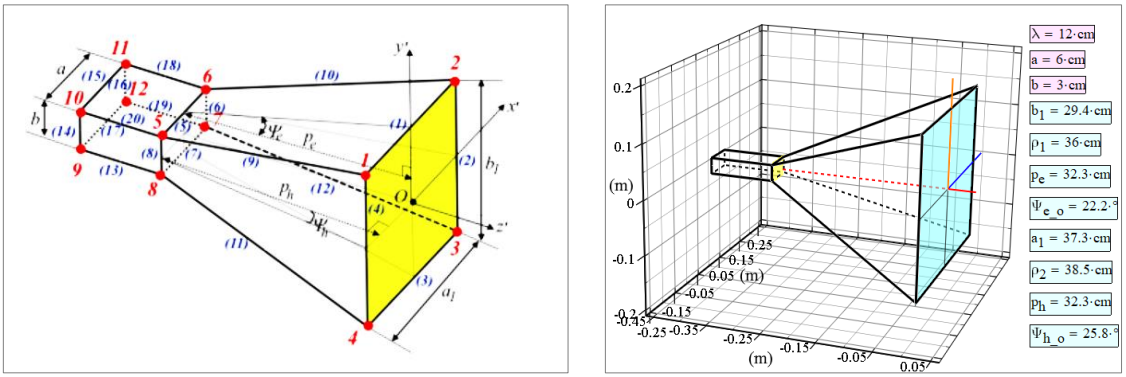

a) the structure of the geometric model of the pyramid horn antenna

b) scale sketch of pyramidal horn antenna

FIG. 5 The geometric model used and the sketch of the pyramid horn antenna drawn to scale

$$\Delta\theta_{hH\_3dB} = 2 \cdot root\left[F_h(0,\theta) - \frac{\sqrt{2}}{2} \cdot F_{max}, \theta, 0, \pi\right] = 24.8^o; \tag{16}$$

$$\Delta\theta_{hE\_3dB} = 2 \cdot root\left[F_h\left(\frac{\pi}{2},\theta\right) - \frac{\sqrt{2}}{2} \cdot F_{max}, \theta, 0, \pi\right] = 21.8^o \tag{17}$$

The maximum value of the directivity coefficient calculated based on relations (33) and (34) is $D_{o\_hp} = 49.1\,(16.91\,dB)$ and the one obtained based on relation (6), using approximate calculation methods of integrals, is $D_{o\_hp} = 50{,}8\,(17.06\,dB)$.

In Fig. 5 ÷ Fig. 7 shows the results of the graphical representations of the directivity characteristic of the pyramid horn antenna, obtained with the program mentioned above.

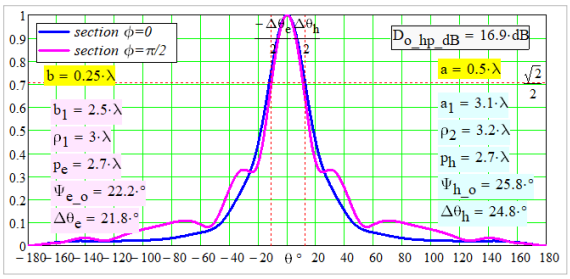

a) Cartesian coordinates, linear scale

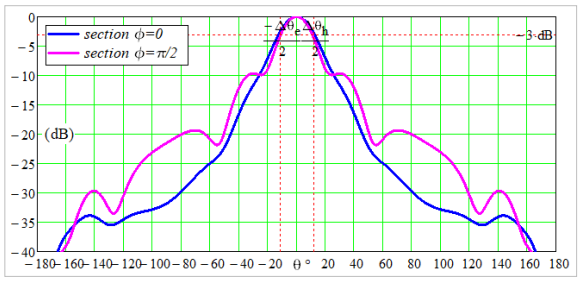

b) Cartesian coordinates, logarithmic scale in dB

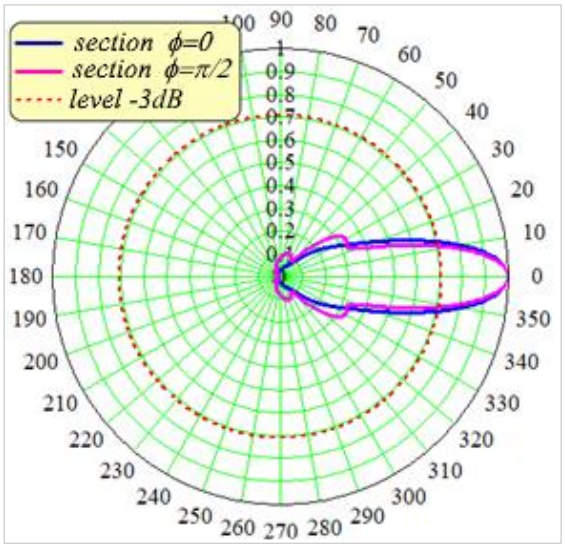

c) polar coordinates, linear scale

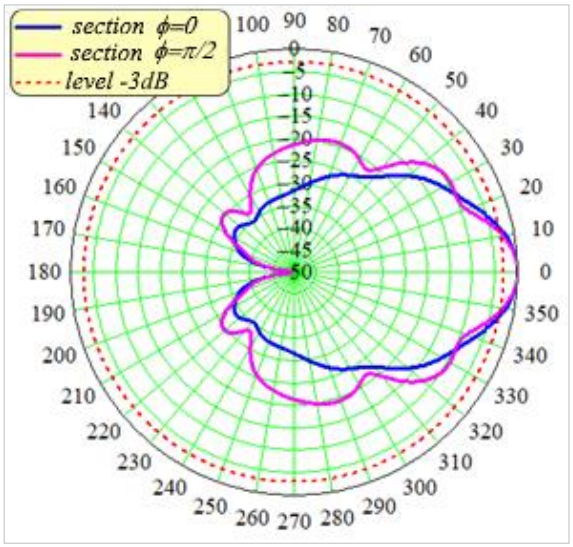

d) polar coordinates, logarithmic scale in dB

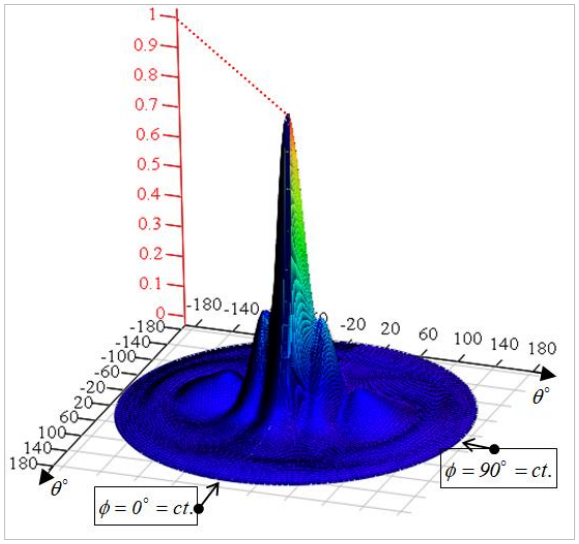

e) sections $\phi = ct.$ in 3D representation, linear scale

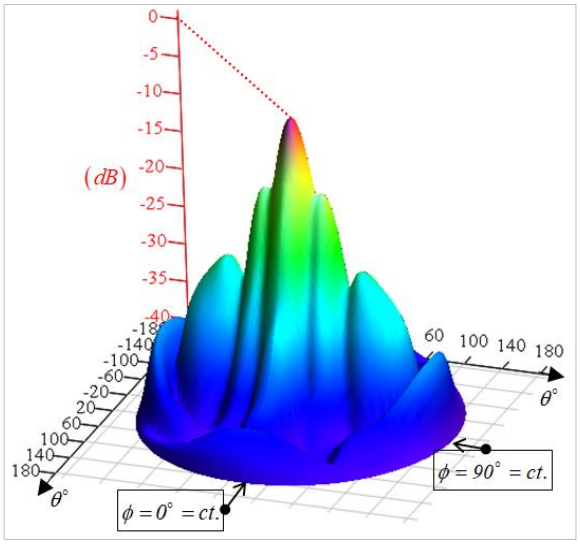

f) sections $\phi = ct.$ in 3D representation, logarithmic scale in dB

FIG. 5 Directivity characteristic of the pyramidal horn antenna in sections $\phi = ct.$

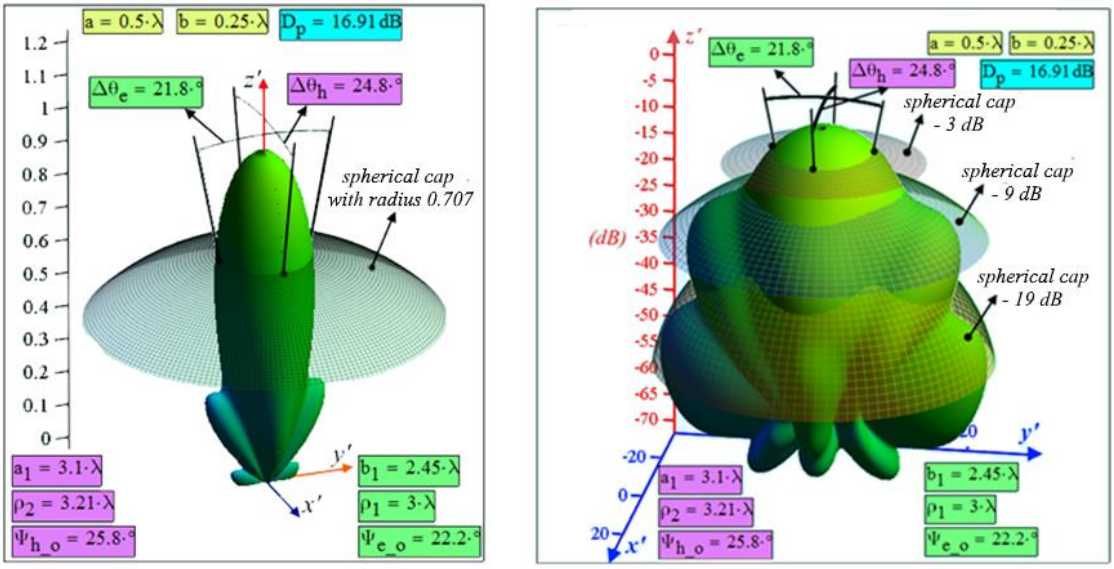

a) linear scale b) logarithmic scale in dB

FIG.6 Representation in spherical coordinates of the directivity characteristic of the pyramid horn antenna

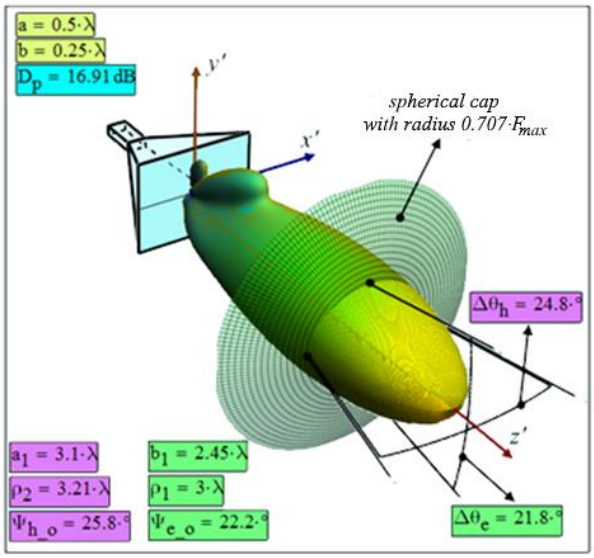

Fig.7 Representation in spherical coordinates - linear scale, of the directivity characteristic of the pyramidal horn antenna together with its scale sketch

5. CONCLUSIONS

The analysis of the obtained results leads to the following conclusions:

- ✓ the absolute value of the electric field and magnetic field intensities generated by a pyramidal horn antenna in the far field area is directly proportional to the module of its directivity function;
- ✓ the shape of the directivity characteristic and the values of the opening angles of its main lobe in planes E and H as well as the maximum value of the directivity coefficient do not depend on the wavelength, being dependent only on the geometric values normalized to the wavelength $b_{1n}, \rho_{1n}, a_{1n}, \rho_{2n}$.

- ✓ for each set of values ρ_{1n}, ρ_{2n} there are optimal values of the horn antenna aperture that maximize the directivity coefficient: $b_{1\_opt} = \sqrt{2\rho_{1n}}$, $a_{1\_opt} = \sqrt{3\rho_{2n}}$;
- ✓ for the modelled configuration, with $\rho_{1n} = 3,\ b_{1n} = b_{1n\_opt} = 2.45,\ \rho_{2n} = 3.21,$ $a_{1n} = a_{1n\_opt} = 3.1$, the values resulted are $\Delta\theta_e = 21.8^\circ$, $\Delta\theta_h = 24.8^\circ$, $D_{o\_hp} = 16.91\,dB$. Also, the directivity characteristic presents a main lobe and several significant secondary lobes, adjacent to the main lobe (without zero crossings), with the level of $-9.7\,dB, -19.4\,dB$ and $-31.2\,dB$.

The shape of the directivity characteristic of the pyramid horn antenna is correlated with its constructive dimensions. Along with the increase in size of the dimensions ρ_1, ρ_2 normalized to the wavelength, the directivity of the horn antenna improves but the phase error between the edge and the centre of the horn increases, the approximations used in relations (10) and (11) which allowed the quadratic approximation of the phase in the opening of the horn antenna and based on which they could Fresnel integrals should be used, requiring possible phase corrections. By calling the numerical integral, however, evaluations of the directivity of the horn antenna can be made, starting from exact expressions of the path differences from relations (10) and (11).

REFERENCES

[1] C. A. Balanis, „*Antenna Theory: Analysis and Design, Fourth Edition*", New York, John Wiley &Sons Publishers, Inc., 2016;

[2] G. Gavrilă, „Complemente de unde electromagnetice", Bucharest, Editura tehnică, 2018;

[3] T. A. Milligan, „*Modern Antenna Design, Second Edition*", Willey-IEEE Press, 2005;

[4] ***IEEE Standard Association, "*IEEE 145-2013 Standard for Definitions of Terms for Antennas*", 11 12 2013. [Online]. Available: https://standards.ieee.org/ieee/145/4705/;

[5] W. L. Stutzman și G. A. Thiele, „*Antenna Theory and Design, Third Edition*", New York, John Wiley & Sons Publishers, Inc., 2012;

[6] S. J. Orfanidis, „*Electromagnetic Waves and Antennas*", Piscataway, New Jersey, Rutgers University, 2016;

[7] ***„*Antenna Engineering Handbook, 5th Edition*", New York, McGraw-Hill Book Company, 2018;

[8] R. E. Collins, „*Antennas and Radiowave Propagation*", New York, New York, McGraw-Hill Book Company, 1985;

[9] N. K. Nikolova, „*Lecture notes on antenna engineering*" 2018. [Interactiv]. Available: http://www.ece.mcmaster.ca/faculty/nikolova/antenna_dload/current_lectures/.

NUMERICAL MODELING OF AN ENERGY MANAGEMENT SYSTEM FOR A UAV DESIGN POWERED BY PHOTOVOLTAIC CELLS

Andrei BUZDUGAN
Military Technical Academy Ferdinand I (andrei_buzdu@yahoo.com)
ORCID: 0000-0001-6004-3115

Nicolae JULA
Military Technical Academy Ferdinand I (nicolae.jula@gmail.com)

Albert BĂLTEANU
"Henri Coandă" Air Force Academy, Braşov, Romania (albert_balteanu@yahoo.com)

DOI: 10.19062/1842-9238.2022.20.2.6

Abstract: *UAVs are increasingly used for tasks such as surveillance, monitoring, and inspection, but their effectiveness is limited by their energy storage and generation capacity. Therefore, optimizing the energy system of a solar-powered UAV is crucial to extend its range and duration, and numerical modeling can help achieve this goal.*

In this particular study, researchers focused on a solar-powered UAV with a 151 cm wingspan. They used three different energy sources to power the UAV, and then simulated its performance using numerical modeling. The aim was to find the optimal energy source for each stage of flight and ensure a steady and efficient power supply throughout the entire mission.

The findings of this study have important implications for the development of new UAVs with exceptional performance.

Keywords: *numerical modeling, algorithm, photovoltaic cells, fuel cell, UAV, drone, battery*

1. INTRODUCTION

Over the past decade, the use of unmanned aerial vehicles (UAVs) in military operations has revolutionized the way we think about warfare. These innovative aircrafts, equipped with complex power systems fueled by photovoltaic cells, have proven to be highly effective tools for conducting operations in a more efficient and less risky manner [4]. As technology continues to develop, the civilian world is taking notice and exploring new uses for these versatile machines [3].

With the ability to fly missions at higher altitudes and greater distances than ever before, UAVs have expanded beyond their initial military application [1]. They are now being used in a wide range of civil and commercial industries, from real-time traffic monitoring and wireless coverage to precision agriculture and civil infrastructure inspections [5].

Conventionally, the energy required to power all the electrical consumers on board a UAV is provided by a battery. The limitations of a flight mission are determined by the amount of energy stored or produced on board the aircraft prior to takeoff [2]. Increasing

the number of battery cells can extend the duration of electric power supply, but the added weight significantly limits the flight range.

A constructive solution to mitigate these operational limitations is the implementation of a photovoltaic system on the surfaces of the UAV. This way, solar radiation absorbed by the photovoltaic cells is converted into electric energy and transmitted to both consumers and the battery, enabling sustained flight throughout the day [6].

This paper outlines the way in which the energy system of a UAV, whose main energy source is photovoltaic cells, provides the necessary power for all consumers . In this regard, an analysis was conducted by simulating a long-term aerial monitoring mission lasting 24 hours. The numerical modeling presented was generated using the MATLAB/SIMULINK computational tool, in which the initial settings considered were the technical characteristics of the UAV developed in ing. Buzdugan Andrei's doctoral thesis [9].

2. THE MATHEMATICAL MODEL OF THE ENERGY MANAGEMENT SYSTEM

The theoretical developments made during this research are directly used in the development of the software integrated in the energy management unit. Therefore, on-board the UAV, the supply of electrical consumers is controlled through the energy management system. The C++ code was developed based on (1)-(8) and (9)-(14), and was implemented in the PIC microcontroller using the mikroC PRO for PIC application [10]. The resulting files were loaded onto the PIC16F887 microcontroller using a PICKit 3 programmer [8].

$$\frac{d_v}{d_t} = \frac{T\cos\alpha}{m} - \frac{D}{m} - g \cdot \sin\gamma \tag{1}$$

$$\frac{d_\gamma}{d_t} = \frac{T\sin\alpha}{mv} + \frac{L}{mv} \cdot \cos\psi - \frac{g}{v} \cdot \cos\gamma \tag{2}$$

$$\frac{d_\varphi}{d_t} = \frac{L}{m \cdot v\cos\gamma} \cdot \sin\psi \tag{3}$$

$$\frac{d_x}{d_t} = v \cdot \cos\gamma \cdot \cos\varphi \tag{4}$$

$$\frac{d_y}{d_t} = v \cdot \cos\gamma \cdot \sin\varphi \tag{5}$$

$$\frac{d_h}{d_t} = v \cdot \sin\gamma \tag{6}$$

$$L = \frac{1}{2} \cdot \rho \cdot v^2 \tag{7}$$

$$D = \frac{1}{2} \rho \cdot v^2 \cdot S_w \cdot C_D \tag{8}$$

in which:

- x, y and h represent the position of the UAV (N, E and height), relative to the terrestrial axis system;
- v - speed of the UAV;
- m - total mass of the UAV;
- g - gravitational acceleration;
- angles: Ψ - roll angle, φ - yaw angle and γ - pitch angle;
- forces: T - traction force, L - lift force and D - drag force.

In (7) and (8) Sw is the area of the wings, CD and CL are the drag and lift coefficients, and ρ is the air density coefficient.

The solar radiation for a terrestrial system, marked by P_s and expressed in W/m^2, is calculated using (9).

$$P_s = I_{SC} \cdot \tau \cdot \sin(H_s) \tag{9}$$

in which:

- I_{SC} - current intensity generated by photovoltaic cells;
- τ -transmission factor.

A detailed form of solar radiation is obtained by describing the intensity of the current generated by the photovoltaic cells and the elevation angle of the sun in the form of (10) and (11).

$$I_{SC} = I_0 \cdot \left(\frac{1 + \varepsilon \cdot \cos(2\pi(n-4)/365}{1-\varepsilon^2}\right)^2 \tag{10}$$

$$\sin(H_s) = \sin\phi \cdot \sin\delta + \cos\phi \cdot \cos\delta \cdot \cos(\pi - \pi \cdot t/12) \tag{11}$$

In (10) and (11) the following notations were used:

- I_0 - constant value of solar radiation (1367W/m^2);
- ε - represents the earth's eccentricity ratio (≈0.01671);
- n - represents the number of the day of the year;
- ϕ- represents the latitude of a location;
- t - solar time of a location;
- δ- the declination angle of the sun.

A first step in this process consists in representing the solar radiation P_s in all three directions IXb, IYb and IZb, in the positive and negative sense. Depending on the azimuth angle and the elevation angle of the sun, the intensity of solar radiation in the three directions is represented in the form of (12), (13) and (14).

$$I_{Xg} = P_S \cdot \cos H_s \cdot \cos A_s \tag{12}$$

$$I_{Yg} = P_S \cdot \cos H_s \cdot \sin A_s \tag{13}$$

$$I_{Xg} = P_S \cdot \cos H_s \cdot \cos A_s \tag{14}$$

3. EXPERIMENTAL DETERMINATIONS

To corroborate the accuracy of the mathematical model of the energy management system, a sequence of experiments were conducted on an electric-powered UAV using photovoltaic cells. To ensure comparable operational circumstances throughout various flight phases, a parameter-recording test rig was utilized.

The examination of the data obtained from ten samples collected during the experiment facilitates the identification of an approach to optimize and streamline the energy system of a solar-powered UAV utilized for aerial surveillance missions. As depicted in Fig. 1, the configuration comprising the UAV, the testing platform, and the evaluation apparatus is presented.

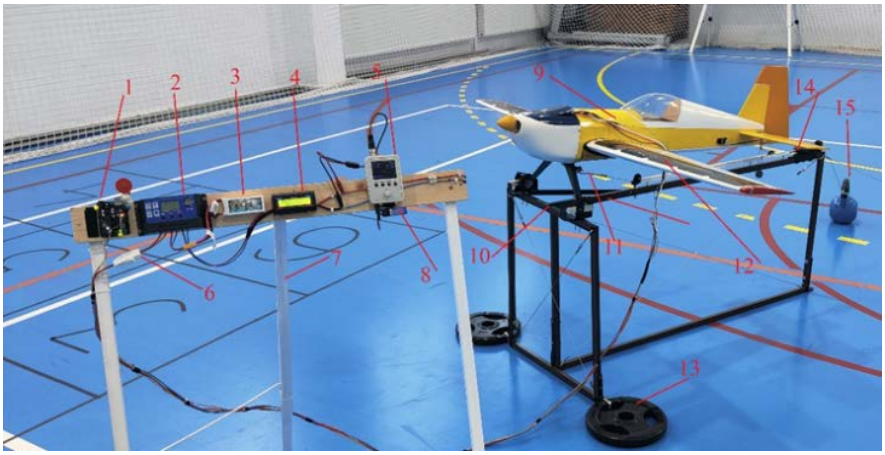

FIG. 1 The experimental setup for determining the functional parameters of a solar UAV

The main components used in the experiment are numbered from 1 to 15 and represent the following:

1 – Ardnuio UNO R3 [7]; **2** – MPPT device with microcontroller PIC16F887 [8]; **3** – battery pack; **4** – device for measuring the consumed power; **5** – oscilloscope; **6** – electrical circuit switch photovoltaic system; **7** – test bench; **8** – battery power oscilloscope; **9** – UAV; **10** – stand for testing UAV; **11** – thrust thrust; **12** – photovoltaic cells; **13** – holding weight in fixed position; **14** – traction force measuring device; **15** – anchor weight.

During the experimental testing of the UAV on the designated test stand, a simulated aerial monitoring mission was conducted, during which ten measurements were taken to determine the performance characteristics of the propulsion system and energy consumption. For each level of rotation speed, varying values of current intensity and voltage were recorded using a power measurement device. The measurement of the traction force of the UAV entailed the monitoring of propeller speed and weight exerted on the digital scale. Upon the completion of the experiment illustrated in Fig. 1, an array of parameters was acquired, providing a comprehensive depiction of the energy system's operation. These data are presented in Table 1.

Table 1. Experimental parameters determined during UAV testing on the stand

Sample no.	RPM	I	V	Thrust (g)
1.	1293	0.22	11.29	71
2.	2253	0.49	11.28	110
3.	3278	1.13	11.26	165
4.	3925	2.03	11.23	212
5.	4569	3.24	11.19	405
6.	5459	5.67	11.12	518
7.	5924	7.23	11.05	590
8.	6364	9.3	10.97	620
9.	6912	11.95	10.88	1018
10.	7204	13.81	10.82	1210

Upon examination of the data provided in Table 1, several key findings have been uncovered. Firstly, it has been determined that the voltage supplied to consumers remains constant throughout the entirety of the operation. Additionally, it has been observed that the electric current intensity and thrust force increase simultaneously with the propeller speed.

Based on the aforementioned findings, the graph displayed in Fig. 2 has been created to demonstrate the relationship between power consumption and electric motor speed. As the propulsion system speed increases, there is a concurrent increase in traction force.

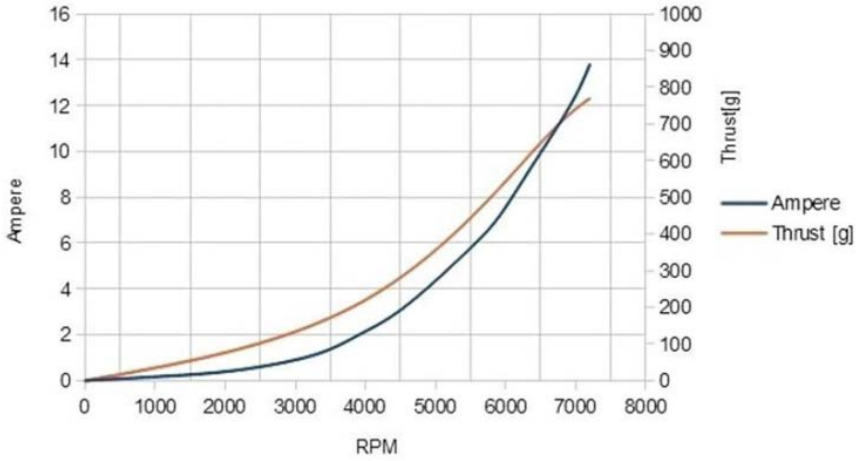

FIG. 2 The graphical representation of the experimentally obtained parameters in the testing phase

The obtained experimental data play a pivotal role in commencing the numerical modeling stage, wherein the operation of the energy system and its efficacy in furnishing power to electrical consumers to fulfill the mission objectives are scrutinized.

4. NUMERICAL MODELING OF THE ENERGY MANAGEMENT SYSTEM

The numerical model, formulated based on equations (1)-(14), proves to be versatile, enabling its use in both constant altitude flight missions and those with variable ceilings across different stages. In order to generate a set of reference data for the actual operation of the UAV, the MATLAB computational tool [9] was used. Two distinct scenarios were considered, corresponding to the UAV's power supply being furnished by varying numbers of electrical sources. Subsequent simulations were conducted, focused on a 24-hour flight mission profile, whose stages are illustrated in the schematic presented in Fig. 3.

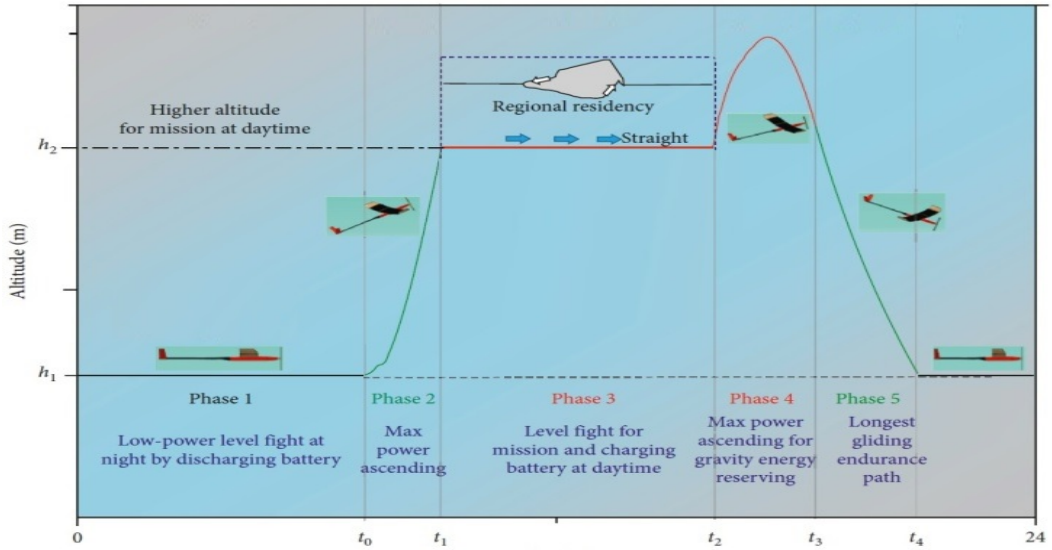

FIG. 3 Flight diagram for a UAV powered through photovoltaic cells

The difference between the two cases represents the number of electrical sources used to power the consumers. The selected options are:

- Photovoltaic cells, battery pack, and fuel cell;
- Photovoltaic cells and battery pack.

The numerical model was implemented in the MATLAB application, which has been widely used for various terrestrial or aerial simulations. The source code is a personal contribution and not a commercially purchased product.

Thus, there is the possibility of modification/adaptation for different types of photovoltaic-powered UAV's. The program is not limited to a restricted set of cases as is the case with many commercial programs.

4.1. Case 1 (photovoltaic cells and battery pack)

The solar UAV performs an aerial monitoring mission, in which the electrical consumers are powered by a battery and a photovoltaic system.

Flight mission data:

- Maximum flight altitude: 3000 m;
- Aerial monitoring altitude: 2100 m;
- Cruise altitude: 1600 m;
- Time period: 24h - July 15, 2022;
- Flight stages: 5;
- Weather conditions: normal for this period (clear sky);
- Solar radiation interval: 06:17-19:50.

Technical data on the UAV:

- Maximum power generated by the photovoltaic system: 180 W;
- Maximum power generated by the battery: 200 W.

Drawing on its own management system's numerical model, the solar UAV reached a maximum altitude of 3000 m, as shown in Fig. 4. During the ascent, the electrical consumers were supplied with power from the two energy sources in a differentiated manner determined by the calculation algorithm.

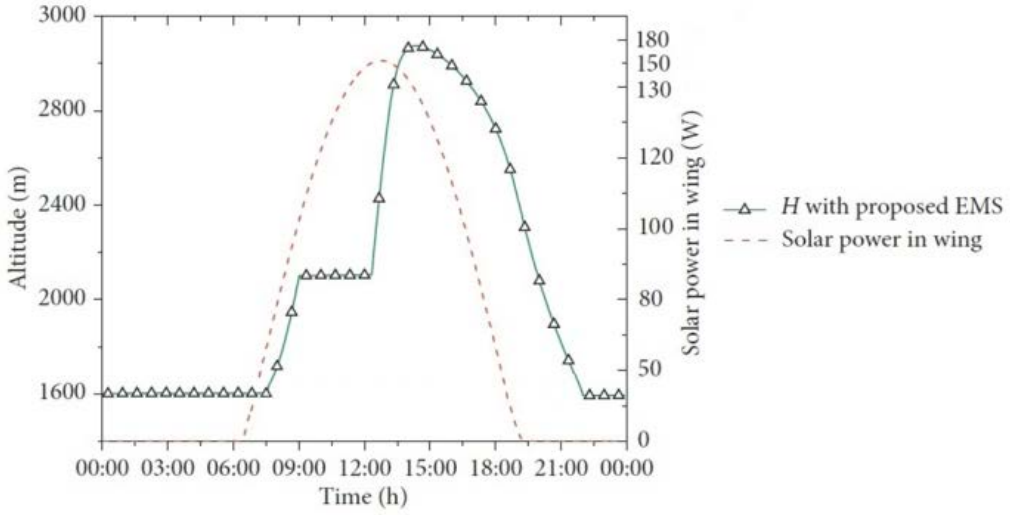

FIG. 4 Determination of the maximum flight altitude in the case of using only two energy sources

The graph depicted in Fig. 4 reveals a clear correlation between the performance of the photovoltaic system and the ascending flight of the UAV. As the sun rises and the photovoltaic cells start generating electricity, the propulsion system experiences an additional power consumption.

However, the energy required to power the system is simultaneously supplied by the two energy sources. The photovoltaic system needs to generate a maximum of 56 W while the ascending flight to a height of 2930 m requires 180 W.

The energy management system ensures the power difference by utilizing the accumulator battery. Throughout this time interval, the energy transfer to the consumers is maintained by both electrical sources.

4.2. Case 2 (photovoltaic cells, battery pack, and fuel cell)

The flight mission in the second case is conducted under the same conditions as in the first scenario, with the exception that the electrical consumers are powered by three energy sources: a photovoltaic system, an accumulator battery, and a fuel cell with a total power generation capacity of 120 W.

Moreover, Fig. 5 displays a constant power output by the fuel cell during the entire operation period. The accumulator battery supplies power to the electric consumers between 00:00-01:30, after which the fuel cell takes over to assist with energy transfer until the photovoltaic system is able to provide the required power.

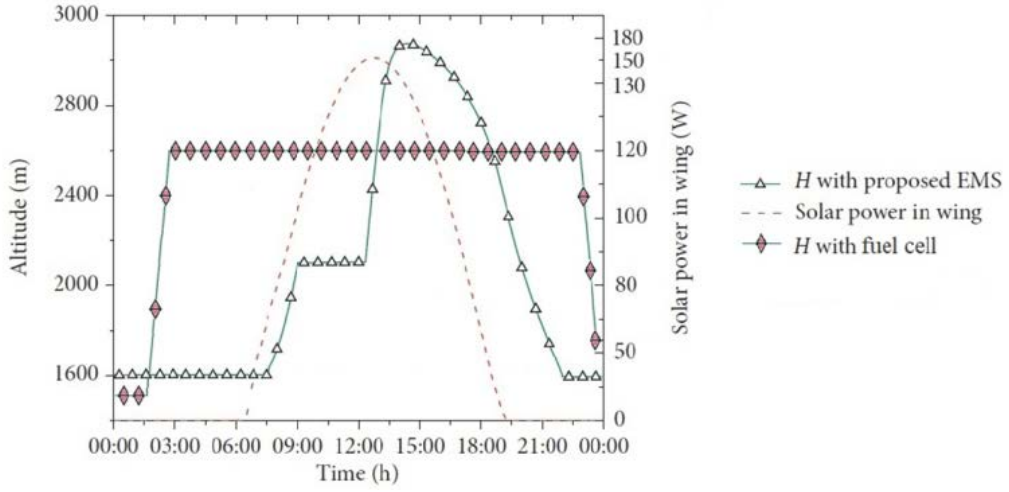

FIG. 5 Graphical representation of the power supply system using three electrical sources

The graph presented in Fig. 5 demonstrates that the fuel cell operates steadily at maximum capacity, and the following observations can be made:

- the fuel cell provides 75 % of the power required by the propulsion system.
- over the entire flight mission, the fuel cell generates 93.75 % of the total electrical energy.

By analyzing the graphs in Fig. 4 and 5, it is clear that using three electrical sources leads to a high efficiency in powering the electric consumers.

The importance of incorporating a fuel cell into the power system is particularly evident when the solar radiation is low and cannot provide sufficient power for the propulsion system. In this scenario, the accumulator battery may become depleted after prolonged use.

CONCLUSIONS

In order to achieve a solar UAV capable of high-altitude and long-distance missions, it is necessary to power the electrical consumers through multiple energy sources. An energy management system, such as the active command system (APM), can switch between energy sources to ensure a constant power supply to the electrical consumers

throughout the flight duration. By combining photovoltaic cells with a battery and a fuel cell, the UAV can be powered for longer periods of time and at various times of the day. The power supply is provided in a mixed or individual mode from the three sources depending on flight conditions and propulsion system requirements.

A proposed technical solution involves developing an energy management system with an integrated MPPT function that selects the optimal energy source and supplies all electrical consumers in the most efficient way possible. The mathematical algorithm takes into account solar radiation levels, battery charging capacity, and fuel cell status to determine the best energy source for powering the consumers. Energy source switching is controlled by the algorithm to ensure uninterrupted and efficient power supply.

During the flight mission, energy consumption and battery charging vary depending on the altitude and propulsion system requirements. Flying at a constant altitude involves a uniform power consumption, with energy generated by the photovoltaic system used to power the electrical consumers and charge the battery. If the UAV maintains a constant flight altitude below 2000 m and the maximum power consumption of the propulsion system does not exceed 50 W under normal solar radiation conditions, then the propulsion system can be powered exclusively by energy generated by the photovoltaic cells.

During the ascent, all the power generated by the photovoltaic system is transmitted to the propulsion system without charging the battery. During the descent, energy consumption is minimal and the power generated by the photovoltaic system is used to power the electrical consumers and charge the battery.

REFERENCES

[1] P. Arjyadhara, S.M. Ali, J. Chitralekha (2013), *Analysis of solar PV cell performance with changing irradiance and temperature*, International Journal of Engineering and Computer Science 2(1):214-220;

[2] G. Abbe, H. Smith (2016) *Technological development trends in solar-powered aircraft systems*, Renewable and Sustainable Energy Reviews 60:770-783. https://doi.org/10.1016/ j.rser.2016.01.053;

[3] R. Barbosa, B. Escobar, V.M. Sanchez, J. Hernandez, R. Acosta, Y. Verde, (2014), *Sizing of a solar/ hydrogen system for high altitude long endurance aircraft*, International Journal of Hydrogen Energy 39(29):16637-16645. **Error! Hyperlink reference not valid.**;

[4] D. Glade (2019), *Unmanned Aerial Vehicles: Implications for Military Operations, Occasional Paper No. 16 Center for Strategy and Technology Air War College Air University Maxwell Air Force Base*;

[5] J. Sliwinski, A. Gardi, M. Marino, R. Sabatini (2017), *Hybrid-electric propulsion integration in unmanned aircraft*, Energy 140:1404-1416. https://doi.org/10.1016/j.energy.2017.05.183;

[6] V.V. Tyagi, N.A.A. Rahim, N.A. Rahim, J.A.L. Selvaraj (2013), *Progress in solar PV technology: research and achievement*, Renewable and Sustainable Energy Reviews 20:443-461. https://doi.org/10.1016/j.rser.2012.09.028;

[7] https://docs.arduino.cc/resources/datasheets/A000066-datasheet.pdf;

[8] https://ww1.microchip.com/downloads/en/DeviceDoc/ 51795B.pdf;

[9] https://www.mathworks.com/products/matlab.html?s_tid= hp_products_matlab;

[10]https://www.mikroe.com/mikroc-pic.

POWER SOURCES SWITCHING IN A HYBRID ENERGY NETWORK ON BOARD A SOLAR UAV

Andrei BUZDUGAN
Military Technical Academy Ferdinand I (andrei_buzdu@yahoo.com)
ORCID: 0000-0001-6004-3115

Nicolae JULA
Military Technical Academy Ferdinand I (nicolae.jula@gmail.com)

Albert BĂLTEANU
"Henri Coandă" Air Force Academy, Brașov, Romania (albert_balteanu@yahoo.com)

DOI: 10.19062/1842-9238.2022.20.2.7

Abstract: *Utilizing a photovoltaic system to power an Unmanned Aerial Vehicle (UAV) enables longer and extended flights. A hybrid energy system, consisting of three distinct energy sources, was investigated. A technical solution was developed to optimize the energy system and mitigate transient effects observed during power source switching. Through a long-term aerial monitoring mission simulation, the study demonstrated the efficiency and reliability of the energetic management system for a solar-powered UAV in providing a constant and stable power supply to the grid throughout the flight. The findings of this study have implications for the development of high-performance UAVs by ensuring optimal and efficient selection of suitable energy sources for flight conditions and uninterrupted power supply to electrical consumers, minimizing operational risks.*

Keywords: *energetic management system, commutation, photovoltaic cells, fuel cell, battery, UAV*

1. INTRODUCTION

Conventionally, the energy required to power all the electrical consumers on board a UAV is provided through an accumulator battery. The limitations of a flight mission are determined by the amount of energy stored or produced on board the aircraft prior to takeoff. Increasing the number of battery cells extends the duration of the electric power supply, but due to the additional weight, the flight range is not significantly increased.

A structural solution to mitigate these operational limitations involves the implementation of a photovoltaic system on the lifting surfaces of the UAV. This way, solar radiation on the photovoltaic cells is converted into electrical energy and transmitted to the consumers and battery, allowing for continuous flight throughout the day.

In terms of complexity, powering a UAV with solar energy also involves the use of other auxiliary energy sources and components. Following an analysis of the main elements used in the construction of a solar-powered UAV, two of them are of particular importance: the photovoltaic cells and the maximum power point tracking (MPPT) device

[14], [12], [7]. The connection between these two elements lies in the optimization of the entire photovoltaic system's performance.

When exposed to solar radiation, an electric current is registered at the terminals of a photovoltaic cell. The relationship between the level of solar radiation and the energy generated by the photovoltaic cells is graphically described through an intensity-voltage curve. Depending on the type of photovoltaic cell, the I-V curve's shape differs from case to case [6].

2. HYBRID ENERGY SYSTEM

Based on the statements from introduction, the capacity of a battery to generate the required power for certain flight missions is limited. Furthermore, the charging time is longer than the time to power the consumers, and landing the UAV and connecting it to a power source is required for recharge.

For this reason, the development of a hybrid energy system, consisting of photovoltaic cells, a fuel cell, and a battery, represents a technical solution to improve the flight time of a solar-powered UAV. In this sense, researchers from the Aerospace Research Institute of South Korea and the National Institute of Aerospace Technology of Spain validated the premise of the outstanding results of a hybrid energy system by performing checks and simulations in the Matlab/Simulink application [3], [13].

In this configuration, the photovoltaic cells integrated on the carrying surfaces of a UAV provide the necessary energy to the consumers during the day, charge the battery, and perform the electrochemical process of the fuel cell. In the case of low solar radiation, when the photovoltaic cells are not functioning at nominal capacity or not generating energy, the fuel cell entirely supplies the electric consumers.

The block diagram presented in Fig. 1 represents the electrical circuit of a hybrid energy system, in which the primary energy source is the photovoltaic system, and the secondary sources are the fuel cell and the battery. The integration of unidirectional or bidirectional converters ensures the flow of energy depending on the direction and time of the power source. In this sense, the direct current generated by the photovoltaic cells is converted into alternating current to power the propulsion system and other electric consumers. The fuel cell and the battery are electric sources for which the energy transfer flow is carried out in both directions, and the type of current differs depending on the case. Bidirectional converters are used to achieve energy transfer and conversion from direct current to alternating current and vice versa. The connection of an MPPT device ensures the photovoltaic system operates at maximum capacity by continuously detecting the maximum value of solar radiation.

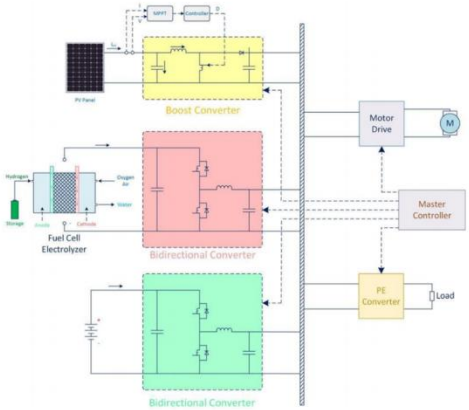

FIG. 1 Block diagram of the hybrid power network for a UAV powered by photovoltaic cells

During the night, the energy generated by the fuel cell is only distributed to the electrical consumers, without charging the battery. A high level of solar radiation allows the photovoltaic system to generate enough energy to power the electrical consumers and charge the battery. Under certain conditions, when additional power is required for the propulsion system and the photovoltaic system is in operation, some of the generated energy is transferred to the fuel cell. Control of the energy flow and priorities for energy transfer is ensured through the energy consumption management system. Depending on the type, weather conditions, and flight mission duration, the command and control unit sets the priorities for electrical power supply.

From the advantages presented above, hybridization represents the most suitable architecture for powering the electrical consumers of a solar UAV. The implementation of a power control strategy at the command unit level ensures outstanding energy system performance through optimal switching of energy sources based on flight conditions and UAV power consumption [1], [8]. When more than two electrical sources are used in the power system, they can be connected in series, parallel, or mixed, depending on their priority in powering the consumers [9], [2].

Series connection of electrical sources is used for UAVs that fly at low altitude and require high power consumption. Most UAVs designed for civilian or military purposes use a parallel connection of energy sources. This configuration benefits from redundancy, but in certain situations, power control becomes difficult when the power supply is simulated through two or more energy sources [11].

Mixed connection of energy sources requires a minimum of three electric sources. From a technical point of view, it presents all the advantages of the two types of connections presented earlier, but manufacturing costs due to complexity are high [10].

3. ENERGY MANAGEMENT UNIT FOR A SOLAR UAV

The energy management unit, based on a mathematical algorithm implemented as a C++ program, ensures continuous power supply to electrical consumers and efficiently switches between energy sources. The main functions of the management algorithm include quickly identifying the maximum power generated by the photovoltaic system, selecting the optimal energy sources, and controlled charging of the battery pack [5], [16].

Photovoltaic cells generate electrical energy only during the day and under certain lighting conditions. Therefore, secondary energy sources are necessary. A technical solution for creating a mixed secondary energy source is to use a battery pack and a fuel cell. From this perspective, supplying consumers through a battery pack requires a charging and discharging control system that ensures its normal operation and significantly prolongs its service life. By using a DC converter, consisting of a capacitive filter and a multi-winding transformer, controlled and optimized charging of a battery is achieved [3].

The practical realization of an energy management unit for a solar-powered UAV contributes to research on the switching mode of power sources and the study of transient effects during power supply to electrical consumers. After analyzing the international standard ISO 10483-1:2004, which specifies the optimal criteria for energy source switching, the main characteristics for designing the electrical scheme of the energy management unit were determined [17].

After establishing the main elements required in the design process, the electrical scheme and 3D simulations of the energy management unit were created using the Proteus PCB Design software. The electrical scheme of the energy management unit for a UAV powered by photovoltaic cells is shown in Fig. 2.

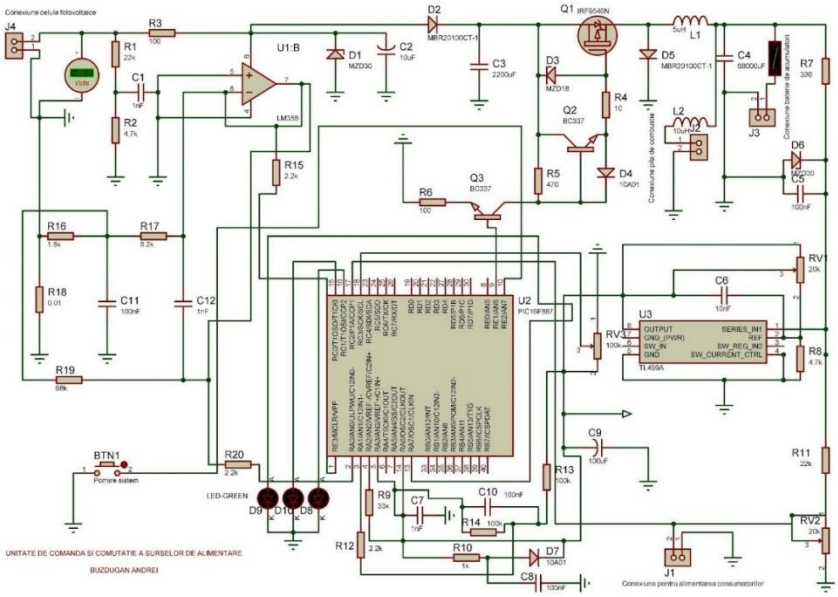

FIG. 2 The electrical diagram of the energy management system unit

Through the two operational amplifiers of the LM358 integrated circuit, the voltage and electric current generated by the photovoltaic cells are measured [18]. The information received from the integrated circuit is processed by the PIC16F887 microcontroller, resulting in an amplitude-modulated signal that is later used in the step-down conversion stage of the electric current [19].

The P-channel MOSFET transistor Q1 is switched in accordance with the signal emitted from pin 9 of the PIC microcontroller. Throughout the operation, transistors Q2 and Q3 ensure the integrity of the amplitude-modulated signal.

The electrical diagram presented in Fig. 2 has the advantage of obtaining a maximum voltage of 12V and a current of up to 3A. The battery charging procedure is gradually carried out in three levels, depending on the solar radiation and electric current generated by the photovoltaic system. During the operation of the fuel cell to supply consumers, the battery is not charged. This method ensures a long battery life and constant discharge during operation.

The TL499A integrated circuit provides a stable and constant voltage of 5V necessary for the operation of the PIC microcontroller.

Depending on the solar radiation level, battery charging capacity, and fuel cell status, the energy management unit selects the optimal power source for supplying consumers without interrupting, limiting, or reducing the supplied electric energy. Throughout this time, the energy source switching is controlled by a mathematical algorithm integrated in the form of a C++ program in the PIC16F887 microcontroller.

After functional testing in the Proteus PCB Design application, the electrical diagram presented in Fig. 2 was exported to the ARES application to simulate a 3D presentation of the energy management system [20]. The dimensions of the electronic board presented in Fig. 3 are 97 mm in length and 48 mm in width.

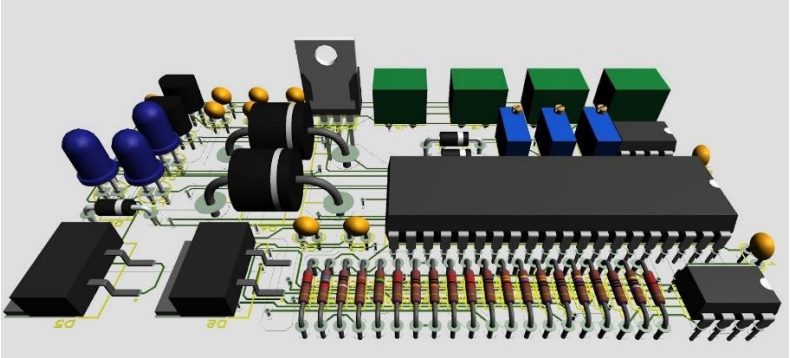

FIG. 3 3D simulation of the electronic board for the energy management system

4. THE EXPERIMENT

In order to validate the experimental model of the energy management system, a series of tests were carried out using an UAV powered by electric energy generated by photovoltaic cells. To obtain similar operating conditions for different flight stages, a test stand with the ability to record parameters was used. Similar tests were carried out in the Solar Flight company laboratories in Italy, which resulted in data regarding the optimization and operation of the energy system for the following UAVs: Solar-Seat Transporter, SunStar, and Sunseeker I and II [15], [21].

The results of the tests presented in this paper were obtained in the on-board Equipment Maintenance Laboratory at Bacau Air Base 95.

The practical realization of a UAV with a wingspan of 151 cm and a test stand for operating regimes made it possible to validate the energy management system by providing a constant and uninterrupted power supply to electric consumers and studying the transient effects observed during the switching of energy sources. The electrical sources used in this case represent a photovoltaic system composed of 10 solar cells, an accumulator battery and a fuel cell [4].

During the experiment, certain aspects were monitored regarding the power ratio generated by the three electrical sources and the power consumed by the propulsion system, as well as the transient effects of the electric current observed during the switching of the power supply mode.

The image presented as Fig. 4 illustrates the solar-powered UAV utilized for conducting functional tests, showcasing its physical design, configuration, and key components.

- 10 X SunPower C60 solar cells (125 x 125 mm) made of monocrystalline silicon, connected in series, with 5.8A, and the total power of 65W

- TurnigyAerodrive D3548/4 1100 KV electric motor

FIG. 4 UAV powered by solar energy used in the experiment

The research conducted in this experiment aimed to observe the transient effects of electric current during the switching of power sources, and the resulting study presents the findings.

The transient effects of electric current occur when the power source changes suddenly or when the electric current is interrupted. These variations in electric current can cause damage or operational limitations to the electric and electronic systems within the power grid, leading to unexpected behavior or deterioration of these systems.

To minimize the transient effects of electric current, various techniques and devices can be used, such as EMI filters and slow-switching breakers. These help attenuate rapid variations in current or voltage, thereby reducing the risk of damage to connected systems and devices.

The switching of electrical sources is carried out under the following conditions:

- the voltage generated by the photovoltaic system drops below 12V;
- the power generated by the photovoltaic system does not fully meet the energy needs of the UAV.

Based on these criteria and the number of electrical sources connected to the MPPT device, the experiment was repeated twice. The data recorded using a Tektronix TDS 220 laboratory oscilloscope, connected to the power supply network of the electrical consumers, are the results of a comparison between the two situations [22].

Depending on the number of power sources connected to the energy system, two cases were obtained, and presented in Fig. 5 A and B:

- Fig. 5 A / case 1 - photovoltaic cells, battery pack, and fuel cell;
- Fig. 5 B / case 2 - photovoltaic cells and battery pack.

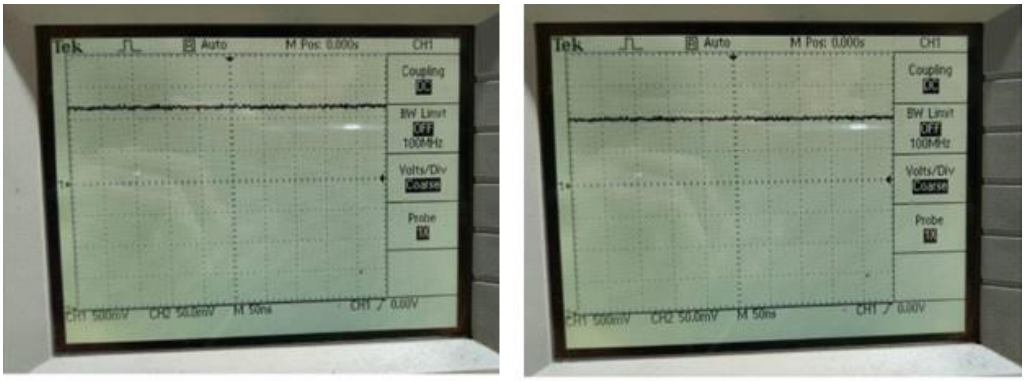

FIG. 5 The experimental results of energy source switching in both cases

Case 1 - Fig. 5 A:

Under normal illumination conditions, the photovoltaic system operates at its maximum capacity, and the voltage generated by it has a value of 12.5V. The battery connected to the MPPT device indicates a voltage of 12.4V, comparable to that of the photovoltaic system.

After initiating the energy system, the electric motor was accelerated to a speed of 4569 rpm. For this operating regime, the entire energy consumption is provided through the photovoltaic cells. The power resulting from solar energy has a value of 65W, and the power required for the propulsion system at this speed is 36.25W.

To study the transient effects that occur during the switching of electrical sources, the conditions were simulated where the UAV flies a distance during the night when the solar

radiation intensity is undetectable. In this regard, the power supply from the photovoltaic cells was interrupted through a switch mounted on the main power supply line.

On the oscilloscope screen shown in Fig. 5 A, a constant supply voltage and current can be observed, even during the switching of power sources. The frequency of display of signal changes is 50 ns, and the voltage oscillation detection mode is selected to be automatic.

During the period when the consumers were being supplied by the three electrical sources, five successive switches were performed. During these tests, the supply voltage value to the consumers remained constant, and no oscillations were recorded on the oscilloscope screen during the switching of power sources. The reason why there were no non-conformities recorded throughout this verification period is due to the fact that the total power generated by the three sources is greater than that required for normal operation.

Case 2 - Fig. 5 B:

To validate the premise resulting from Case 1, the experiment was repeated by disconnecting the fuel cell from the energy supply system. With the energy generated by the photovoltaic system, the electric motor was accelerated to the same speed of 4569 rpm, consuming 36.25W. After activating the switch that disconnects the power supply from the photovoltaic cells, the MPPT time device automatically transfers energy through the battery. Following this action, a sudden reduction in the current supplied to electrical consumers was observed on the oscilloscope screen, as depicted in Fig. 5 B.

Comparing the results obtained in Case 1 and Case 2, the following conclusions have been drawn:

- the MPPT device performs the switching of power sources under the initially imposed conditions;
- in the case of a complete interruption of the energy flow generated by the photovoltaic system, when only the photovoltaic cells and the battery are connected to the MPPT device, the supply current value drops;
- under certain conditions, when electronic devices and the propulsion system require a standard current and electrical voltage value, there is a risk of them shutting down.

CONCLUSIONS

To be able to perform long-distance and high-altitude flight missions, a UAV needs to be powered by multiple energy sources. In a hybrid energy network, where photovoltaic cells are the main source, the use of an energy management system can ensure a constant supply of electricity to consumers throughout the entire operation.

After comparing the characteristics of energy management systems used in solar UAVs, the active command system (APM) was found to be the most suitable for powering consumers by switching energy sources.

The use of photovoltaic cells together with a battery and a fuel cell ensures in-flight power supply for the UAV at different times of the day and for extended periods. Depending on the flight conditions and power requirements, the power supply can be provided in a mixed mode from all three sources or individually.

To ensure efficient selection of energy sources and supply all electric consumers in the most efficient way possible, a proposed technical solution involves developing and experimentally implementing a control unit with integrated MPPT function. This will select the optimal power supply source based on solar radiation levels, battery charging capacity, and fuel cell condition. The switching of energy sources will be controlled by a mathematical algorithm.

REFERENCES

[1] A.K. Sehra, W. Whitlow, Prog. Aerosp. Sci., 40 (2004) 199–235;
[2] B.A. Moffitt, T.H. Bradley, D. Mavris, D.E. Parekh, Collect. Tech. Pap. - 6th AIAA Aviat. Technol. Integr. Oper. Conf., 1 (2006) 14–29;
[3] B. Lee, P. Park, C. Kim, S. Yang, S. Ahn, J. Mech. Sci. Technol., 26 (2012) 2291–2299;
[4] D. Glade (2019) , U*nmanned Aerial Vehicles: Implications for Military Operations, Occasional Paper No. 16 Center for Strategy and Technology Air War College Air University Maxwell Air Force Base*;
[5] E. Bongermino, F. Mastrorocco, M. Tomaselli, V.G. Monopoli, D. Naso, IEEE Int. Symp. Ind;
[6] K.A. Emery, *Photovoltaic efficiency measurements—Overview. In Proceedings of the SPIE*, The International Society for Optical Engineering, Denver, CO, USA, 3 November 2002;
[7] A. Guo, Z. Zhou, X. Zhu, X. Zhao, Y. Ding, *Automatic Control and Model Verification for a Small Aileron-Less Hand-Launched Solar*, Powered Unmanned Aerial Vehicle. Electronics 2020, 9, 364;
[8] H. Chen, A. Khaligh, IECON Proc. (Industrial Electron. Conf., Glendale, USA (2010) 2851–2856;
[9] J.Y. Hung, L.F. Gonzalez, Prog. Aerosp. Sci., 51 (2012) 1–17;
[10] M. Abdul Sathar Eqbal, N. Fernando, M. Marino, G. Wild, Aerospace, 5 (2018) 34;
[11] M. Harmats, D. Weihst, J. Aircr., 36 (1999) 321-331;
[12] S. Morton, R. D'Sa, N. Papanikolopoulos, *Solar Powered UAV: Design and Experiments*, In Proceedings of the IEEE/RSJ International Conference on Intelligent Robots and Systems (IROS), Hamburg, Germany, 28 September–3 October 2015;
[13] Ó. González-Espasandín, T.J. Leo, E. Navarro-arévalo, Sci. World J. 2014 (2014) 1-14;
[14] P. Oettershagen, A. Melzer, T. Mantel, K. Rudin, T. Stastny, B. Wawrzacz, T. Hinzmann, S. Leutenegger, K. Alexis, R. Siegwart, *Design of small hand-launched solar-powered UAVs: From concept study to amulti-dayworld endurance record flight*.J. Field Robot. 2017, 34, 1352–1377;
[15] L. Wagner (2007), *Overview of Energy Storage Methods*, Mora Associates Research Report;
[16] Y. Xie, A. Savvaris, A. Tsourdos, Aerosp. Sci. Technol., 85 (2019) 13–23;
[17] https://www.iso.org/standard/36423.html;
[18] https://datasheetspdf.com/pdf/603853/ONSemiconductor/LM358/1;
[19] http://ww1.microchip.com/downloads/en/devicedoc/41291d.pdf;
[20] https://www.labcenter.com/schematic/;
[21] https://www.solar-flight.com/projects.;
[22] https://www.testequipmenthq.com/datasheets/ TEKT-RONIX-TDS220-Datasheet.pdf.

SOLVING THE BILEVEL LINEAR PROGRAMMING PROBLEM USING THE MONTE CARLO METHOD

Ștefania CONSTANTINESCU, Ion MIERLUȘ-MAZILU
Technical University of Civil Engineering of Bucharest, Bucharest, Romania
(stefania.constantinescu@utcb.ro, ion.mierlusmazilu@utcb.ro)

DOI: 10.19062/1842-9238.2022.20.2.8

Abstract: *In this paper we propose to use the "Monte Carlo" method for solving bilevel linear programming (the bilevel linear programming problem – BLP problem). In the BLP problem, each decision maker tries to optimize their own objective function without considering the objective of the other party, but the decision of each party affects the objective value of the other party as the decision space. The existing methods for solving the BLP problem can be grouped into four categories: a) methods based on vertices enumeration; b) methods based on Kuhn-Tuck conditions; c) the fuzzy approach; d) metaheuristics methods. Starting from Gnedenko's theorem, this paper uses the "Monte Carlo" method to determine an approximate solution for the BLP problem. The numerical example presents the performance of the proposed approach.*

Keywords: *vertices enumeration method, decision makers, random search method, uniform random numbers, relative error*

1. BILEVEL LINEAR PROGRAMMING PROBLEM FORMULATION

The bilevel programming problem has its origins in the work of Stackelberg „The Theory of the Market Economy (Oxford University Press", 1952). The BLP arises in paper of Bracken and McGill "Mathematical Programs with Optimization Problems in the Constraints" (Operations Research Vol. 21 No. 1, 1973) [1]. Although the origins of BLP problem are in the game theory, BLP problem has applications in many technical fields and to set an example in hydrology to efficient use of water resources [3].

Many references can be found in the report of Vicente and Calamai, Bilevel and Multilevel Programming: A Bibliography Review [8].

The general formulation of a bilevel programming problem is as follows [2]:

(upper level)

$$\begin{cases} \min\limits_{x,y} F(x,y) \\ s.t.\ G(x,y) \le 0 \end{cases} \tag{1}$$

where y can be solved from

(lower level)

$$\begin{cases} \min\limits_{y} f(x,y) \\ s.t.\ g(x,y) \le 0 \end{cases} \tag{2}$$

where $x \in R^{n_1}$, $y \in R^{n_2}$. The variables of problem (1) , $x \in R^{n_1}$ are considered upper level and $y \in R^{n_2}$ are the lower level variables. The upper level decision maker controls over vector x, and the lower level decision maker controls over vector y.

In the following we consider the particular case when the objective functions and the constraints are linear functions, obtaining the BLP problem.

In the BLP problem, each decision maker tries to optimize its own objective function without considering the objective of the other party, but the decision of each party affects the objective value of the other party as well as the decision space. The linear BLP problem is an optimization model formulated as follows:

$$\begin{cases} \min\limits_{x} F(x,y) = c_1 x + d_1 y \\ \min\limits_{y} f(x,y) = c_2 x + d_2 y \\ s.t. \quad A_1 x + A_2 y \le b, \\ \quad\quad x,\ y \ge 0 \end{cases} \tag{3}$$

where: $F(x,y)$ is the objective function of the leader and $f(x,y)$ is the objective function of the follower. Also, $x \in R^{n_1}$ is a vector controlled by leader and $y \in R^{n_2}$ is a vector by follower, $A_1 \in \mathcal{M}_{m,n_1}(R)$ is a $(m \times n_1)$ real matrix and $A_2 \in \mathcal{M}_{m,n_2}(R)$ is a $(m \times n_2)$ real matrix. Here $x \ge 0$ means $x_i \ge 0,\ i = \overline{1, n_1}$.

The leader decision is priority and the leader gets feedback from the follower. There are many methods to solve this kind of problems; the existing methods can be grouped into the following categories [4]:

(a) Methods based on vertices enumeration: the optimal solution should be in vertex points belonging in feasible space determined by constraints [2],

(b) Methods Based on Kuhn-Tucker conditions: the BLP problem becoming a one-level problem replacing the second level problem with complementary constraints [9]

(c) The fuzzy approach: the objective functions of the leader or the follower or both objective functions are considered like a memberships function [6], and

(d) Methods based on meta heuristics: to solve the BLP problem can be used genetic algorithm [4,5], algorithm based on simulated annealing etc.

Our proposed approach can be included in last category of methods to solve BLP problem.

2. THE PROPOSED METHOD: OPTIMIZATION USING RANDOM SEARCH

In this section we present methods of optimization based on *random search.* The problem is the following, $\min\limits_{x \in D} f(x)$, where $D \subset R^k$ is a $k-$dimensional set. There is a vast variety of professional literature based on properties of $f(x)$ or of D. Here we are interested in determining the point $x^* \in D$ such as $\min\limits_{x \in D} f(x) = f(x^*) = f^*$, i.e. x^* is a *global* minimum point. The global minimum point is selected from several local minimums.

The idea of *random search* is the following [7]:

Generate a large number N of random points $X_1, X_2, ..., X_N$, uniformly distributed in D (supposed to be a bounded set). Then calculate $f(X_i)$, $1 \le i \le n$ and take $f^*_{(N)} = f\left(X^*_{(N)}\right) = \min\limits_{1 \le i \le N} f(X_i)$.

A theorem of Gnedenko (1943) says that in some conditions (i.e. f is a continuous function), we have $\lim_{N\to\infty} f^*_{(N)} = f^*$, $\lim_{N\to\infty} X^*_{(N)} = x^*$. If the optimum solution $x^* \in T^* \subset D$, (T^* is a capture set containing the solution), then it is known that for a given risk ε, $0<\varepsilon<1$ there is a p such as [7]:

$$P\left(X_N \in T^*; \left\|X_N - x^*\right\| \geq \varepsilon\right) = p,$$

it is necessary to use

$$N > \left[\frac{\log\varepsilon}{\log(1-p)} + 1\right] = N^*, \tag{4}$$

the previous probability being calculated for the assumed distribution of X. As p is not known, one can use $p > 1-\varepsilon$. The following algorithm allows the approximation of $x^* \in D$.

The Randseach Algorithm

Step 0. Input: $N-$ number of points uniformly distributed on D used for determining optimum value of leader function, X^*

$M-$ number of points extracted from the N used for determining optimum value of follower function, Z^*

$K-$ number of points uniformly distributed on the segment $\left[X^*, Z^*\right]$

Initialize: $i \leftarrow 1;\ j \leftarrow 0;$

Step 1. While $i \leq N$ execute

generate $x \sim > \mathcal{U}(D)$

calculate $C_{i,1} = F(x)$

for $j = \overline{2, k+1}$ $C_{i,j} = x_{j-1}$

endfor

endwhile

Step 2. Sort C after the first column in C

for $j = \overline{2, k+1}$

$x^*_{1,j-1} = C_{1,j}$

endfor

Retain M lines of C in B

for $i = \overline{1, M}$ calculated

$B_{i,1} = f\left(C_{i,2}, C_{i,3}, ..., C_{i,k}\right)$

for $j = \overline{2, k+1}$ $B_{i,j} = x_{j-1}$

endfor

endfor

Sort B after the first column in B

for $j = \overline{2, k+1}$ $y^*_{1,j-1} = B_{1,j}$

endfor

for $i = \overline{1, K}$

Generate $x \sim > \mathcal{U}\left(\left[x^*, y^*\right]\right)$

Calculate $F(x)$, $f(x)$.

$S_{i,1} = F(x)$

$S_{i,k+2} = f(x)$

for $j = \overline{2, k+1}$ $\quad x^{**}_{i,j-1} = S_{i,j}$

endfor

endfor

Sort S after the first column in *S;*

Step 3. Delivre $F_{opt} = F(x^{**})$, $f_{opt} = f(x^{**})$, obtained in x^{**}

Stop!

Remark: The matrix *S* have on the first line and first column the optimum value for leader objective function, on the first line and last column the optimum value for follower objective function and on the interior columns of the first line, x^{**}, are the coordinates of approximate optimal point!

3. A NUMERICAL EXAMPLE

We will customize the algorithm proposed in the previous section for the case of *k*=3 and we will compare the solution obtained with the help of the polyhedron vertex enumeration method with the approximate solution obtained with the proposed method. At the end of the section we will determine the relative error and we will make the necessary considerations.

Consider the following problem:

$$\min_{(x,y)} F(x,y,z) = 3x + y + z$$

$$\min_{z} f(x,y,z) = 2x - y - 7z$$

$$\text{restrictions} \begin{cases} 2x - y + 2z \geq 3 \\ x - y + z \leq 1 \\ x - y + 2z \leq 2 \\ y - z \leq 1 \end{cases}$$

These planes define an $ABCD$ tetrahedron with the following vertices:

$A(1,1,1), B(2,1,0)\ C(1,3,2),\ D(2,2,1).$

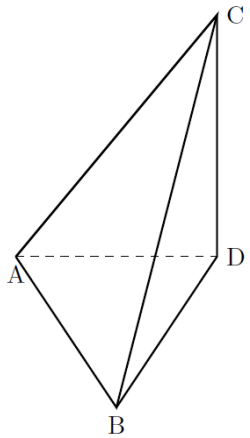

FIG. 1 Tetrahedron of restrictions

3.1 Enumeration Method

Firstly we use the enumeration vertices method to find exact solution.

$F(A)=F(1,1,1)=3\cdot 1+1+1=5$, $F(B)=F(2,1,0)=3\cdot 2+1+0=7$,

$F(C)=F(1,3,2)=3\cdot 1+3+2=8$, $F(D)=F(2,2,1)=3\cdot 2+2+1=9$,

$\min\limits_{t\in\{A,B,C,D\}}\{F(t)\}$ is obtained in the point *A*.

We have:

$$m=\max\left\{\frac{3}{2}-x+\frac{y}{2}, y-1, 0\right\}\le z\le \min\left\{1-x+y, 1-\frac{x}{2}+\frac{y}{2}\right\}=M$$

For that $[m, M]\neq\Phi$ it needs that $m\le M$, which is equivalent with the next inequalities

$$\frac{3}{2}-x+\frac{y}{2}<1-x+y\Rightarrow y\ge 1 \quad -x+\frac{y}{2}<1-x+y\Rightarrow y\ge 1 \tag{5}$$

$$\frac{3}{2}-x+\frac{y}{2}<1-\frac{x}{2}+\frac{y}{2}\Rightarrow x\ge 1 \tag{6}$$

$$y-1\le 1-x+y\Rightarrow x\le 2 \tag{7}$$

$$y-1\le 1-\frac{x}{2}+\frac{y}{2}\Rightarrow x+y\le 4 \tag{8}$$

$$0\le 1-x+y\Rightarrow x-y\le 1 \tag{9}$$

$$0\le 1+\frac{x}{2}+\frac{y}{2}\Rightarrow x-y\le 2 \tag{10}$$

The (10) relation is superfluous because it results from the relation (9). The (9) relation is superfluous because it results from the (5) and (7) relations. We can note that in the domain described by the above inequalities we obtain from the (5) relation, $y\text{-}1\ge 0$, so we can discard the zero from the description of *m*

$$1-x+y\le 1-\frac{x}{2}+\frac{y}{2}\Rightarrow y\le x$$

$$\frac{3}{2}-x+\frac{y}{2}\ge y-1$$

$$\frac{5}{2}\ge x+\frac{y}{2}$$

$$5\ge 2x+y$$

We have $z^*=M$ because *f* is decreasing in the variable *z*.

$z^*=M=1-x+y$ in the triangle with the vertices $A'(1,1)$, $B'(2,1)$, $D'(2,2)$

$F(x,y,z^*)=3x+y+1-x+y=2x+2y+1$

$(1,1)\to 2\cdot 1+2\cdot 1+1=5$

$(2,1)\to 2\cdot 2+2\cdot 1+1=7$

$(2,2)\to 2\cdot 2+2\cdot 2+1=9$

considering $A'(1,1)$, $B'(2,1)$, $D'(2,2)$, where A', B', D' are the projections of points, A', B', D' on the XOY plane.

$$F(x,y,z^*)=3x+y+1-\frac{x}{2}+\frac{y}{2}=\frac{5}{2}x+\frac{3}{2}y+1$$

$$(1,1)\to\frac{5}{2}\cdot 1+\frac{3}{2}\cdot 1+1=5$$

$$(1,3)\to\frac{5}{2}\cdot 1+\frac{3}{2}\cdot 3+1=8$$

$$(2,2)\to\frac{5}{2}\cdot 2+\frac{3}{2}\cdot 2+1=9$$

The optimum is obtained for $(x,y)=(1,1)$.

When $(x,y)=(1,1)$, $M=1-x+y=1$, $M=\frac{3}{2}-\frac{x}{2}+\frac{y}{2}=1$

When $(x,y)=(1,1)$, we have:

$$m=\max\left\{\frac{3}{2}-1+\frac{1}{2},1-1\right\}=1 \text{ and } M=\min\left\{1-1+1,1-\frac{1}{2}+\frac{1}{2}\right\}=1\Rightarrow z^*=1$$

$$z\in\overset{m}{[}1,\overset{M}{1}]$$

$$z=1$$

$$z^*=1$$

3.2 The Proposed Method

Although the minimum number of points given by equation (4) $\varepsilon=10^{-5}$ and $p=10^{-3}$ is $N=11507$, we use this example the following values $N=10^6$.

Using the RandSeach algorithm for the previous numerical example we consider:

i) $N=10^6;\ M=\frac{N}{10};\ K=\frac{M}{10};$

ii) the leader's function to optimize $F(x,y,z):=3x+y+z$;

iii) the follower's function to optimize $f(x,y,z):=2x-y-7z$.

We obtain the approximate solution of this example

$\min F:=5.039$, $\min f:=-6.052$, $x=1.004$, $y=1.012$, $z=1.005$

By comparing the solution obtained by enumeration vertices method with the approximate solution given by proposed method we find the following relative error

$$\text{err}:=\sqrt{\frac{\sum_{i=2}^{4}\left|s_{1,i}-S_{i-1}\right|^2}{\sum_{i=1}^{3}\left|S_i\right|^2}}$$

$$\text{err}:=0.0085$$

which leads us to affirm that the proposed method is "good"!

CONCLUSIONS

From the list of references can be seen that the BLP problem is still actual. The simplicity of the proposed approach would recommend it for practical applications. The only problem would be the finding an efficient algorithm for the numerical simulation of uniformly distributed points in the *D*. In the considered numeric example, we can be observed that the approximate solution is sufficiently "good", the relative error being of the 10^{-3} order.

AKNOWLEDGMENT

The work described has not been published previously and if accepted, it will not be published elsewhere in the same form, in English or in any other language, including electronically without the written consent of the copyright-holder.

REFERENCES

[1] J. Bracken and J. T. McGill, *Mathematical Programs with Optimization Problems in the Constraints*, Operations Research, vol. 21, no. 1, pp. 37-44, 1973;
[2] B. Colson, P. Marcotte, G. Savard, *Bilevel programming: a survey*, 4*OR*, vol. 3, no. 2, pp. 87–107, 2005;
[3] S. Fang, P. Guo, Mo Li, L. Zhang, *Bilevel Multiobjective Programming Applied to Water Resources Allocation*, Hindawi Publishing Corporation Mathematical Problems in Engineering, 2013;
[4] S. R. Hejazi, A. Memariani, G. Jahanshahloo, M. Sepehri, *Linear bilevel programming solution by genetic algorithm*, Computers & Operations Research, vol. 29, no. 13, pp. 1913-1925, 2002;
[5] R. Mathieu, L. Pittard, A. G. Dalingam, *Genetic algorithm based approach to bilevel linear programming*, Recherche opérationnelle / operations research, vol. 23, no. 1, pp. 1-21, 1994;
[6] H. S. Shih, Y. J. Lai, E. S. Lee, *The fuzzy approach for multilevel programming problems*, Computers & Operations Research, vol. 23, no. 1, pp. 773-791, 1983;
[7] I. Văduva, *Stochastic Simulation:Monte Carlo Methods and Applications*, in Congreso Internacional de Matematica Aplicada, november 4-6, 2014, Toluca, Mexico.
[8] L. N. Vicente, P. H. Calamai, *Bilevel and multilevel programming: A bibliography review*, Journal of Global Optimization, vol. 5, no. 3, pp. 291-306, 1994.
[9] Y. Lv, T. Hu, G. Wang, Z. Wan, *A penalty function method based on Kuhn–Tucker condition for solving linear bilevel programming*, Applied Mathematics and Computation, vol. 188, no. 1, pp. 808-813, 2007.